

**Experimental investigation of the Fe-rich regions in the
Ce-Fe-{Ni, Si, Al}-B quaternary systems: High-throughput
screening of magnetic phases**

Kayode Orimoloye

A Thesis
in the Department
of
Mechanical and Industrial Engineering

Presented in Partial Fulfillment of the Requirements
For the Degree of Master of Applied Science (Mechanical Engineering) at
Concordia University
Montreal, Quebec, Canada.

August, 2016

© Kayode Orimoloye, 2016

CONCORDIA UNIVERSITY

School of Graduate Studies

This is to certify that the thesis prepared

By: **Kayode Orimoloye**

Entitled: **Experimental investigation of the Fe-rich regions in the Ce-Fe-{Ni, Si, Al}-B
quaternary systems: High-throughput screening of magnetic phases**

and submitted in partial fulfillment of the requirements for the degree of

Master of Applied Science (Mechanical Engineering)

Complies with the regulations of the University and meets the accepted standards with
respect to originality and quality.

Signed by the final Examining Committee:

_____ Chair

Dr. Ming Chen

_____ Examiner

Dr. Christian Moreau

_____ Examiner

Dr. Steve Shih

_____ Supervisor

Dr. Mamoun Medraj

Approved by:

Chair of Department or Graduate Program Director

August, 2016

Abstract

Fe-rich regions of the Ce-Fe-{Ni, Si, Al}-B quaternary systems were studied and screened for magnetic phase identification. The main magnetic phase found in these systems is the $\text{Ce}_2(\text{Fe}_{14-x}\text{T}_x)\text{B}$ solid solutions, where T denotes Ni, Si or Al. No new Fe-rich magnetic phase was discovered. Fe-rich regions of the Ce-Fe-{Ni, Si, Al}-B quaternary systems were experimentally studied using diffusion couples and selected key alloys annealed at 900°C . Homogeneity ranges of $\text{Ce}_2(\text{Fe}_{14-x}\text{Ni}_x)\text{B}$, $\text{Ce}_2(\text{Fe}_{14-x}\text{Si}_x)\text{B}$ and $\text{Ce}_2(\text{Fe}_{14-x}\text{Al}_x)\text{B}$ solid solutions were measured to be $(0 \leq x_{\text{Ni}} \leq 1.5)$, $(0 \leq x_{\text{Si}} \leq 2.33)$ and $(0 \leq x_{\text{Al}} \leq 2.5)$, respectively. Magnetic force microscope analysis was used to screen out non-magnetic phases. Among the phases observed in the Fe-rich regions of the Ce-Fe-{Ni, Si, Al}-B quaternary systems, only the quaternary extensions of $\text{Ce}_2\text{Fe}_{14}\text{B}$ show visible magnetic domains. Using thermogravimetric analysis and physical property measurement system, further tests were performed to quantify the intrinsic magnetic properties of the $\text{Ce}_2\text{Fe}_{14}\text{B}$ quaternary extended solid solutions. This is to reveal the effect of modifying $\text{Ce}_2\text{Fe}_{14}\text{B}$ ternary compound by Ni, Si and Al additives on its intrinsic magnetic properties. Modifying $\text{Ce}_2\text{Fe}_{14}\text{B}$ ternary compound with these additives showed decrease in the saturation magnetization and anisotropy field. But in the case of Curie temperature, Ni and Si additives increase the Curie temperature of $\text{Ce}_2\text{Fe}_{14}\text{B}$ ternary compound while Al additive reduces its Curie temperature.

Dedication

To my late mother,

Mrs. Felicia Orimoloye,

Who died on 15th June, 2016.

May her soul rest in eternal peace.

Acknowledgements

First and foremost, I want to thank my thesis supervisor, Dr. Mamoun Medraj. It has been an honour to be your student. I appreciate all your efforts and supports of time, ideas and funding to make my MAsc programme a successful one. Thank you for being a source of inspiration when it all looked unrealizable in the beginning.

Special appreciation goes to Dr. Dmytro Kervokov, who assisted me in building a concrete research background. Your contributions towards my thesis are also appreciated. The past and present members of TMG group have contributed immensely to my personal and professional times at Concordia. When it came to friendship, supports and good advice, you have always been there. I would seize this opportunity to thank Tian Wang. You have been a good and reliable colleague for the past years.

I would like to thank Dr. Ryan Dominic for his unalloyed support and assistance in experiments involving PPMS and TGA. Your technical suggestions towards writing a good report on magnetic properties of the studied materials are highly appreciated.

Lastly, I would like to thank my late parents for their supports, encouragements and love. I would also like to thank my sisters and brothers for their encouragements and trusts in me. Special thank you to my wife for taking care of me and our children. I do appreciate your love, trust, patience and encouragements towards the success of this thesis.

Table of Contents

Chapter 1	1
1.1 Introduction.....	1
1.2 Objectives of this study.....	6
Chapter 2	8
2.1. Binary phase diagram	7
2.1.1 Ce-Fe binary system	7
2.1.2 B-Fe binary system.....	8
2.1.3 Al-Fe binary system.....	9
2.1.4 Fe-Ni binary system.....	10
2.1.5 Fe-Si binary system.....	11
2.1.6 Ce-Si binary system	12
2.1.7 Al-Ce binary system	13
2.1.8 B-Ce binary system.....	14
2.1.9 Ce-Ni binary system	15
2.1.10 B-Ni binary system	16
2.1.11 B-Si binary system.....	17
2.1.12 Al-B binary system	18
2.2 Ternary phase diagram.....	19
2.2.1 Ce-Fe-B ternary system	19
2.2.2 Ce-Fe-Al ternary system.....	21
2.2.3 Ce-Fe-Si ternary system.....	23
2.2.4 Ce-Fe-Ni ternary system.....	24

Chapter 3	26
3.1 Diffusion couple technique	25
3.2 Key alloys preparation	26
3.3 Characterization of samples	26
3.3.1 Scanning electron microscopy	26
3.3.2 X-ray diffraction	27
3.3.3 Magnetic force microscopy	27
3.3.4 Magnetic measurements	28
Chapter 4	31
4.1 Ce-Fe-Ni-B system	30
4.1.1 Solid-solid diffusion couples	31
4.1.2 Experimental results of the key alloys	41
4.1.3 MFM characterization of phases at the Fe-Ni side of the Ce-Fe-Ni-B system	57
4.1.4 Intrinsic magnetic properties of the $Ce_2Fe_{14}B$ modified by Ni compound	59
4.1.5 Discussion of the results of the Ce-Fe-Ni-B quaternary system	63
4.2 Ce-Fe-Si-B system	67
4.2.1 Solid-solid diffusion couples	67
4.2.2 Experimental results of the key alloys	74
4.2.3 MFM characterization of phases in the Fe region of the Ce-Fe-Si-B system	80
4.2.4 Intrinsic magnetic properties of the $Ce_2Fe_{14}B$ compound modified by Si	83
4.2.5 Discussion of the results of the Ce-Fe-Si-B quaternary system	87
4.3 Ce-Fe-Al-B system	90
4.3.1 Phase analysis	90

4.3.2	XRD analyses of the Ce-Fe-Al-B key alloys	94
4.3.3	MFM characterization in the Fe region of the Ce-Fe-Al-B system	95
4.3.4	Intrinsic magnetic properties of the Ce ₂ Fe ₁₄ B compound doped with Al	96
4.3.5	Discussion of the results of the Ce-Fe-Al-B system.....	100
Chapter 5	103
5.0	Conclusions.....	102
5.1	Contributions	103
5.2	Recommendations for future work	104

List of Figures

Figure 1.1: Typical PM motors in cars [9].....	3
Figure 1.2: General Motors permanent magnetic electric motor [10]	3
Figure 1.3: Worldwide production timeline of rare earth elements on oxide basis by major producers [2]	5
Figure 2.1: Ce-Fe phase diagram [28]	8
Figure 2.2: B-Fe Phase Diagram. Full lines represent interstitial model while dashed lines represent substitutional model. Indicated values are from the interstitial model [29].....	9
Figure 2.3: Fe-Al phase diagram [38].....	10
Figure 2.4: Fe-Ni phase diagram [43].....	11
Figure 2.5: Fe-Si phase diagram [46]	12
Figure 2.6: Ce-Si phase diagram [51].....	13
Figure 2.7: Al-Ce phase diagram [54]	14
Figure 2.8: Ce-B phase diagram [55]. Solid lines represent to the lines confirmed by various works while dotted lines represent those are not consistent or determined.....	15
Figure 2.9: Ce-Ni phase diagram [57]	16
Figure 2.10: B-Ni phase diagram [62]	17
Figure 2.11: B-Si phase diagram [65]. Dotted lines are based on the work of Olesinski et al. [63] and solid lines are based Zaitsev et al. [64]	18
Figure 2.12: Partial Al-B phase diagram [66].....	19
Figure 2.13: Ce-Fe-B isothermal section at 700 ^o C [46].....	21
Figure 2.14: Al-Ce-Fe isothermal section at 500 ^o C [78]	22
Figure 2.15: Isothermal section of Ce-Fe-Si system at 900 ^o C, redrawn from [80].....	24

Figure 3.1: Typical d^2M/dH^2 curve from SPD method for determining anisotropy field in the $Ce_2(Fe, X)_{14}B$ solid solution ($X = Ni, Si$ and Al)	29
Figure 4.1: Compositions of the diffusion couples in the Ce-Fe-Ni-B system.....	31
Figure 4.2: BSE micrographs of the solid-solid diffusion couple 1 in the Ce-Fe-Ni-B system. ..	33
Figure 4.3: BSE micrographs of the solid-solid diffusion couple 2 in the Ce-Fe-Ni-B system. The numbers shown on parts (a), (b), (d-f) and (h) refer to the diffusion zone numbers	36
Figure 4.4: BSE micrographs of the solid-solid diffusion couple 3 in the Ce-Fe-Ni-B system. The numbers shown on parts (b) and (d-f) refer to the diffusion zone numbers	39
Figure 4.5: The compositions, in at.%, of the key alloys in the Ce-Fe-Ni system	42
Figure 4.6: BSE micrographs of key alloys (a) 1, (b) 2.....	43
Figure 4.7: Partial isothermal section of the Ce-Fe-Ni system at $700^\circ C$	44
Figure 4.8: The compositions of the key alloys in the Ce-Fe-Ni-B system.....	46
Figure 4.9: BSE micrographs of key alloys (a) 1, (b) 3 after 10 days annealing, (c) 3 after 31 days annealing, (d) 4	48
Figure 4.10: BSE micrographs of key alloys (a) 7, (b) 10, (c) 12, (d) 14.....	51
Figure 4.11: BSE micrographs of key alloys (a) 15, (b) 16, (c) 17, (d) 18.....	54
Figure 4.12: XRD pattern of key alloys (a) 3, (b) 5, (c) 11, (d) 16.....	57
Figure 4.13: Compositions of the selected key alloys used for MFM characterization of the $Ce_2(Fe_{14-x}Ni_x)B$ solid solution. The arrow represents increasing Ni direction.....	58
Figure 4.14: MFM magnetic domain micrographs of key alloys (a) 1, (b) 2, (c) 5.....	59
Figure 4.15: The composition dependence of the saturation magnetization (M_S) of the $Ce_2(Fe, Ni)_{14}B$ solid solution at 298 K	61

Figure 4.16: The composition dependence of the anisotropy field (H_A) of the $Ce_2(Fe, Ni)_{14}B$ solid solution at 298 K	62
Figure 4.17: The composition dependence of the Curie temperature (T_C) of the $Ce_2(Fe, Ni)_{14}B$ solid solution.....	63
Figure 4.18: Compositions of the diffusion couples in the Ce-Fe-Si-B system	68
Figure 4.19: BSE micrographs of the solid-solid diffusion couple 1 in the Ce-Fe-Si-B system. The numbers shown on parts (a-e) refer to the diffusion zone numbers	70
Figure 4.20: BSE micrographs of the solid-solid diffusion couple 2 in the Ce-Fe-Si-B system. The numbers shown on parts (b-d) refer to the diffusion zone numbers	73
Figure 4.21: The compositions of the key alloys in the Ce-Fe-Si-B system	75
Figure 4.22: BSE micrographs of key alloys (a) 1, (b) 3, (c) 5, (d) 6, (e) 8	77
Figure 4.23: XRD pattern of key alloys (a) 2, (b) 5, (c) 7	80
Figure 4.24: Compositions of the selected key alloys used for MFM characterization of the $Ce_2(Fe_{14-x}Si_x)B$ solid solution. The arrow represents increasing Si direction	82
Figure 4.25: MFM magnetic domain micrographs of key alloys (a) 3, (b) 5	82
Figure 4.26: The composition dependence of the saturation magnetization (M_S) of the $Ce_2(Fe_{14-x}Si_x)B$ solid solution at 298 K	85
Figure 4.27: The composition dependence of the anisotropy field (H_A) for the $Ce_2(Fe_{14-x}Si_x)B$ solid solution at 298 K	86
Figure 4.28: The composition dependence of the Curie temperature (T_C) for the $Ce_2(Fe_{14-x}Si_x)B$ solid solution.....	87
Figure 4.29: : The compositions of the key alloys in the Ce-Fe-Al-B system.....	91
Figure 4.30: BSE micrographs of key alloys (a) 1 (b) 8.....	92

Figure 4.31: XRD pattern of key alloys (a) 2, (b) 5.....	95
Figure 4.32: MFM domain micrographs of key alloys (a) 2, (b) 3, (c) 5	96
Figure 4.33: The composition dependence of the saturation magnetization (M_S) of the Ce ₂ (Fe _{14-x} Al _x)B solid solution at 298 K.....	98
Figure 4.34: The composition dependence of the anisotropy field (H_A) of the Ce ₂ (Fe, Al) ₁₄ B solid solution at 298 K	99
Figure 4.35: The composition dependence of the Curie temperature (T_C) of the Ce ₂ (Fe, Al) ₁₄ B solid solution.....	100

List of Tables

Table 1.1: Effects of some additives on $R_2Fe_{14}B$ magnet.....	4
Table 4.1: Terminal actual compositions of the diffusion couples used to study the Ce-Fe-Ni-B system, annealed at $900^{\circ}C$ for 39 days.....	31
Table 4.2: Phase composition obtained by WDS spot analysis of diffusion couple 1 in the Ce-Fe-Ni-B system	34
Table 4.3: Phase composition obtained by WDS spot analysis on the diffusion couple 2 in Ce-Fe-Ni-B system	37
Table 4.4: Phase composition obtained by the WDS spot analysis of diffusion couple 3 in the Ce-Fe-Ni-B system	40
Table 4.5: The compositions and annealing times of key alloys used in studying the Ce-Fe-Ni system at $700^{\circ}C$	41
Table 4.6: Chemical analysis and the corresponding phases in key alloys 1 to 5 used in the Ce-Fe-Ni system	44
Table 4.7: Compositions and annealing times of key alloys used in studying the Ce-Fe-Ni-B system at $900^{\circ}C$	45
Table 4.8: Chemical analysis and the corresponding phases in key alloys 1 to 6	49
Table 4.9: Chemical analysis and the corresponding phases in key alloys 7 to 14	52
Table 4.10: Chemical analysis and the corresponding phases in key alloys 15 to 18	55
Table 4.11: Compositions and annealing conditions of the selected key alloys used for MFM characterization of the $Ce_2(Fe_{14-x}Ni_x)B$ solid solution annealed at $900^{\circ}C$	58
Table 4.12: Magnetic properties of the $Ce_2(Fe_{14-x}Ni_x)B$ solid solution	60

Table 4.13: Terminal compositions and annealing times of the diffusion couples used to study the Ce-Fe-Si-B system at 900°C.....	68
Table 4.14: Phase composition obtained by WDS spot analysis on diffusion couple 1 in the Ce-Fe-Si-B system.....	71
Table 4.15: Phase composition obtained by WDS spot analysis on diffusion couple 2 in the Ce-Fe-Si-B system.....	74
Table 4.16: Compositions and annealing time of key alloys used in studying the Ce-Fe-Si-B system at 900°C.....	75
Table 4.17: Chemical analysis and the corresponding phases of the key alloys in Ce-Fe-Si-B...	78
Table 4.18: Compositions of key alloys used in MFM characterization of the Ce ₂ (Fe, Si) ₁₄ B solid solution annealed at 900°C for at least 10 days.....	81
Table 4.19: Magnetic properties of the Ce ₂ (Fe _{14-x} Si _x)B solid solution.....	84
Table 4.20: Compositions of key alloys used in studying the Ce-Fe-Al-B system annealed at 900°C for 10 days.....	91
Table 4.21: Chemical analysis and the corresponding phases in key alloys 1 to 9	93
Table 4.22: Magnetic properties of Ce ₂ (Fe _{14-x} Al _x)B solid solution.....	97

List of abbreviations

PM	Permanent Magnet
RE	Rare Earth
SEM	Scanning Electron Microscopy
WDS	Wavelength Dispersive X-ray Spectroscopy
XRD	X-ray Diffraction
TGA	Thermogravimetric Analysis
PPMS	Physical Property Measurement System
M_S	Saturation Magnetization
H_A	Anisotropy Field
T_C	Curie Temperature

Chapter 1

1.1 Introduction

Rare-earth (RE) magnets are essential in a wide variety of industries such as aerospace, automotive, electronics, medical, and military, because of their superior magnetic properties [1]. Since the advent of high-flux density permanent magnets (PMs) based on RE elements, such as Nd or Sm, electric machines of PM-type are preferred over induction machines when weight and size are factors to be considered [2]. They also have several advantages over induction machines, which are heavier, noisier and require more maintenance due to their high-ratio gear boxes [2]. In today's cars, there are electric motors for door mirror positioning, window lift, seat positioning, engine cooling fans, air conditioning, ABS and anti-skid, multi speaker radio and CD systems [3]. These gadgets are not just encountered in prestige cars but are fitted as standard on most models [3]. Additional features in cars add to the numbers of existing motors, which consequently increase the quantity of PMs in that car. Figure 1.1 shows some of the areas in which PMs are being used in a car.

RE magnets are composed of alloys of the lanthanide group of elements. The two lanthanide elements most prevalent used in the production of PMs are neodymium (Nd) and samarium (Sm), with neodymium-iron-boron (Nd-Fe-B) and samarium-cobalt (Sm-Co) as their most common commercial varieties [4]. Sm-Co PMs, introduced to the market in the 1970's, has found its applications in high performance or miniaturized machines where its high price and limited availability are acceptable [5]. It is also a type of RE magnet material that is highly

resistant to oxidation with better temperature resistance than neodymium materials and the energy product ranges for the SmCo_5 -type and $\text{Sm}_2\text{Co}_{17}$ -type magnets are 15 to 22 MGOe and 22 to 32 MGOe, respectively [4]. Research on the alternative PMs-based on RE continued after the eruption of the political crisis in Zaire (now known as the Democratic Republic of the Congo) in 1978 [2, 6]. This political crisis caused the price of Co to increase precipitously in the latter years [2, 6]. Co is not only essential for Sm-Co PMs but also for Al-Ni-Co PMs. Searching for new PMs to replace costly and scarcely Sm-Co PMs continued until the discovery of Nd-Fe-B PMs by General Motors and Sumitomo Special Metals Company Limited in 1983 [5, 7, 8]. Nd-Fe-B is mechanically stronger than Sm-Co magnet and it is also the most advanced commercialized PM material available today with the highest energy product approaching 52 MGOe, moderate temperature stability, and very high coercive force but can only be used at temperatures below 150°C [4, 6]. Figure 1.2 shows permanent magnetic electric motor designed by General Motors in 2011. Drawbacks of Nd-Fe-B magnets include high cost, low mechanical strength, low corrosion resistance when not properly coated or plated and low Curie temperature (310°C) which causes their magnetic properties to drop significantly as the temperature increases [4].

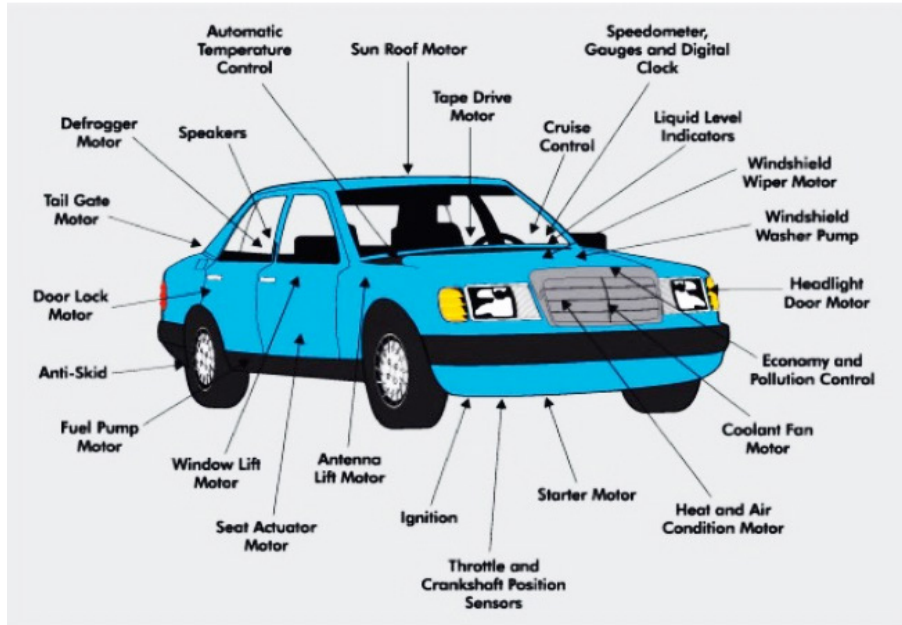


Figure 1.1: Typical PM motors in cars [9]

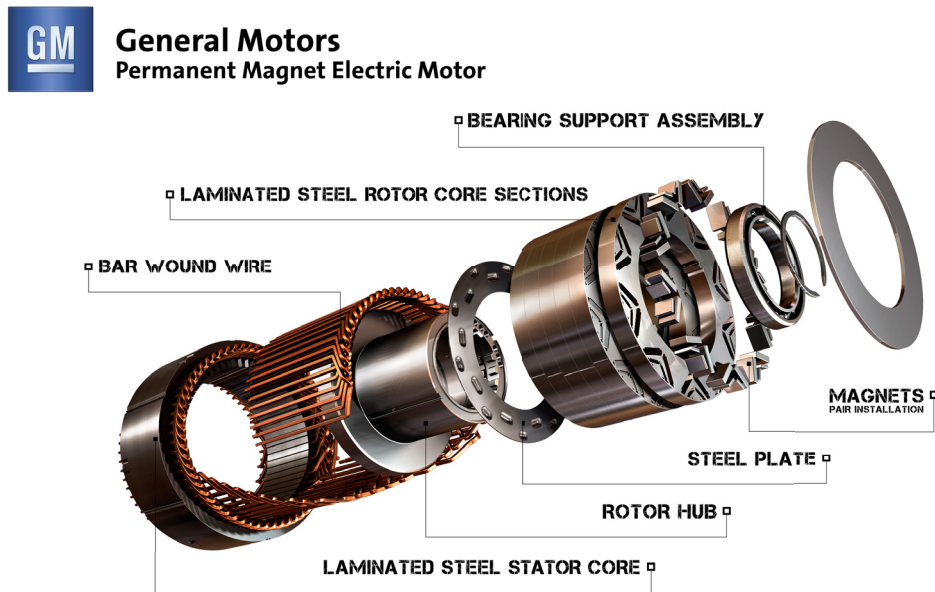


Figure 1.2: General Motors permanent magnetic electric motor [10]

Many investigations have been carried out to overcome some of the drawbacks of $\text{Nd}_2\text{Fe}_{14}\text{B}$ PM. Some of these investigations have been on the effects of additives on the $\text{Nd}_2\text{Fe}_{14}\text{B}$ and other $\text{RE}_2\text{Fe}_{14}\text{B}$ PMs. Table 1.1 summarizes effects of some additives on $\text{RE}_2\text{Fe}_{14}\text{B}$ magnets. Goll and

Kronmuller [11] reported that the spontaneous polarization J_s , the magnetocrystalline anisotropy constant K_1 and the Curie temperature T_C for high performance PMs used in high temperature applications must be greater than 1.0 Tesla, 10^6 J/m^3 and 250°C , respectively. For a material to have a large energy product, it must have a large magnetocrystalline anisotropy, which is a necessary condition for a large coercivity [12].

Table 1.1: Effects of some additives on $\text{R}_2\text{Fe}_{14}\text{B}$ magnet

Additive	Effects	Ref.
Aluminum	Increases intrinsic coercivity significantly Reduces Curie temperature Reduces saturation magnetization	[13-15]
Silicon	Increases Curie temperature Reduces saturation magnetization	[16-18]
Nickel	Increases Curie temperature Reduces saturation magnetization	[15]
Vanadium	Reduces Curie temperature Reduces saturation magnetization	[14]
Cobalt	Increases Curie temperature	[15, 19]
Manganese	Reduces Curie temperature significantly	[20]
Chromium	Reduces Curie temperature Reduces saturation magnetization	[14]
Copper	Increases Curie temperature	[18]

In 1980's, the Molycorps Mountain Pass mine in California, which was the major producer of RE elements in the world, experienced difficulties with their aging infrastructure and low RE elements prices [2]. The mine was later closed down since improvements to the mine was not viable economically, and this opened door for China in 1990's to become the main producer of RE elements [2]. Today, nearly 100% of the world's rare earth metals and more than 95% of the rare earth oxides come from China [1]. China's dominance is further demonstrated in the production of roughly half of Al-Ni-Co and Sm-Co, and over 65% of hard Ferrite PMs [1]. In spite of rising global demand, China reduced export quotas of rare earth elements in July 2010

by 72% [1]. This resulted in skyrocketing prices, long and uncertain lead times, very fast payment terms with advance payments and doubts about whether or not the materials would be available at any price [1]. Figure 1.3 shows worldwide production timeline of rare earth elements for over five decades.

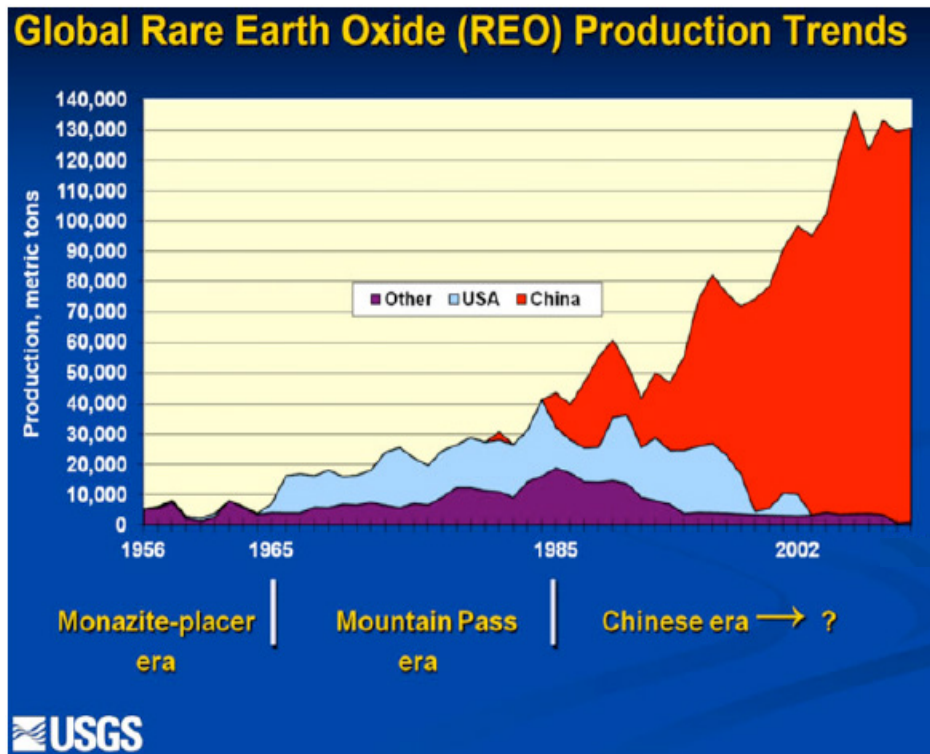


Figure 1.3: Worldwide production timeline of rare earth elements on oxide basis by major producers [2]

Between 2003 and 2011, the price of Nd metal per kg rose from US \$7.00 to US \$244.20 [21-22]. And the price of Dy per kg, which is usually added to the $\text{Nd}_2\text{Fe}_{14}\text{B}$ PM to improve its intrinsic coercivity, increased from US \$27.00 in 2003 to US \$2032.10 in 2011 [21-22]. But, the price of cerium, which has been accorded little attention, is still relatively low despite the turbulence in the market of rare earths. Use of cerium for the RE-PM has been overlooked over the years due to its lowest Curie temperature and weaker magnetic properties in both $\text{RE}_2\text{Fe}_{14}\text{B}$ and REFe_{12} series. Cerium is the most abundant rare earth, currently in market oversupply and

significantly less expensive than neodymium used in today's most powerful permanent magnet [23]. And as of December 2015, respective prices of cerium, neodymium and dysprosium metals were US \$7, US \$60 and US \$350 per kg [24]. And as it is shown in Table 1.1, it has been demonstrated that additives improve magnetic properties of the investigated $\text{RE}_2\text{Fe}_{14}\text{B}$ PM. This has shown that weaker magnetic properties of $\text{Ce}_2\text{Fe}_{14}\text{B}$ can be improved by modification with additives. Therefore, discovery of new or modified cerium-based permanent magnets will not only fill the wide gap currently existing between ferrite and neodymium-based magnets, but will also reduce the cost significantly when compared to neodymium-based magnet. Hence, we will investigate the addition of Ni, Si and Al additives on $\text{Ce}_2\text{Fe}_{14}\text{B}$ PM in this work.

1.2 Objectives of this study

The objective of this study is to experimentally determine the promising magnetic compositions in the Fe-rich sides of Ce-Fe-{Ni, Si, Al}-B quaternary systems for the ongoing research on developing low cost and high thermal stability magnetic materials suitable for automobile applications. Specific objectives of this work are:

- Searching for new quaternary phases in the Fe-rich regions of Ce-Fe-{Ni, Si, Al}-B systems, using diffusion couple and key alloy techniques;
- Studying the solubilities of the Ni, Si and Al in $\text{Ce}_2\text{Fe}_{14}\text{B}$ ternary compound;
- Identifying the magnetic phases in the Fe-rich sides of Ce-Fe-{Ni, Si, Al}-B systems, with the aid of Magnetic Force Microscope (MFM);
- Determining the intrinsic magnetic properties of the identified phases;
- Studying the effects of Ni, Si and Al additives on the intrinsic magnetic properties of $\text{Ce}_2\text{Fe}_{14}\text{B}$.

Chapter 2

Literature review

2.1. Binary phase diagram

The twelve constituent binaries in the Ce-Fe-{Ni, Si, Al}-B quaternary systems are all discussed in this section.

2.1.1 Ce-Fe binary system

Ce-Fe phase diagram has been fully established. It is characterized by two intermediate compounds (CeFe_2 and $\text{Ce}_2\text{Fe}_{17}$), which both form through peritectic reactions [25]. Figure 2.1 illustrates the phase diagram of Ce-Fe system as reported by Okamoto in 2008. CeFe_2 is ferromagnetic with Curie temperature of around 230 K [26] while magnetic properties of $\text{Ce}_2\text{Fe}_{17}$ deviate from what is observed in other $\text{RE}_2\text{Fe}_{17}$ -type. $\text{Ce}_2\text{Fe}_{17}$ is antiferromagnetic and has two ordering temperatures [26-27]. The first ordering temperature is at 94 K, below which $\text{Ce}_2\text{Fe}_{17}$ is ferromagnetic [28]. The second ordering temperature is at 206 K, Neel temperature, below which $\text{Ce}_2\text{Fe}_{17}$ is anti-ferromagnetic down to 94 K, and it is paramagnetic above the Neel temperature [28].

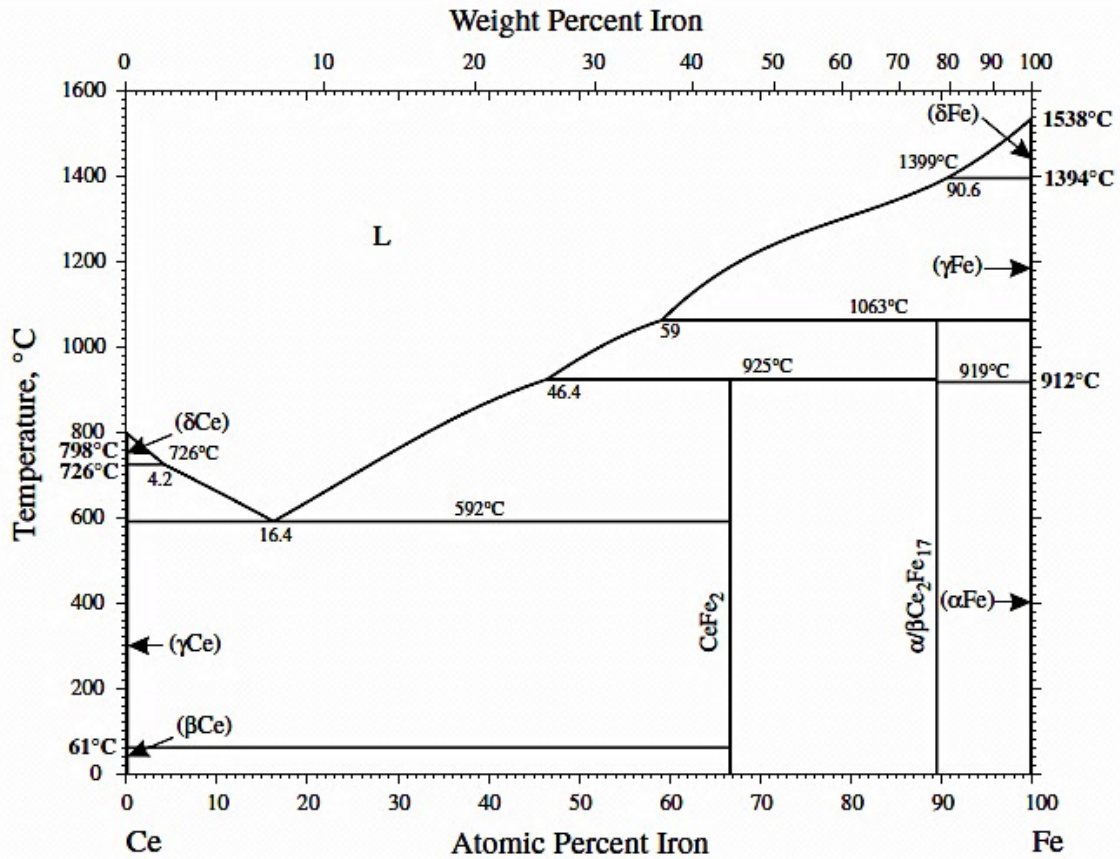


Figure 2.1: Ce-Fe phase diagram [29]

2.1.2 B-Fe binary system

B-Fe phase diagram has been completely studied. It has two intermediate phases of BFe_2 and BFe [30]. BFe_2 forms through a peritectic reaction while BFe melts congruently at 1876 K [31]. BFe_3 is a metastable phase with several crystal modifications [32]. Existence of a high-temperature modification of BFe is inconclusive [31]. Figure 2.2 shows the phase diagram of B-Fe system. Amorphous Fe_2B phase has Curie temperature of 823 K and the nanocrystalline Fe_2B annealed at 823 K is super-paramagnetic, a behavior which occurs in ferromagnetic or ferromagnetic nanoparticles [33].

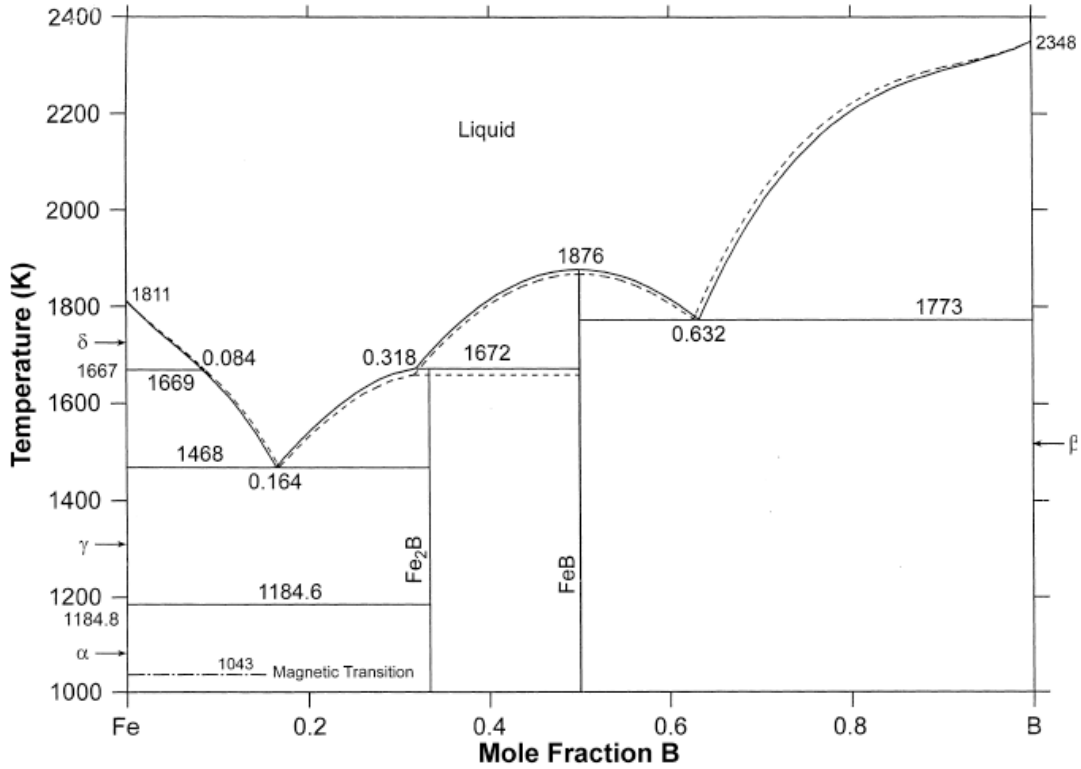


Figure 2.2: B-Fe Phase Diagram. Full lines represent interstitial model while dashed lines represent substitutional model. Indicated values are from the interstitial model [30]

2.1.3 Al-Fe binary system

The Al-Fe binary system is characterized by a wide α -Fe solid solution range and six stable intermediate phases, namely AlFe_3 , AlFe , ϵ (Al_3Fe_2), Al_2Fe , Al_3Fe_2 , and Al_3Fe [30, 33]. Due to the disagreements about the mode of formation of Al_3Fe , Kubaschewski [31] in 1992 reported it as Al_3Fe , but it was later confirmed to be $\text{Al}_{13}\text{Fe}_4$ [34-35]. AlFe_3 (D0_3) is a low temperature phase and the phase boundaries of the high temperature phase Al_3Fe_2 are still somewhat uncertain [31]. Fan et al. [37] reported that, D0_3 -ordered AlFe_3 is ferromagnetic and B2 -ordered AlFe is paramagnetic. More descriptions of the phases in the Al-Fe binary system could be found in [30, 33, 37]. Figure 2.3 shows the phase diagram of Al-Fe system from [39].

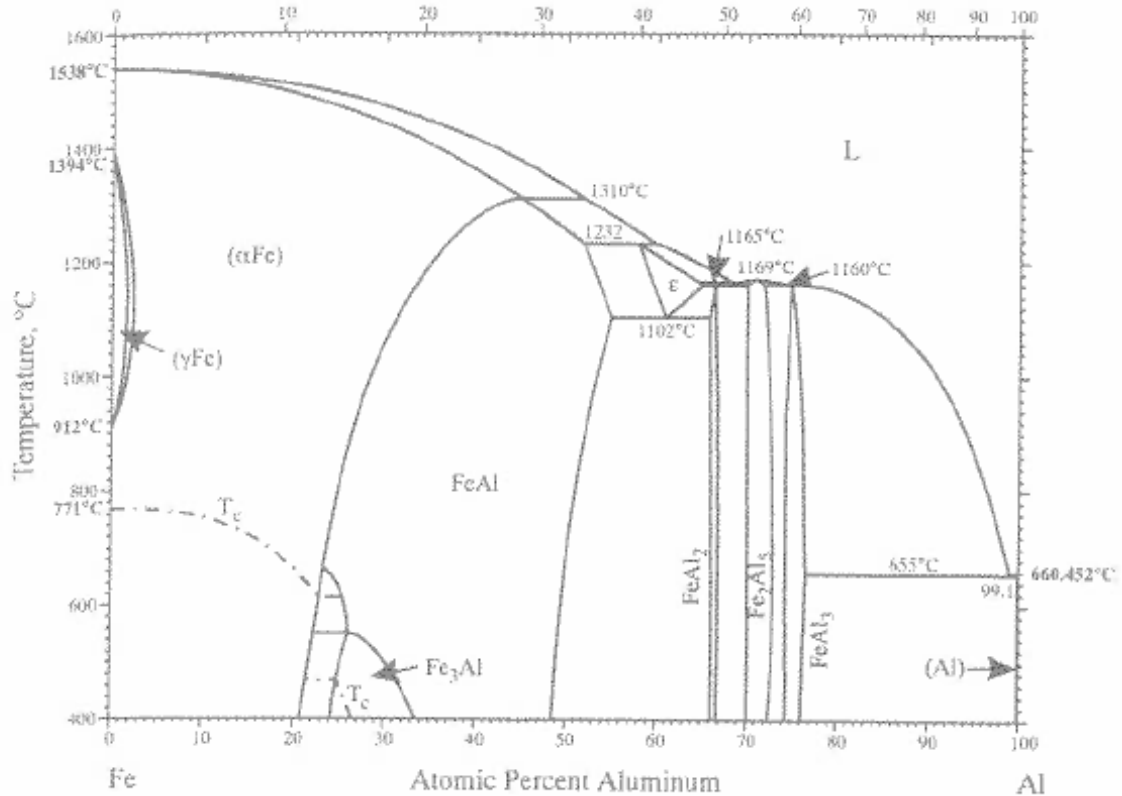


Figure 2.3: Fe-Al phase diagram [39]

2.1.4 Fe-Ni binary system

Fe-Ni phase diagram has been completely established. This system belongs to a technologically important class of alloy systems due to its extraordinary magnetic, mechanical and electrical characteristics [40]. FeNi_3 phase, forms in the Ni-rich region, reveals chemical long-range ordering of $L1_2$ -type [40]. And in iron-rich region (around 30 at.% Ni), some compositions yield negative value of the thermal expansion coefficient, the so-called Invar-effect [40]. In particular, it is still not clear whether the $L1_0$ – ordered FeNi phase is stable or metastable [41]. According to experimental studies by Reuter et al. [42], FeNi is a metastable phase, while Mishin et al. [43] indicated it to be a weak stable phase. Besides, Keyzer et al. [41] demonstrated Fe_3Ni phase to be a metastable one. Figure 2.4 shows the phase diagram of Fe-Ni system from the work of

Swartzendruber et al. [44]. $L1_0$ – ordered FeNi ferromagnet is a potential non-rare earth candidate for the hard magnetic materials. However, it cannot be easily obtained by conventional techniques for producing hard magnets, due to its extremely slow cooling formation [45].

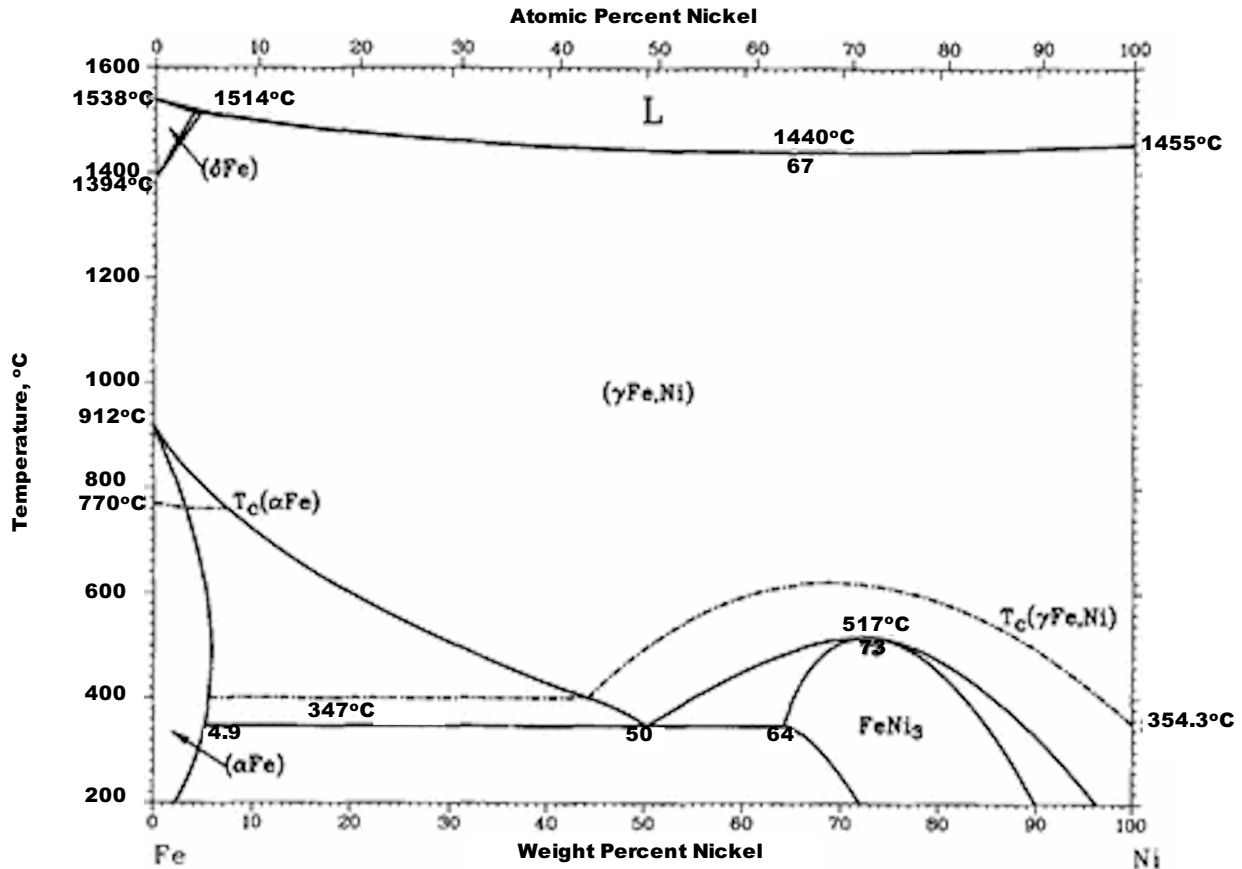


Figure 2.4: Fe-Ni phase diagram [44]

2.1.5 Fe-Si binary system

Fe-Si binary system has been completely studied. Raynor et al. [34] reported six intermediate phases, namely Fe_3Si , Fe_2Si , Fe_5Si_3 , $FeSi$, $\beta FeSi_2$ and $\alpha FeSi_2$ in this system. The two polymorphs of $FeSi_2$ are the low-temperature form, $\alpha FeSi_2$, which occurs at the stoichiometric composition and the high-temperature form, $\beta FeSi_2$, which is Fe-deficient [38]. Recently, Raghavan reported five phases in his recent publications [31, 34, 37, 45] without giving reason for the exclusion of

Fe₃Si. But, Raynor et al. [34] had previously pointed out that, there was disagreement in the region of the ordered Fe₃Si ($\alpha_1 + \alpha_2$) phase (around 18-26 at.% Si) [34]. More information on the Fe-Si binary system could be found in [30, 33]. Figure 2.11 illustrates the phase diagram of the Fe-Si system as drawn by Raghavan [47] in 1992, based on the work of Kubaschewski [31]. Fe₃Si has 840 K Curie temperature and has been reported to be a potential candidate for developing semiconductor spintronic devices [47–49].

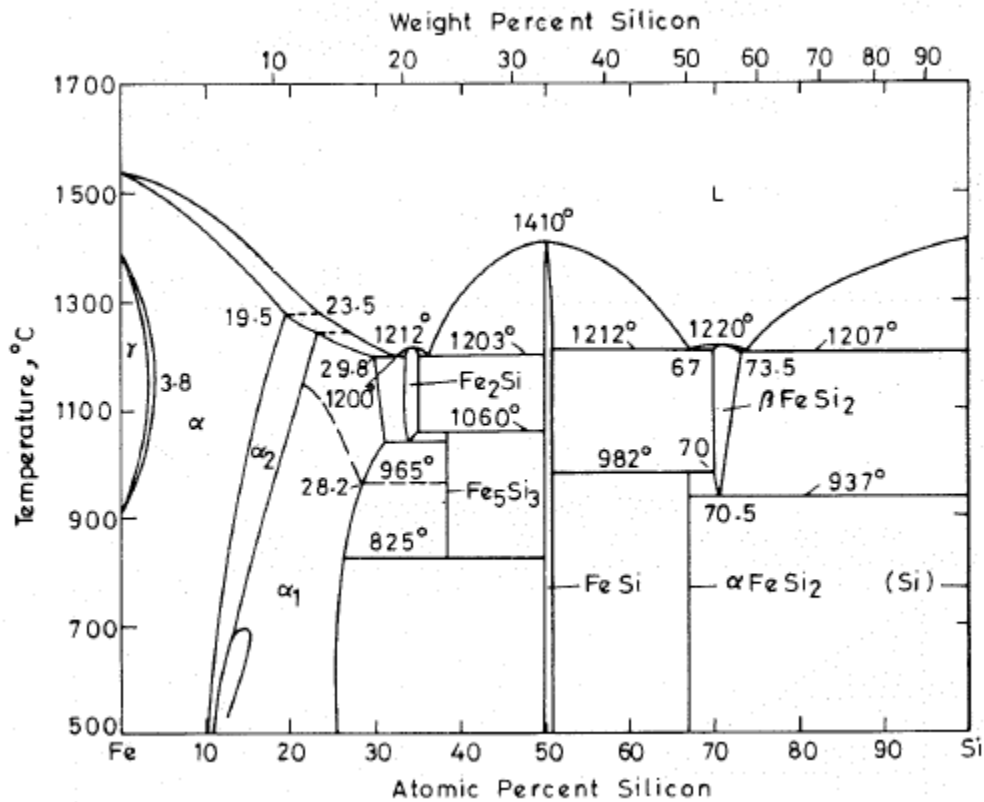


Figure 2.5: Fe-Si phase diagram [47]

2.1.6 Ce-Si binary system

Full investigation of the Cerium-Silicon was carried out by Bulanova et al. [51]. They reported six binary compounds, namely Ce₅Si₃, Ce₃Si₂, Ce₅Si₄, CeSi, Ce₃Si₅ and CeSi₂. Except for the CeSi and Ce₃Si₅ which form congruently, other compounds form peritectically [52]. The

homogeneity region of CeSi_2 is from 64 to 66.7 at.% Si [46]. Figure 2.6 shows the phase diagram of Ce-Si system and full descriptions of the phase diagram could be found in the study of Bulanova et al. [51] and the report of Okamoto [52]. The compound CeSi orders anti-ferromagnetically below 5.6 K Neel temperature [53].

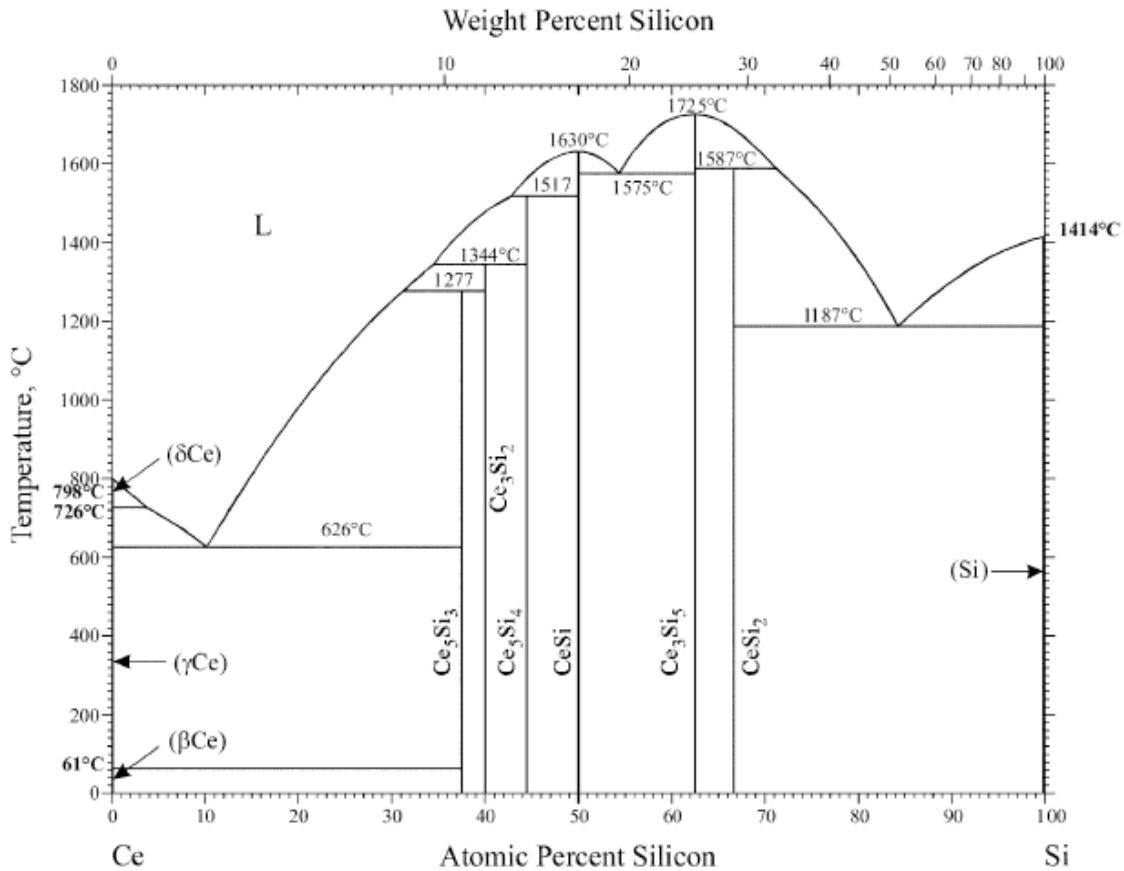


Figure 2.6: Ce-Si phase diagram [52]

2.1.7 Al-Ce binary system

The Al-Ce binary system contains AlCe_3 , Al_2Ce , AlCe , $\text{Al}_{11}\text{Ce}_3$ and Al_3Ce compounds [54]. Full descriptions of these compounds are reported by Okamoto [55] and Gschneider et al. [54]. Figure 2.7 shows the phase diagram of Al-Ce system and the reports on the magnetic properties of the compounds in this system could not be found in the literature.

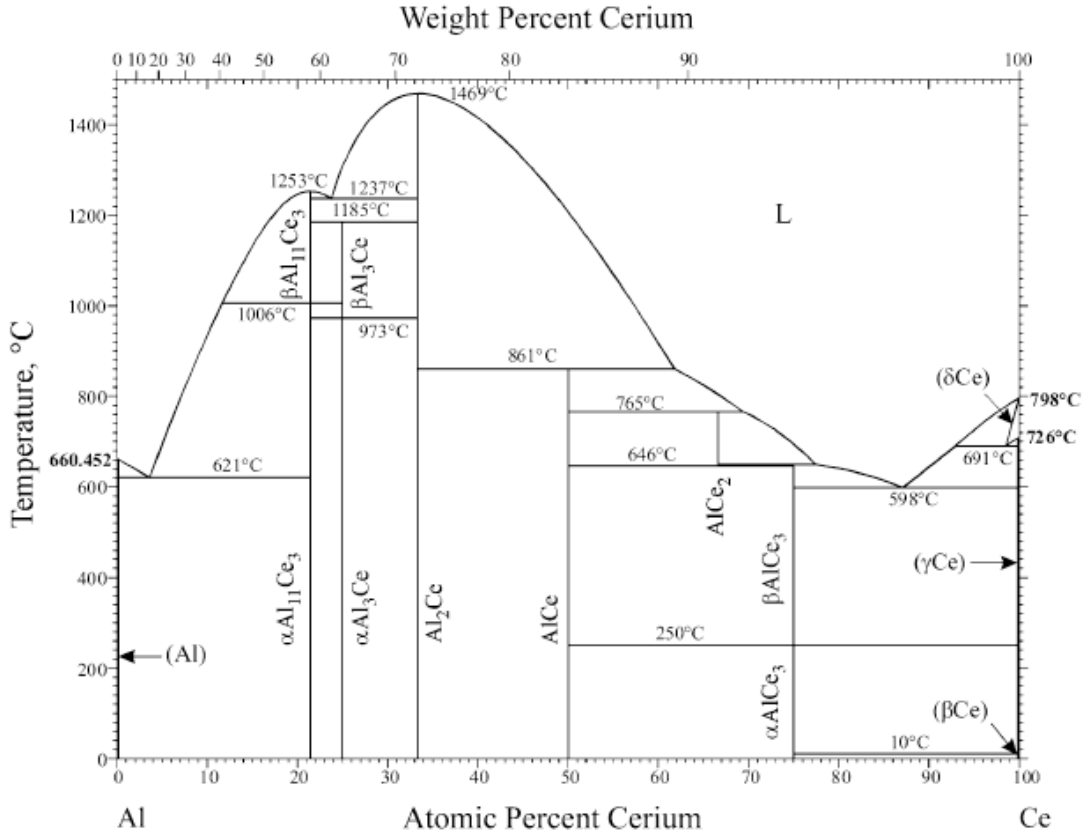


Figure 2.7: Al-Ce phase diagram [55]

2.1.8 B-Ce binary system

Full investigation of the B-Ce binary system includes liquid (L), three stable cerium polymorphs (βCe , γCe and δCe), terminal elemental-boron phase (βB), and B_4Ce and B_6Ce compounds [56]. B_6Ce compound was reported to demonstrate measurable solid-solution range [56]. Liquidus of B-Ce phase diagram could not be determined due its high temperature. Figure 2.8 illustrates the phase diagram of B-Ce system as drawn by Liao et al. [56]. Dotted lines represent the liquidus that could not be determined and the inconsistent results of various works that require further investigation while solid lines represent the results that have been confirmed by several works. Reports on the magnetic properties of the B_4Ce and B_6Ce compounds could not be found in the literature.

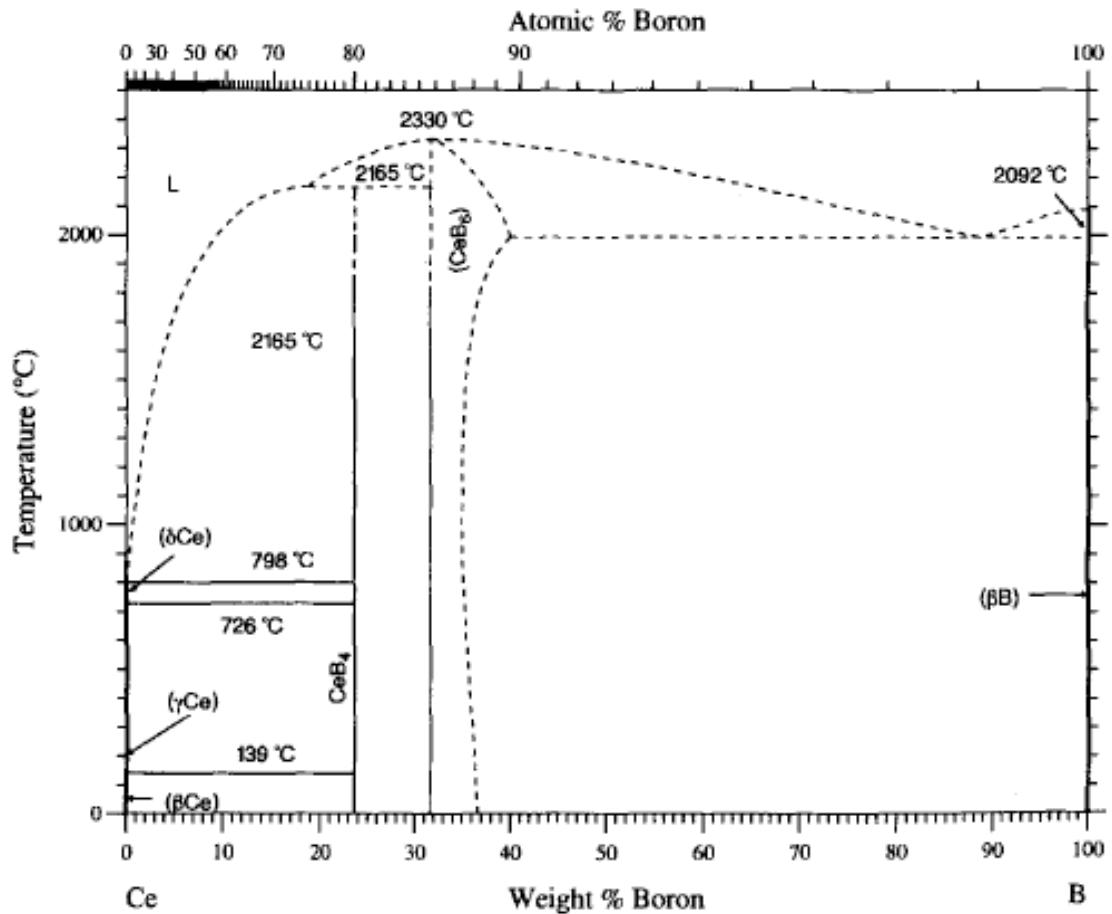


Figure 2.8: Ce-B phase diagram [56]. Solid lines represent to the lines confirmed by various works while dotted lines represent those are not consistent or determined

2.1.9 Ce-Ni binary system

The Ce-Ni system contains Ce_7Ni_3 , CeNi , CeNi_2 , CeNi_3 , Ce_2Ni_7 and CeNi_5 compounds [57]. CeNi_5 has a measurable homogeneity range [56-57]. The formation of Ce_7Ni_3 , CeNi and CeNi_5 is congruent while CeNi_2 , CeNi_3 , and Ce_2Ni_7 form peritectically [58]. Figure 2.9 shows the phase diagram of Ce-Ni system based on the report of Okamoto [58]. CeNi_3 is paramagnetic and Ce_2Ni_7 shows a very weak ferromagnetism and low 42 K Curie temperature [58-59].

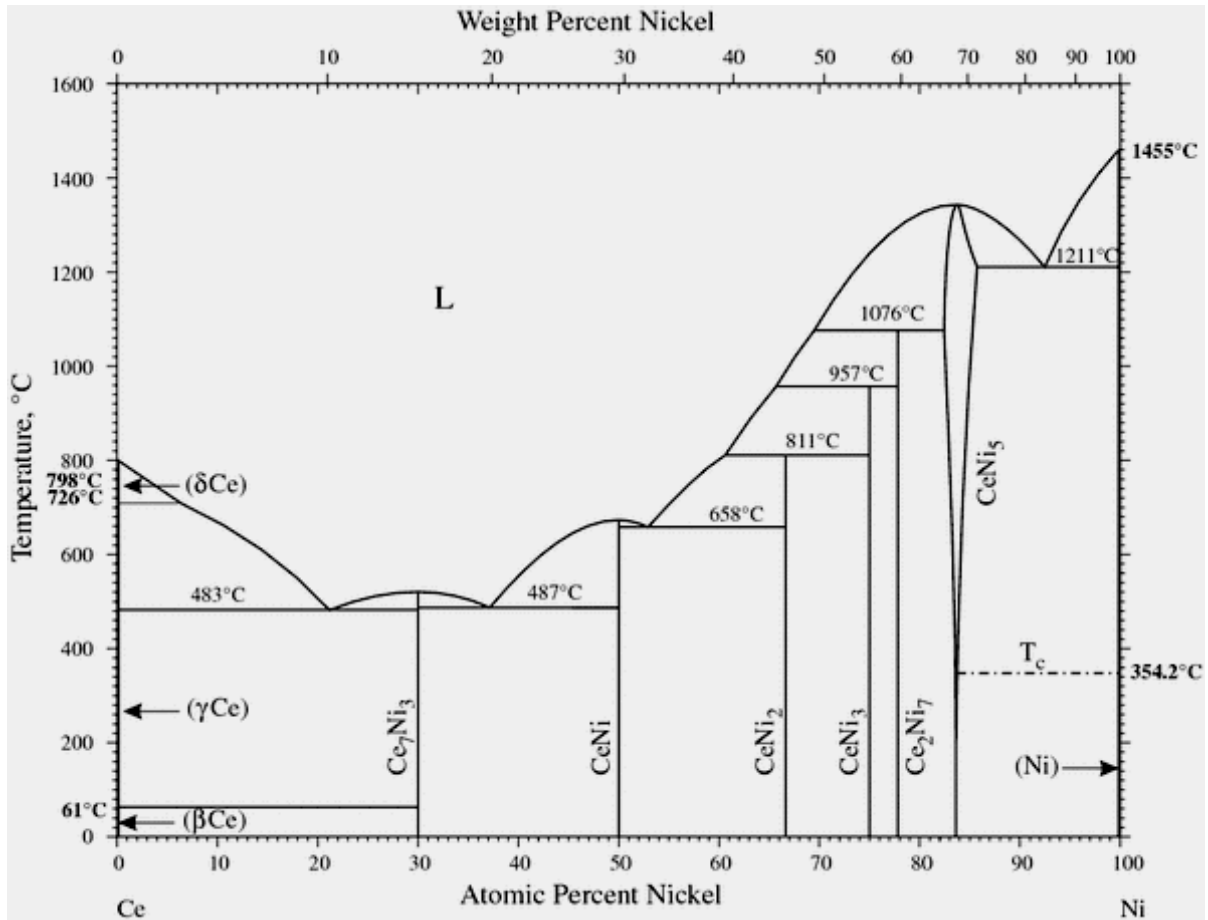


Figure 2.9: Ce-Ni phase diagram [58]

2.1.10 B-Ni binary system

Despite difficulties in attaining equilibrium and inadequate experimental accuracy that have given rise to several controversial points, B-Ni system has been fully studied [61]. With the aid of thermal analysis, microscopic and x-ray diffraction methods, Schobel et al. [62] reported five intermetallics, namely BNi₃, BNi₂, orthorhombic B₃Ni₄, monoclinic B₃Ni and BNi. More details of the B-Ni binary system could be found in [60–62]. Figure 2.10 shows the phase diagram of B-Ni system from the work of Liao and Spear [63]. Reports on the magnetic properties of the B-Ni compounds could not be found in the literature.

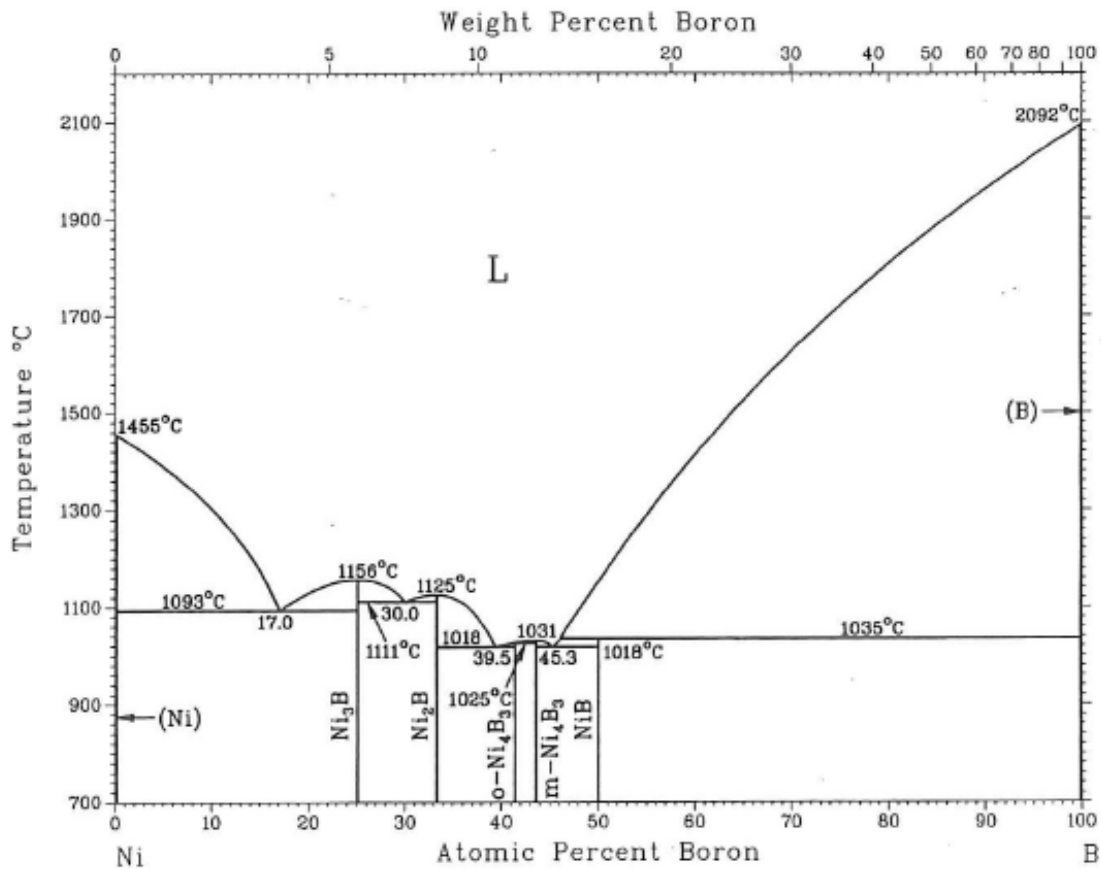


Figure 2.10: B-Ni phase diagram [63]

2.1.11 B-Si binary system

Three intermediate phases were reported in the B-Si binary system; B₃Si, B₆Si and B_nSi ($n \approx 23$) [64]. Zaitsev et al. [65] studied the thermodynamic properties of the B-Si alloys and the phase diagram was obtained by thermodynamic modeling. The difference between the works of Olesinski et al. [64] and Zaitsev et al. [65] is most noticeable for the $L \rightarrow B_6Si + (Si)$ eutectic reaction [66]. Figure 2.11 illustrates the phase diagram of the B-Si system as drawn by Okamoto [66], based on the work of Olesinski et al. [64] and Zaitsev et al. [65]. No report could be found in the literature on the magnetic properties of the compounds in this system.

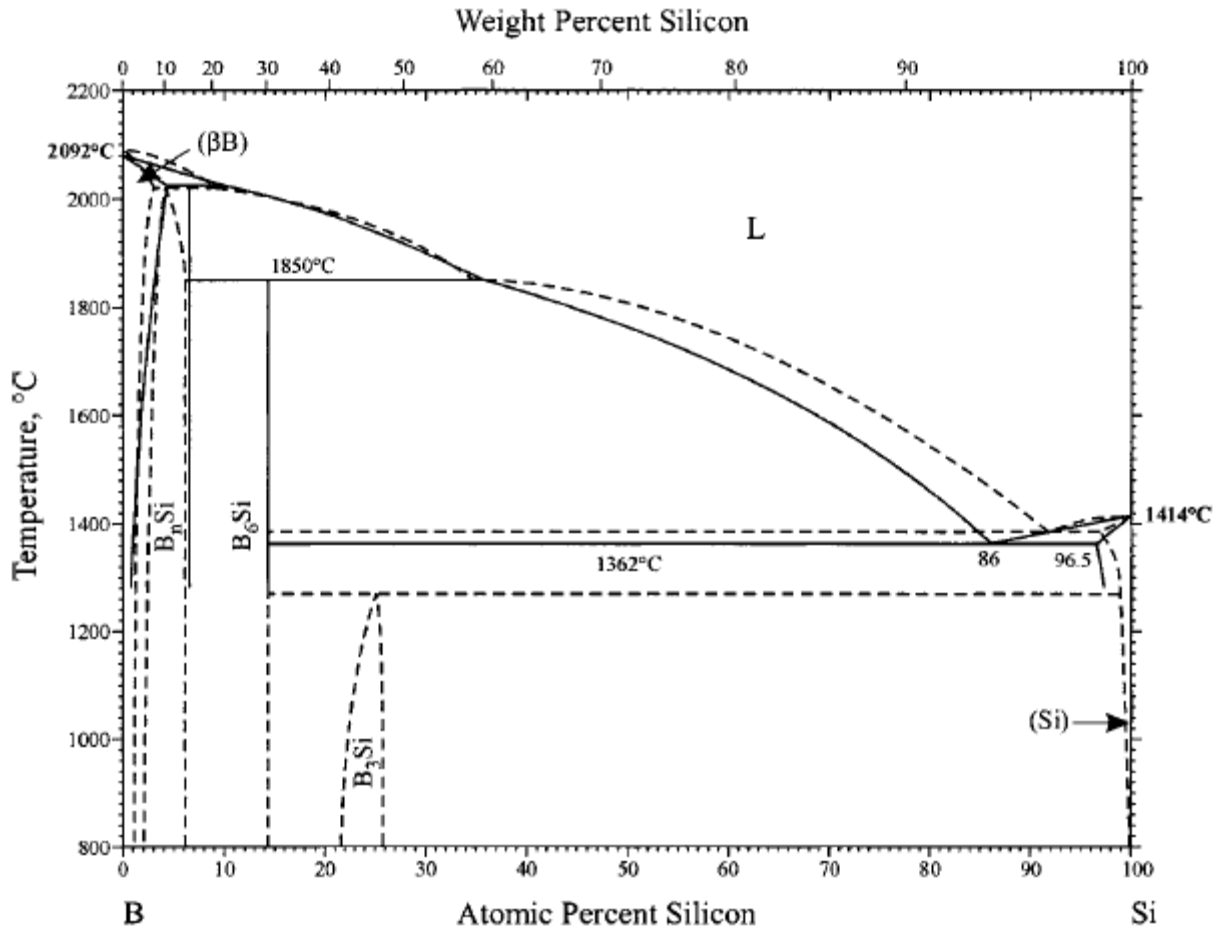


Figure 2.11: B-Si phase diagram [66]. Dotted lines are based on the work of Olesinski et al. [64] and solid lines are based Zaitsev et al. [65]

2.1.12 Al-B binary system

Despite various inconclusive speculations on the Al-B system, its full phase diagram is characterized with AlB_2 and AlB_{12} compounds [67]. Both AlB_2 and AlB_{12} form through peritectic reactions. The complete phase diagram of this system could not be found in the literature, but a partial phase diagram in the Al-rich side, which was reported by Duschanek and Rogl [67], is shown in Figure 2.12. No report on the magnetic properties of Al-B system is available in the literature.

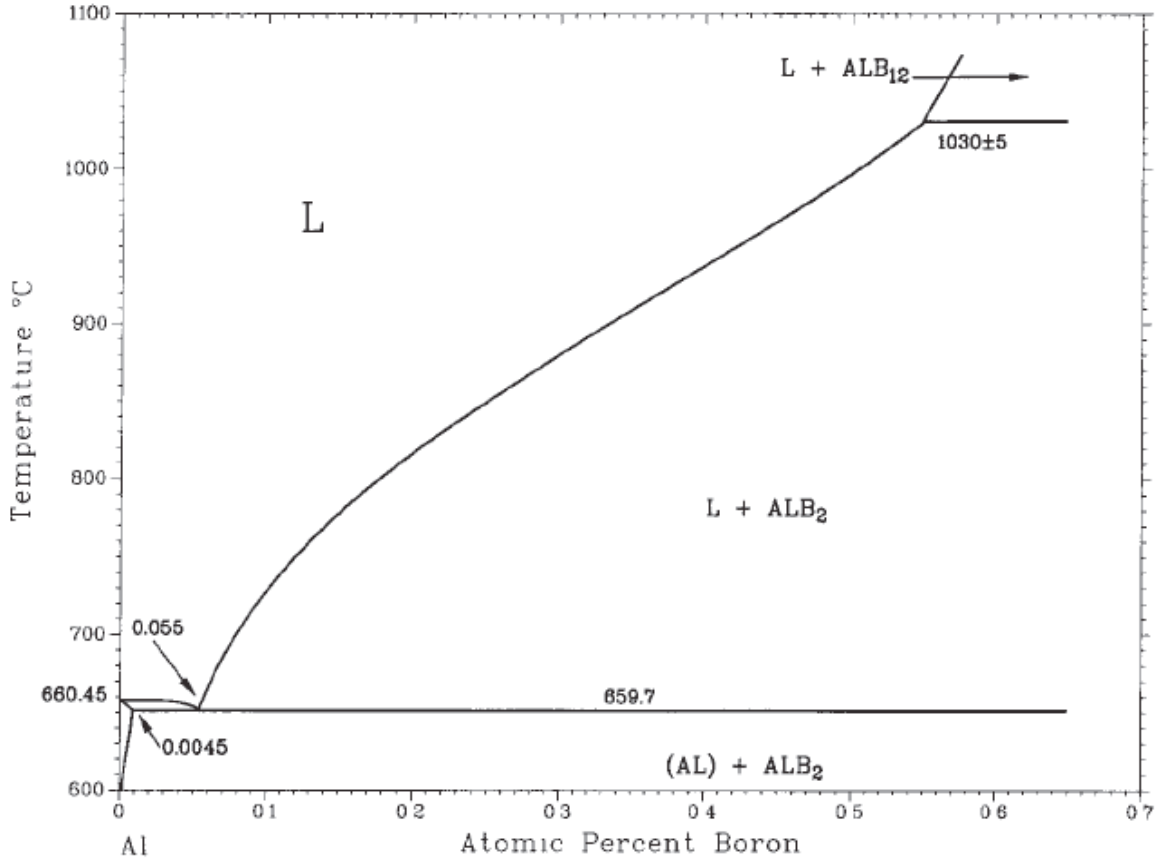


Figure 2.12: Partial Al-B phase diagram [67]

2.2 Ternary phase diagram

Since the aim of this work is to experimentally investigate the Fe-rich part of the Ce-Fe-{Ni, Si, Al}-B quaternary systems, only the four containing Ce and Fe, out of the ten constituent ternary systems, will be discussed in this thesis. The ternary phase diagrams that will be discussed here are Ce-Fe-B, Ce-Fe-Al, Ce-Fe-Ni and Ce-Fe-Si ternary systems.

2.2.1 Ce-Fe-B ternary system

Ce-Fe-B ternary system is a key system in studying the influence of Ni, Si and Al additions on the magnetic properties of Ce₂Fe₁₄B compound. It contains Ce₂Fe₁₄B magnetic compound, which is the basis of the current experimental work.

Bilonizhko et al. [68] investigated the Ce-Fe-B ternary system with alloys containing not more than 33.3 at.% Ce composition at 700^oC for 300 hours and composition of 33.3 to 100 at.% Ce at 500^oC for 500 hours. They identified three ternary compounds with approximate compositions of CeFe₂B₂, Ce₃Fe₁₆B and Ce₂FeB₃ [68]. No ternary solubilities in the binary compounds were detected. Dub et al. [69] later identified Ce₂FeB₃ composition to have Ce_{5-x}Fe_{2+x}B₆ (τ_3) formula, but the range of x was not indicated in their [69] work. In a following paper, Dub et al. [70] corrected Ce₃Fe₁₆B to have Ce₂Fe₁₄B composition while CeFe₂B₂ (τ_2) has the composition Ce_{1.1}Fe₄B₄ [46, 70]. Figure 2.12 shows an isothermal section of the Ce-Fe-B system at 700^oC.

Herbst et al. [72] investigated Ce₂Fe₁₄B in different melt-spun alloy compositions and annealing temperatures. They reported optimum magnetic properties of 4.9 kG remanence, 6.2 kOe intrinsic coercivity and 4.1 MGOe maximum energy product for the Ce₁₇Fe₇₇B₆ alloy [72]. Recently, Zhou et al. [73] also investigated Ce-Fe-B alloys containing Ce₂Fe₁₄B compound by melt spinning. Unlike 550^oC annealing temperature in which optimum magnetic properties were obtained for the Ce₁₇Fe₇₇B₆ alloy by Herbst et al. [72], Zhou et al. [73] annealed at 400^oC and observed higher magnetic properties of 6.9 kG remanence, 6.2 kOe intrinsic coercivity and 8.6 MGOe maximum energy product for the same alloy composition. They concluded that the optimum magnetic properties can be obtained in the alloys with 14-17 at.% Ce, if the annealing temperature is around 400^oC [73].

$\text{Ce}_2\text{Fe}_{17}$ compound with maximum solubility of about 60 at.% Al and that the CeFe_2 phase does not dissolve Al [75]. Results of Franceschini et al. [76] proved that the conclusion of Zarechnyuk et al. [75], that Al does not dissolve in CeFe_2 , to be wrong. They reported that Al substitute Fe in CeFe_2 , and the solubility is up to around $x = 0.125$ (8.3 at.%) in $\text{Ce}(\text{Fe}_{1-x}\text{Al}_x)_2$ [76]. Zolotarevsky et al. [77] reported another ternary phase of CeFe_4Al_8 (ϕ) composition. Figure 2.13 shows partial isothermal section of Ce-Fe-Al system at 500°C [77]. This system has complex phase relationships in the Al-rich corner and the Ce-Fe compounds tend to dissolve significant amount of Al.

Magnetic study of the $\text{Ce}_2(\text{Fe},\text{Al})_{17}$ showed that Curie temperature increases from 238 K for $\text{Ce}_2\text{Fe}_{17}$ to 384 K for $\text{Ce}_2(\text{Fe}_{17-x}\text{Al}_x)$ where $x = 3$, composition and then decreases at higher aluminum content [78].

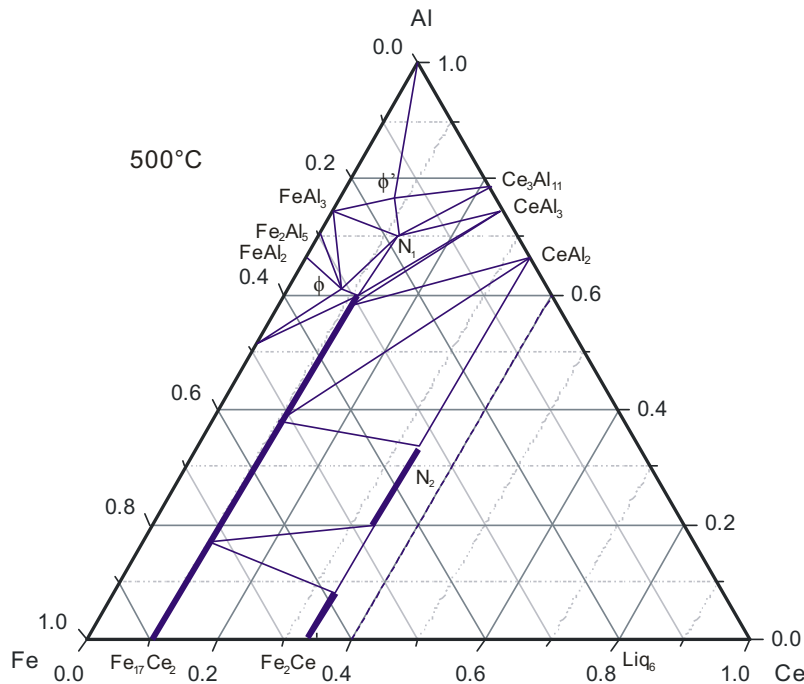


Figure 2.14: Al-Ce-Fe isothermal section at 500°C [79]

2.2.3 Ce-Fe-Si ternary system

Full experimental study of the Ce-Fe-Si ternary system has been established for many isothermal sections. Bodak et al. [80] in 1970 used X-ray powder diffraction method to study the Ce-Fe-Si ternary system in the range 0 - 33.3 at.% Ce at 400^oC and the range of 33.3-100 at.% Ce at 800^oC. They confirmed the presence of two ternary compounds (CeFe₂Si₂ and Ce₂FeSi₃) and discovered two more compounds: CeFeSi₂ and CeFeSi [80]. Further study of Ce-Fe-Si system at 900^oC by Berthebaud et al. [81] revealed additional compounds of Ce(Fe_{13-x}Si_x) (2.4 ≤ x ≤ 2.6) and Ce(Fe_{13-y}Si_y) (3.5 ≤ y ≤ 5). They also corrected the composition of Ce₂FeSi₃ compound to be Ce₅Fe₂Si₈ [81]. Because of the combined use of XRD and SEM/EDS, Berthebaud et al. [81] published more detailed and precise description of the Fe-rich corner and ternary solubilities of binary phases compared to the work of Bodak et al. [80]. Figure 2.14 illustrates the Ce-Fe-Si isothermal section drawn at 900^oC by Raghavan [46] in 2008 after the work of Berthebaud et al. [81] in the previous year. The occurrence of many ternary compounds makes the phase equilibria complex in this system. Besides, CeFe₂ compound seems to dissolve limited amounts of Si, compared to Ce₂Fe₁₇.

Magnetic study of Ce(Fe_{13-x}Si_x) (2.4 ≤ x ≤ 2.6) and Ce₂Fe_{17-x}Si_x (0 ≤ x ≤ 3) solid solutions showed that substitution of diamagnetic Si for Fe results in an increment in Curie temperature and a reduction of the unit-cell volume [23, 82–84].

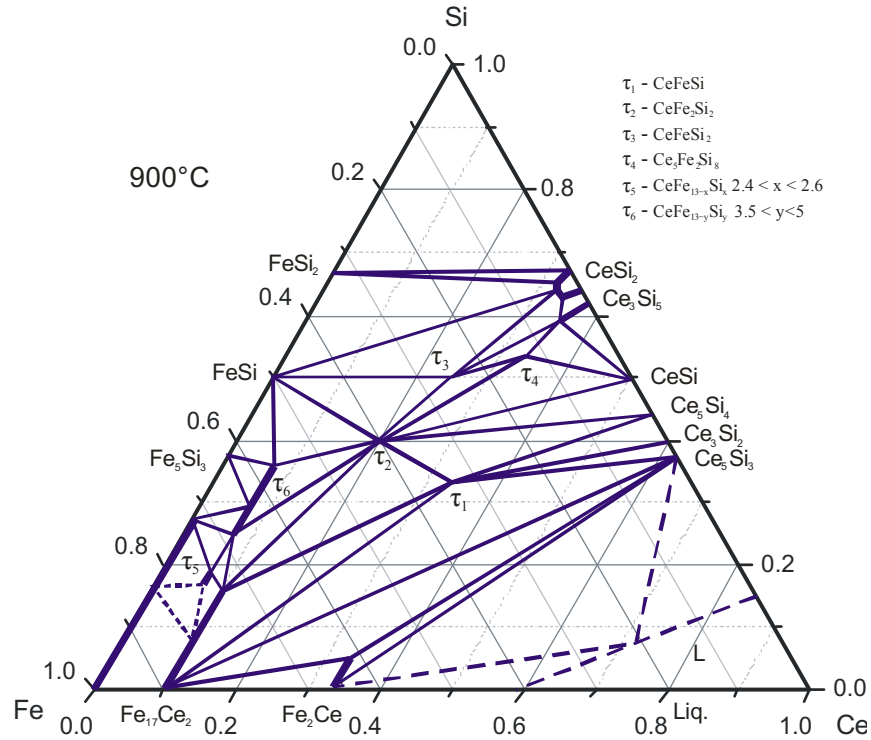


Figure 2.15: Isothermal section of Ce-Fe-Si system at 900°C, redrawn from [81]

2.2.4 Ce-Fe-Ni ternary system

The experimental data on Ce-Fe-Ni is limited. This system is characterized by complete solid solution between compounds CeFe_2 and CeNi_2 [46, 84-85]. Fe substitutes Ni in CeNi_5 compound up to CeFeNi_4 composition [46, 86]. No ternary phase diagram of Ce-Fe-Ni could not be found in the literature. Therefore, it is necessary to further investigate the Ce-Fe-Ni ternary system, since no reports could be found on all the ternary solubilities of the constituent binary compounds except CeNi_5 , CeFe_2 and CeNi_2 . Therefore, this system will be investigated in the current work.

Chapter 3

Experimental procedures

This work involves three quaternary systems, namely Ce-Fe-Ni-B, Ce-Fe-Si-B, and Ce-Fe-Al-B systems. Six diffusion couples and various number of key alloys were used to investigate the Ce-Fe-Ni-B and Ce-Fe-Si-B systems. The study of Ce-Fe-Al-B was performed with key alloy technique only. Both the diffusion couples and key alloys employed in the study of Ce-Fe-{Ni, Si, Al}-B quaternary systems were annealed at 900°C. The first reason for choosing this annealing temperature are to have faster inter-diffusion and reaction among elements in the alloys. Another reason is that the annealing temperature should be lower than minimum liquidus temperature so as to avoid melting of the alloy. The choice of this temperature does not affect the intrinsic magnetic properties. Therefore, a high temperature of 900°C was favoured in order to facilitate diffusion among the different constituents in this current work

The starting materials are Al ingots with purity 99.7%, B pieces with purity 99.5%, Ce ingots with purity 99.9%, Fe pieces with purity 99.99%, Si lump with purity 99.9999% and Ni pieces with 99.99% purity. The materials were all supplied by Alfa Aesar.

3.1 Diffusion couple technique

In this work, solid-state diffusion couple technique is used. Solid-state diffusion couple involves bringing two (or more) materials in such intimate contact that they diffuse into each other [88]. In this technique, there are no problems associated with melting or powder contamination since all the phases form by diffusion reactions of bulk constituents at the interested temperature [89].

Solid-solid diffusion couples were prepared by grinding down the contacting surfaces of the end-members to 1200 grit SiC paper and then polishing using 1 μ m water-based diamond suspension with 99% pure ethanol as lubricant. The two end-members were carefully pressed together, and then clamped with a steel ring. After clamping, the sample is sealed in a quartz tube filled with argon for annealing.

3.2 Key alloys preparation

Arc-melting furnace, equipped with a water-cooled copper crucible and a non-consumable tungsten electrode, was used to prepare the samples under argon protective atmosphere. After samples were melted three times to ensure composition homogeneity, they were sealed in an evacuated quartz tube and later annealed at 900^oC for a specified period of time. Inductively Coupled Plasma/Optical Emission Spectrometry (ICP/OES) was used in determining the actual compositions of these key alloys.

3.3 Characterization of samples

In this study, the tools used in characterization of phase equilibria are Scanning Electron Microscopy (SEM), X-ray Diffraction (XRD), and Magnetic Force Microscopy (MFM). Diffusion couples were characterized with SEM while key alloys were characterized with SEM, XRD, and MFM.

3.3.1 Scanning electron microscopy

Hitachi S-3400N Scanning Electron Microscopy (SEM), which is coupled with Wave-Dispersive X-ray Spectroscopy (WDS), has been used to analyze compositions, morphologies and homogeneity ranges of the constituent phases observed in the diffusion couples and key alloys. Pure Boron standard was used for calibration. Optimum 2500 cps for correctly measuring low

boron content in WDS was attained using 20 kV accelerating voltage, around 92 nA probe current and 30 nA beam current. The error of the SEM/WDS measurement is estimated to be about ± 2 at.%.

3.3.2 X-ray diffraction

X-ray diffraction is used to determine the available phases, their relative amounts and provide information on the crystal structures of the phases in the key alloys. XRD patterns are obtained using PANalytical Xpert Pro powder X-ray diffractometer with $\text{CuK}\alpha$ radiation at 45kV and 40 mA. The XRD spectrum is acquired from 20 to 90° 2 θ with a 0.02° step size. X-ray diffraction study of the alloys is carried out using X'Pert HighScore Plus Rietveld analysis software. Pearson's crystal database [90] is used to export the crystallographic entry to check the known phases in the Ce-Fe-{Ni, Si, Al}-B systems.

3.3.3 Magnetic force microscopy

Magnetic Force Microscopy (MFM) is a form of Scanning Probe Microscopy, in which a sharp probe is scanned across a surface, and probe/sample interaction is monitored to reveal magnetic sample's domain structure in real space [90-91]. The parameters used to obtain MFM magnetic micrographs are 30 μm scan size, 1 Hz scan rate, 0.2 integral gain, 0.4 proportional gain and tapping mode. Key samples, with the compositions of the phases observed at the Fe-rich regions of Ce-Fe-{Ni, Si, Al}-B quaternary systems, are prepared. Since the phase that is magnetic gives clear contrast of magnetic domain, MFM tests is then used to screen out non-magnetic phases from all the phases observed.

3.3.4 Magnetic measurements

In developing new permanent magnetic material, the magnetic properties to be first considered and tested are saturation magnetization, anisotropy field and Curie temperature, which are all intrinsic magnetic properties [93]. Saturation magnetizations and anisotropy fields are measured using a quantum design physical property measurement system (PPMS-9T) at 298 K. The saturation magnetizations of different compositions are obtained in external fields up to 50 kOe. Anisotropy fields are determined by the singular point detection (SPD) method, using second derivative of magnetization (d^2M/dH^2) [93–95]. And a demagnetization factor of 1/3 was applied to correct the contribution of the demagnetization field in $Ce_2(Fe, X)_{14}B$ solid solutions, assuming that the lump samples used are of spherical shapes [97]. Figure 3.1 shows a typical d^2M/dH^2 curve, obtained by SPD method, for $Ce_2(Fe, X)_{14}B$ solid solutions, where $X = Ni, Si$ and Al . Using Perkin-Elmer 7 Series thermogravimetric analysis (TGA), Curie temperature of the $Ce_2(Fe, X)_{14}B$ solid solutions was measured. Curie temperature was measured by drawing tangents at the curve where magnetization vanished. The differences in the Curie temperature of standard samples used for TGA calibration such as Ni metal and Alumel (Ni-Al-Mn-Si alloy) are $+5.1^\circ C$ and $-4.5^\circ C$, respectively.

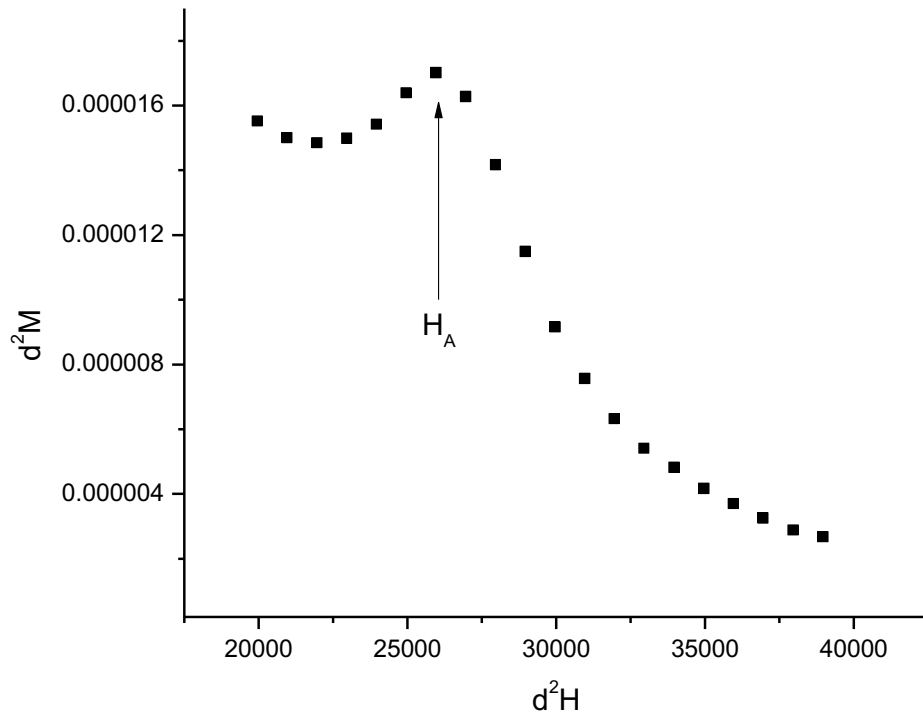


Figure 3.1: Typical d^2M/dH^2 curve from SPD method for determining anisotropy field in the $Ce_2(Fe, X)_{14}B$ solid solution ($X = Ni, Si$ and Al)

Chapter 4

Results and discussions

The main objective of this work is to first experimentally investigate the phase equilibria, using diffusion couple and key alloy techniques in the Fe-rich regions of the Ce-Fe-{Ni, Si, Al}-B quaternary systems. The magnetic phases are then identified from the observed phases using MFM analysis. Quantitative intrinsic magnetic properties of the identified magnetic phases are determined using PPMS-9T and TGA.

Diffusion couples were designed and prepared to investigate the Fe-rich sides of Ce-Fe-{Ni, Si, Al}-B quaternary systems. Key alloys are prepared to further investigate and verify the results obtained from the diffusion couples. XRD analysis is to confirm phases observed in the key alloys after they have been characterized with SEM/WDS. MFM analysis is carried out on the key alloys to identify and screen magnetic phases from all the phases present at the Fe-rich sides of Ce-Fe-{Ni, Si, Al}-B quaternary systems. After identifying magnetic phases with MFM, further tests were carried out to quantify the intrinsic magnetic properties of the promising identified phases. These properties are saturation magnetization, anisotropy field and Curie temperature.

4.1 Ce-Fe-Ni-B system

Both diffusion couple and key alloy techniques have been used to experimentally investigate Ni interaction with Fe-rich corner of the Ce-Fe-B system as can be seen in Figure 4.1. In this section, results of SEM/WDS, XRD and MFM will be explained in details and discussions of these results will then follow in a separate sub-section.

4.1.1 Solid-solid diffusion couples

Three diffusion couples were used in investigating the Fe-Ni side of the Ce-Fe-Ni-B quaternary system. The actual compositions and annealing conditions of the end-members in these diffusion couples are listed in Table 4.1 below. Figure 4.1 shows the compositions of the diffusion couples, in two views, in the Ce-Fe-Ni-B system.

Table 4.1: Terminal actual compositions of the diffusion couples used to study the Ce-Fe-Ni-B system, annealed at 900°C for 39 days

Diffusion couple (DC)	End-member 1 (at.%)	End-member 2 (at.%)
1	Ce9Fe83B8	Fe31Ni69
2	Ce15Fe74B11	Fe31Ni69
3	Ce15Fe74B11	Ni75B25

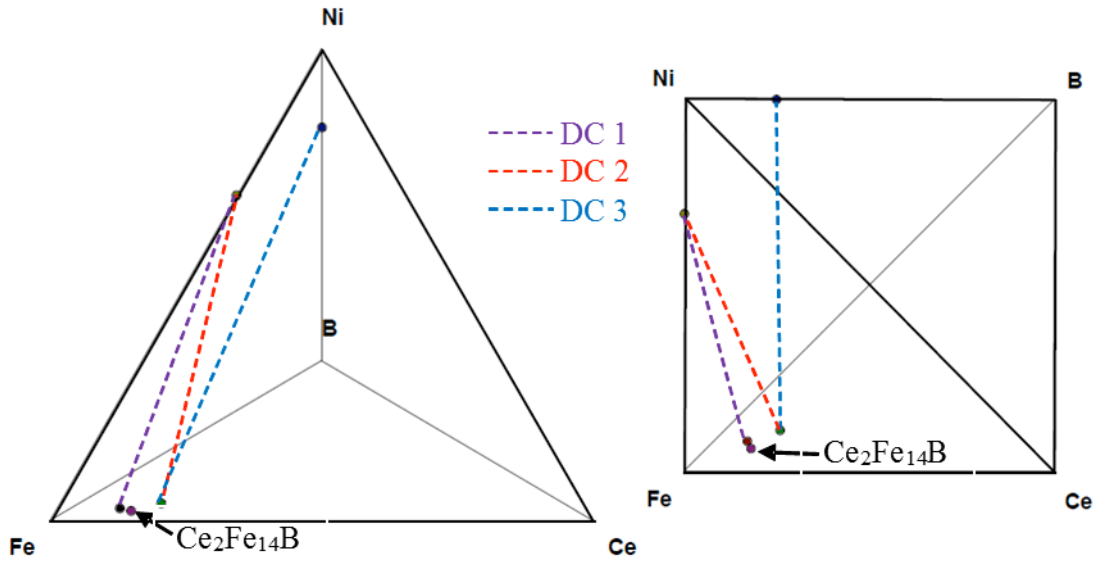


Figure 4.1: Compositions of the diffusion couples in the Ce-Fe-Ni-B system

4.1.1.1 Diffusion couple 1: Ce9Fe83B8 - Fe31Ni69 at.%

The end-member 1 is an alloy of Ce9Fe83B8. It contains three phases, namely α -Fe, Ce_{1.1}Fe₄B₄ (τ_2 in Figure 2.13) and Ce₂Fe₁₄B (τ_1 in Figure 2.13). This is in agreement with the Ce-Fe-B phase diagram shown in Figure 2.13. Figure 4.2(a) shows the BSE micrograph of the end-member 1. The end-member 2 is an alloy of Fe31Ni69 actual composition. It contains Υ (Fe, Ni) solid solution, which is consistent with the Fe-Ni phase diagram shown in Figure 2.4. After annealing this diffusion couple for 39 days at 900°C, three diffusion layers were observed. SEM/WDS spot analysis was performed to determine compositions of the phases in these zones and their results are summarized in Table 4.2. Figure 4.2(b-f) shows BSE micrographs of phases formed in this diffusion couple. From the end-member 1, the order of phases forming along the diffusion path is deduced as: α -Fe + Ce_{1.1}Fe₄B₄ + Ce₂Fe₁₄B (end-member) \rightarrow α -Fe + Ce_{1.1}Fe₄B₄ + Ce₂(Fe_{14-x}Ni_x)B ($0 \leq x \leq 1.5$) \rightarrow α -Fe + Ce_{1.1}Fe₄B₄ + Ce(Ni_{4-x}Fe_x)B ($0.19 \leq x \leq 0.78$) \rightarrow Ce(Ni_{5-x}Fe_x) ($0 \leq x \leq 1.44$) + Υ (Fe, Ni) \rightarrow Υ (Fe, Ni) (end-member). Diffusion zone 2 is a three-phase zone, which contains α -Fe, Ce_{1.1}Fe₄B₄ compound and a quaternary solid solution of Ni in Ce₂Fe₁₄B. The measured content of Ni substituting Fe in Ce₂Fe₁₄B in this layer is in the range of 0-9 at.% Ni. Figure 4.2(d) shows a BSE micrograph of zone 2. The next zone is also a three-phase equilibria but among Ce_{1.1}Fe₄B₄, a binary solid solution of Fe and Ni, and a quaternary solid solution of Fe in CeNi₄B. In CeNi₄B, the amount of Fe substituting Ni was measured within the range of 32-46 at.% Fe. Figure 4.2(e) shows a BSE micrograph of zone 3. Diffusion zone 4 is a two-phase equilibrium between a ternary solid solution of Fe in CeNi₅ and a binary solid solution of Fe and Ni. Fe substitutes Ni in CeNi₅ in the range of 7-21 at.% Fe and the range of Ni in the binary solid solution between Fe and Ni is 11-62 at.% Ni. Figure 4.2(f) shows a BSE micrograph of diffusion zone 4.

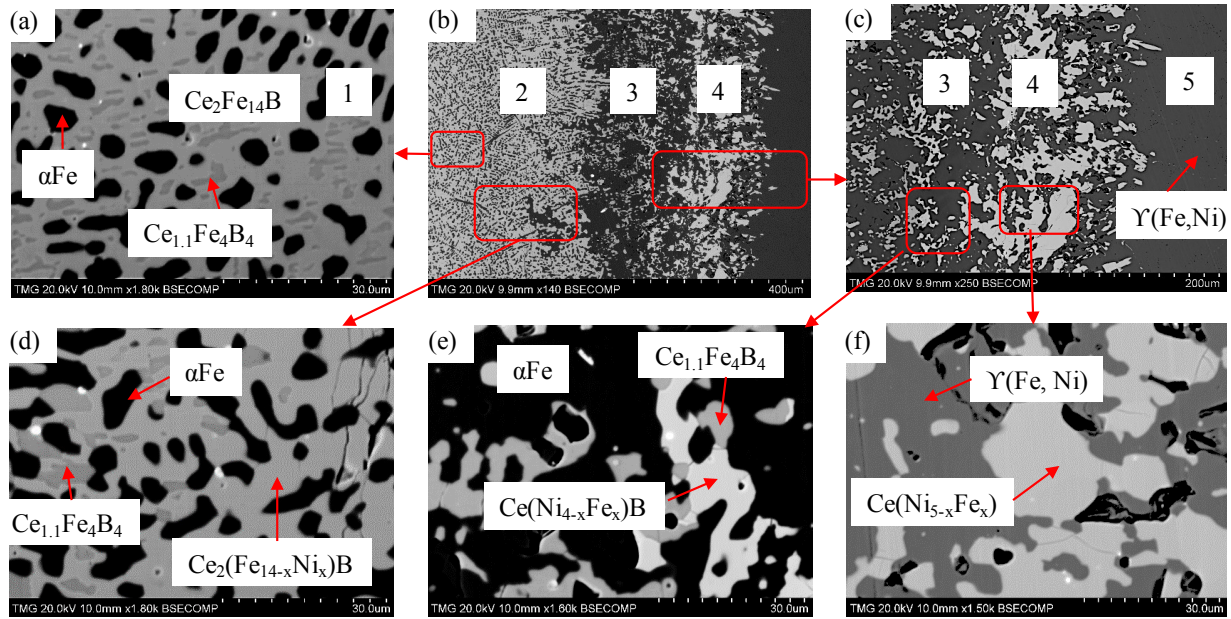


Figure 4.2: BSE micrographs of the solid-solid diffusion couple 1 in the Ce-Fe-Ni-B system.

The numbers shown on parts (a), (b) and (c) refer to the diffusion zone numbers

Table 4.2: Phase composition obtained by WDS spot analysis of diffusion couple 1 in the Ce-Fe-Ni-B system

Diffusion zone number	Description	Phase Composition (at.%)				Corresponding phase
		Ce	Fe	Ni	B	
1	Three-phase alloy (end-member)	1	99	0	0	α Fe
		12	44	0	44	$Ce_{1.1}Fe_4B_4$
		12	82	0	6	$Ce_2Fe_{14}B$
2	Three-phase zone	0-1	96-99	0-4	0	α Fe
		12	44	0	44	$Ce_{1.1}Fe_4B_4$
		12	73-82	0-9	6	$Ce_2(Fe_{14-x}Ni_x)B$ ($0 \leq x \leq 1.5$)
3	Three-phase zone	0	96	4	0	α Fe
		12	44	0	44	$Ce_{1.1}Fe_4B_4$
		15	32-46	22-36	17	$Ce(Ni_{4-x}Fe_x)B$ ($0.19 \leq x \leq 0.78$)
4	Two-phase zone	0	38-89	11-62	0	$\Upsilon(Fe, Ni)$
		17	7-21	62-76	0	$Ce(Ni_{5-x}Fe_x)$ ($0 \leq x \leq 1.44$)
5	One-phase alloy (end-member)	0	31	69	0	$\Upsilon(Fe, Ni)$

4.1.1.2 Diffusion couple 2: Fe₃₁Ni₆₉ – Ce₁₅Fe₇₄B₁₁ at.%

The end-member 1 is an alloy of Ce₁₅Fe₇₄B₁₁ actual composition. It is comprised of CeFe₂, Ce_{1.1}Fe₄B₄ and Ce₂Fe₁₄B phases, which is in agreement with the Ce-Fe-B phase diagram in Figure 2.13. The end-member 2 is an alloy of Fe₃₁Ni₆₉ actual composition, which is a single phase of $\Upsilon(Fe, Ni)$. This is consistent with the Fe-Ni phase diagram shown in Figure 2.4. Figure 4.3(a) and Figure 4.3(b) show BSE micrographs of the end-member 1 and the diffusion couple, respectively. The two end-members were clamped together and five diffusion layers were

observed after annealing at 900^oC for 39 days. Results of SEM/WDS spot analysis of the observed phases in the diffusion zones and the end-members are presented in Table 4.3. From the end-member 1, the sequence of diffusion is deduced as: CeFe₂ + Ce_{1.1}Fe₄B₄ + Ce₂Fe₁₄B (end-member) → Ce_{1.1}Fe₄B₄ + Ce₂(Fe_{14-x}Ni_x)B (0 ≤ x ≤ 1.5) → Ce(Ni,Fe)₂ + Ce(Ni_{3-x}Fe_x) (0 ≤ x ≤ 1.72) + Ce(Ni_{4-x}Fe_x)B (0.19 ≤ x ≤ 0.78) + α-Fe → α-Fe → α-Fe + Ce₂(Ni_{7-x}Fe_x) (0 ≤ x ≤ 1.14) + Ce(Ni_{4-x}Fe_x)B (0.19 ≤ x ≤ 0.78) → Y(Fe, Ni) + Ce(Ni_{5-x}Fe_x) (0 ≤ x ≤ 1.44) → Y(Fe, Ni) (end-member).

From the end-member 1, diffusion zone 2 is a two-phase equilibrium between Ce_{1.1}Fe₄B₄ and a quaternary solid solution of Ni in Ce₂Fe₁₄B. Quaternary solubility extension of Ni in Ce₂Fe₁₄B is 0-9 at.% Ni. Figure 4.3(d) shows a BSE micrograph of diffusion zone 2. Diffusion zone 3 is a four-phase equilibrium among α-Fe, a ternary solid solution of Fe in CeNi₃, unlimited solid solution between CeNi₂ and CeFe₂, and a quaternary solid solution of Fe in CeNi₄B. The measured amounts of Fe in CeNi₃ and CeNi₄B are 37-43 at.% and 16-18 at.%, respectively. Figure 4.3(g) shows a BSE micrograph of diffusion zone 3. Diffusion zone 4 is a single-phase α-Fe as shown in Figures 4.3(e-f). Next is the diffusion zone 5, which is a three-phase equilibrium among α-Fe, a ternary solid solution of Fe in Ce₂Ni₇ and a quaternary solid solution of Fe in CeNi₄B. 18-25 at.% Fe substitute Ni in Ce₂Ni₇ compound while 33-34 at.% Fe substitute Ni in CeNi₄B compound. Figure 4.3(h) shows a magnified BSE micrograph of diffusion zone 5. Diffusion zone 6 is a two-phase equilibrium between a ternary solid solution of Fe in CeNi₅ and a binary solid solution of Fe and Ni. Ternary solubility extension of CeNi₅ is 5-24 at.% Fe and 10-63 at.% Ni is measured in (Fe, Ni) solid solution. Figure 4.3(f) shows magnified micrograph of diffusion zones 3 to 6.

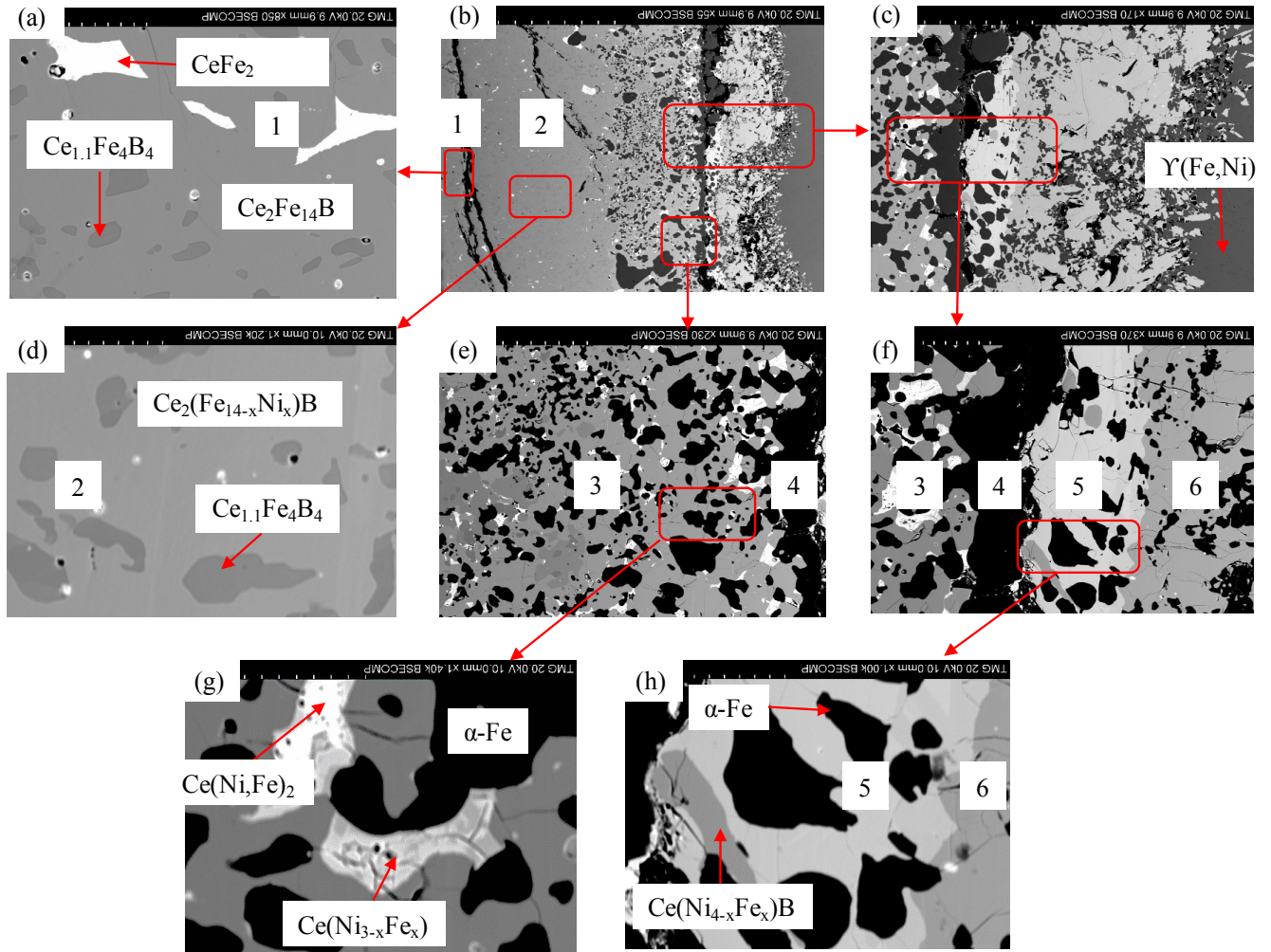


Figure 4.3: BSE micrographs of the solid-solid diffusion couple 2 in the Ce-Fe-Ni-B system.

The numbers shown on parts (a), (b), (d-f) and (h) refer to the diffusion zone numbers

Table 4.3: Phase composition obtained by WDS spot analysis on the diffusion couple 2 in Ce-Fe-Ni-B system

Diffusion zone number	Description	Phase composition (at.%)				Corresponding phase
		Ce	Fe	Ni	B	
1	Three-phase alloy (end-member)	33	67	0	0	CeFe ₂
		12	44	44	0	Ce _{1.1} Fe ₄ B ₄
		12	82	0	6	Ce ₂ Fe ₁₄ B
2	Two-phase zone	12	44	44	0	Ce _{1.1} Fe ₄ B ₄
		12	73-82	0-9	6	Ce ₂ (Fe _{14-x} Ni _x)B (0 ≤ x ≤ 1.5)
3	Four-phase zone	0	96	4	0	α-Fe
		26	37-43	31-37	0	Ce(Ni _{3-x} Fe _x) (0 ≤ x ≤ 1.72)
		33	26-35	32-41	0	Ce(Ni, Fe) ₂
		15	50-52	16-18	17	Ce(Ni _{4-x} Fe _x)B (0.19 ≤ x ≤ 0.78)
4	One-phase zone	0	95	5	0	α-Fe
5	Three-phase zone	0	91-93	7.0-9.0	0	α-Fe
		23	18-25	52-59	0	Ce ₂ (Ni _{7-x} Fe _x) (0 ≤ x ≤ 1.14)
		15	33-34	34-35	17	Ce(Ni _{4-x} Fe _x)B (0.19 ≤ x ≤ 0.78)
6	Two-phase zone	0	37-86	10-63	0	γ(Fe, Ni)
		17	5-24	59-78	0	Ce(Ni _{5-x} Fe _x) (0 ≤ x ≤ 1.44)
7	One-phase alloy (end-member)	0	31	69	0	γ(Fe, Ni)

4.1.1.3 Diffusion couple 3: Ce₁₅Fe₇₄B₁₁ – Ni₇₅B₂₅ at.%

Diffusion couple 3 was annealed at 900°C for 39 days. The end-member 1 is an alloy with actual composition of Ce₁₅Fe₇₄B₁₁ at.%. As shown in Figure 4.4(a), it contains a three-phase equilibrium among CeFe₂, Ce_{1.1}Fe₄B₄ and Ce₂Fe₁₄B, which is consistent with the Ce-Fe-B phase

diagram in Figure 2.13. The end-member 2 is a single-phase alloy of Ni₃B compound. Figure 4.4(b) shows the BSE micrograph of the end-members and diffusion zones in the diffusion couple 3. Seven diffusion layers were observed in this diffusion couple as displayed in the magnified BSE micrographs of Figure 4.4(d-f). Summary of the SEM/WDS spot analysis of the compositions of the phases and end-members is presented in Table 4.4. Based on the observed diffusion zones, the order of diffusion from the end-member 1 is deduced as: CeFe₂ + Ce_{1.1}Fe₄B₄ + Ce₂Fe₁₄B (end-member) → Ce_{1.1}Fe₄B₄ + Ce₂(Fe_{14-x}Ni_x)B (0 ≤ x ≤ 1.5) → α-Fe → Ce(Ni_{3-x}Fe_x) (0 ≤ x ≤ 1.72) + α-Fe + Ce(Ni_{4-x}Fe_x)B (0.19 ≤ x ≤ 0.78) → α-Fe + Ce(Ni_{4-x}Fe_x)B (0.19 ≤ x ≤ 0.78) + Fe₂B → Ce(Ni_{4-x}Fe_x)B (0.19 ≤ x ≤ 0.78) + Ce₂(Ni_{7-x}Fe_x) (0 ≤ x ≤ 1.14) → Ce(Ni_{4-x}Fe_x)B (0.19 ≤ x ≤ 0.78) → Ce(Ni_{4-x}Fe_x)B (0 ≤ x ≤ 0.10) → (Fe_{1-x-y}Ni_xCe_y)₂₃B₆ (0 ≤ y ≤ 0.062) (x = 0.832) → Ni₃B (end-member).

As shown in Figure 4.4(d), diffusion zone 2, which is next to the end-member 1, is a two-phase equilibrium between the Ce_{1.1}Fe₄B₄ compound and a quaternary solid solution of Ni in Ce₂Fe₁₄B. The amount of Ni measured in Ce₂Fe₁₄B is in the range of 0-9 at.%. Figure 4.4(d) shows a BSE micrograph of diffusion zone 2. Diffusion zone 3 contains a single-phase α-Fe. A BSE micrograph of diffusion zone 3 is shown in Figure 4.4(e). Diffusion zone 4 is a three-phase equilibrium, consisting of α-Fe, a ternary solid solution of Fe in CeNi₃ and a quaternary solid solution of Fe in CeNi₄B. In both CeNi₃ and CeNi₄B, the amounts of Fe substituting Ni are 37 at.% Fe and 48-53 at.% Fe, respectively. Figure 4.4(g) displays a BSE micrograph of diffusion zone 4. Next is diffusion zone 5, which is also a three-phase equilibrium but among α-Fe, Fe₂B and a quaternary solid solution of Fe in CeNi₄B. The amount of Fe measured in CeNi₄B phase is 30-47 at.%. Figure 4.4(h) displays a BSE micrograph of diffusion zone 5. Diffusion zone 6 is a two-phase layer between a ternary solid solution of Fe in Ce₂Ni₇ and a quaternary solid solution

of Fe in CeNi_4B . Concentrations of Fe in Ce_2Ni_7 and CeNi_4B are 18-24 at.% and 23–29 at.%, respectively. Figure 4.4(i) displays a BSE micrograph of diffusion zone 6. Zone 7 is a single-phase layer containing quaternary solid solution of Fe in CeNi_4B . Measured amounts of Fe in CeNi_4B are 1-7 at.% and 13-22 at.%. The gap in the compositions was observed between 7 at.% Fe and 13 at.% Fe interval. The gap observed in this solid solution is due to the shape of the homogeneity regions. The last diffusion zone is zone 8 of $(\text{Fe}, \text{Ni}, \text{Ce})_{23}\text{B}_6$ single phase. Content of Ce substituting Fe in $(\text{Fe}, \text{Ni})_{23}\text{B}_6$ phase is between 2 and 5 at.%. Figure 4.4(f) shows a BSE micrograph of diffusion zones 7 and 8.

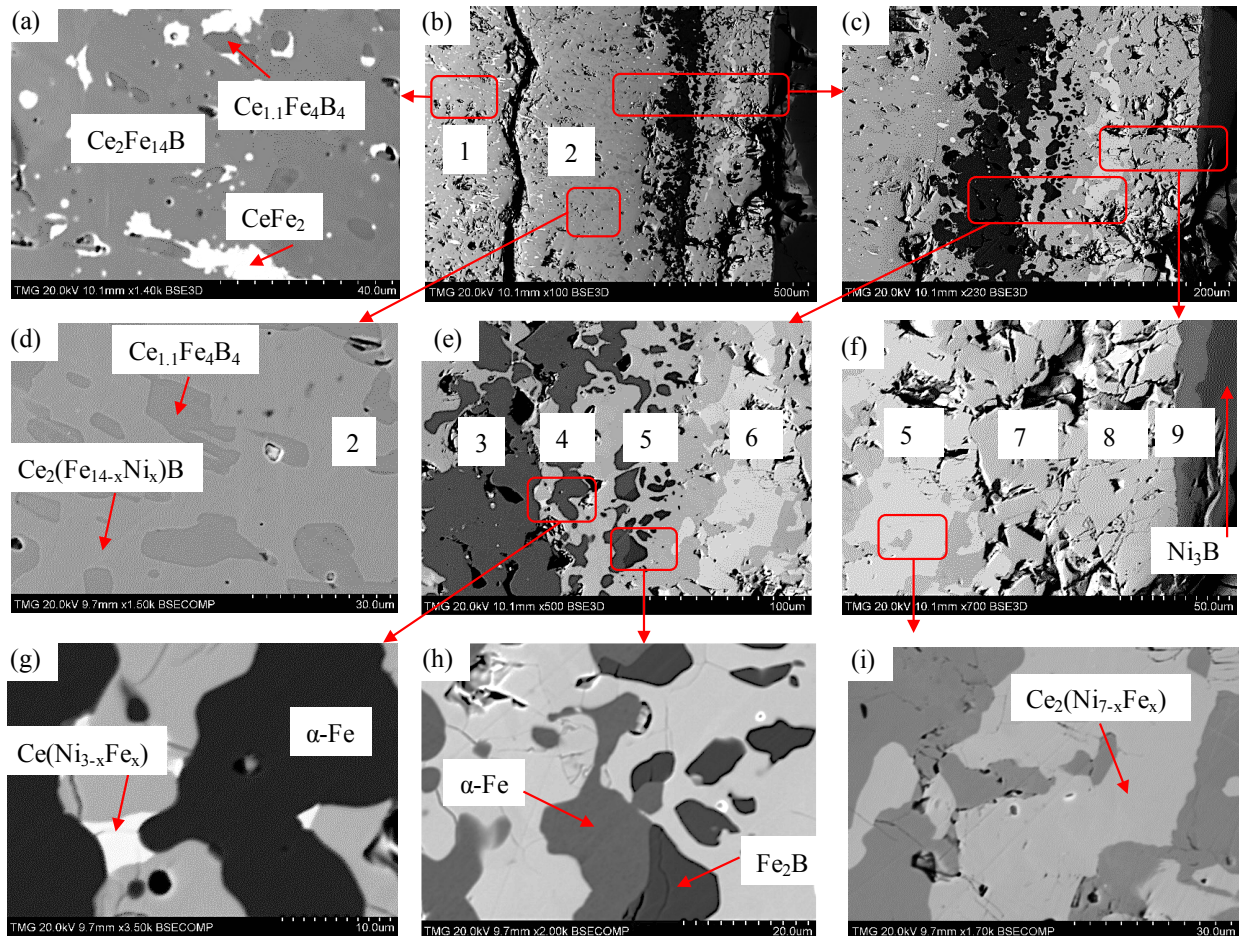


Figure 4.4: BSE micrographs of the solid-solid diffusion couple 3 in the Ce-Fe-Ni-B system.

The numbers shown on parts (b) and (d-f) refer to the diffusion zone numbers

Table 4.4: Phase composition obtained by the WDS spot analysis of diffusion couple 3 in the Ce-Fe-Ni-B system

Diffusion zone number	Description	Phase composition (at.%)				Corresponding phase
		Ce	Fe	Ni	B	
1	Three-phase alloy (end-member)	33	67	0	0	CeFe ₂
		12	44	44	0	Ce _{1.1} Fe ₄ B ₄
		12	82	0	6	Ce ₂ Fe ₁₄ B
2	Two-phase zone	12	44	44	0	Ce _{1.1} Fe ₄ B ₄
		12	73-82	0-9	6	Ce ₂ (Fe _{14-x} Ni _x)B (0 ≤ x ≤ 1.5)
3	One-phase zone	0	94-96	4.0-6.0	0	α-Fe
4	Three-phase zone	0	96	4	0	α-Fe
		26	37	37	0	Ce(Ni _{3-x} Fe _x) (0 ≤ x ≤ 1.72)
		15	48-53	15-20	17	Ce(Ni _{4-x} Fe _x)B (0.19 ≤ x ≤ 0.78)
5	Three-phase zone	0	96	4	0	α-Fe
		0	65	1	34	Fe ₂ B
		15	30-47	21-38	17	Ce(Ni _{4-x} Fe _x)B (0.19 ≤ x ≤ 0.78)
6	Two-phase zone	23	18-24	53-59	0	Ce ₂ (Ni _{7-x} Fe _x) (0 ≤ x ≤ 1.14)
		15	23-29	39-45	17	Ce(Ni _{4-x} Fe _x)B (0.19 ≤ x ≤ 0.78)
7	One-phase zone	15	13-22, 1-7	46-55, 61-67	17	Ce(Ni _{4-x} Fe _x)B (0.19 ≤ x ≤ 0.78) (0 ≤ x ≤ 0.10)
8	One-phase zone	2-5	7-10	67	21	(Fe _{1-x-y} Ni _x Ce _y) ₂₃ B ₆ (0 ≤ y ≤ 0.062) (x = 0.832)
9	One-phase alloy (end-member)	0	0	75	25	Ni ₃ B

4.1.2 Experimental results of the key alloys

Studies were carried out on the Fe-Ni side of the Ce-Fe-Ni ternary system and their results are first presented. Later in this section, the phase analysis, XRD and MFM results of the key alloys in the B-Ce-Fe-Ni quaternary system will be discussed.

4.1.2.1 Phase analysis of key alloys in the Ce-Fe-Ni ternary system

There are limited experimental data on the Ce-Fe-Ni system. It was reported that, ternary solid solution of Fe in CeNi₅ extends up to the CeNi₄Fe composition and an unlimited solid solution exists between CeNi₂ and CeFe₂ [47]. Results of the three diffusion couples discussed above revealed that, Ce₂Ni₇ and CeNi₃ intermetallics also extend into the Ce-Fe-Ni ternary system and that the extension of CeNi₅ is more than the CeNi₄Fe composition that was reported by [46, 84-86]. Based on the observation in diffusion couples, Ni-Fe side of the Ce-Fe-Ni ternary system is further investigated in this work. Five key alloys were prepared to further investigate the ternary solid solutions of Fe in CeNi₅, Ce₂Ni₇ and CeNi₃ in the Ce-Fe-Ni ternary system. Table 4.5 lists the compositions and annealing conditions of these key alloys. Figure 4.5 shows the compositions of key alloys used in studying the Ce-Fe-Ni system.

Table 4.5: The compositions and annealing times of key alloys used in studying the Ce-Fe-Ni system at 700°C

Key alloy number	Actual global composition (at.%)			Annealing time (days)
	Ce	Fe	Ni	
1	7	46	47	12
2	34	35	31	12
3	10	23	67	12
4	12	73	15	12
5	7	72	21	21

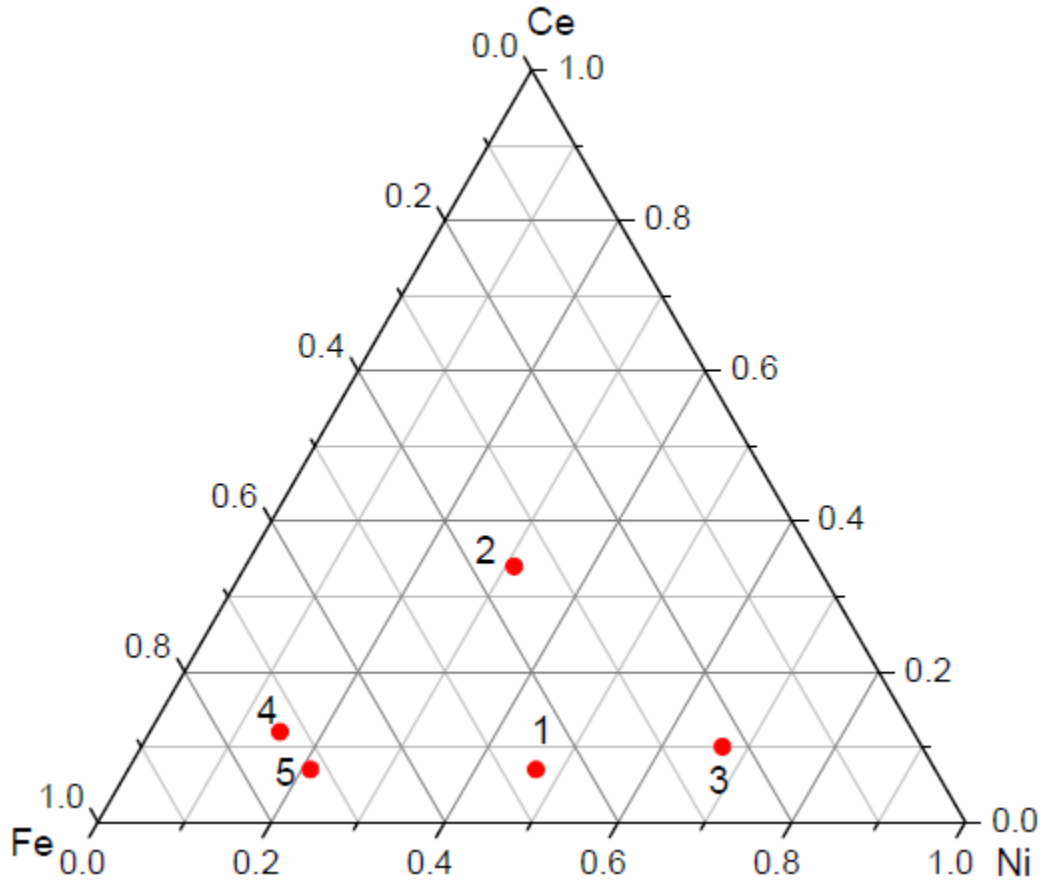


Figure 4.5: The compositions, in at.%, of the key alloys in the Ce-Fe-Ni system

A two-phase equilibrium between a ternary solid solution of Fe in CeNi_5 and a solid solution between Fe and Ni are observed in key alloy 1 after its annealing for 12 days at 700°C . The ternary solubility extension of Fe in CeNi_5 is measured as 19 at.% Fe. Figure 4.6(a) shows a BSE micrograph of key alloy 1. Key alloy 2 was annealed at 700°C for 12 days. A three-phase equilibrium among α -Fe, a ternary solid solution of Fe in CeNi_3 and an unlimited solid solution between CeNi_2 and CeFe_2 are observed. Amounts of Fe measured in CeNi_3 and CeNi_2 are 39 at.% and 30 at.%, respectively. Figure 4.6(b) shows a BSE micrograph of key alloy 2. Key alloy 3 was also annealed for 12 days at 700°C . A two-phase equilibrium between a $\gamma(\text{Fe, Ni})$ solid solution and the 7 at.% Fe in CeNi_5 solid solution is observed. After annealing key alloy 4 at 700°C for 12 days, a three-phase equilibrium among a ternary solid solution of Fe in CeNi_3 , α -Fe

and the $\text{Ce}(\text{Ni}, \text{Fe})_2$ solid solution is observed. Concentrations of measured Fe in CeNi_3 and $\text{Ce}(\text{Ni}, \text{Fe})_2$ are 41 at.% and 32 at.%, respectively. Key alloy 5 was annealed at 700°C for 21 days to make sure that equilibrium is obtained. A two-phase equilibrium between $\alpha\text{-Fe}$ and a ternary solid solution of Fe in Ce_2Ni_7 is observed. 16 at.% Fe content was measured in Ce_2Ni_7 . Table 4.6 summarizes the compositions of phases in the key alloys used in studying the Fe-Ni side of the Ce-Fe-Ni system. Based on the experimental results from the discussed five key alloys and the literature data, a partial isothermal section of the Ce-Fe-Ni ternary system at 700°C is drawn in Figure 4.7.

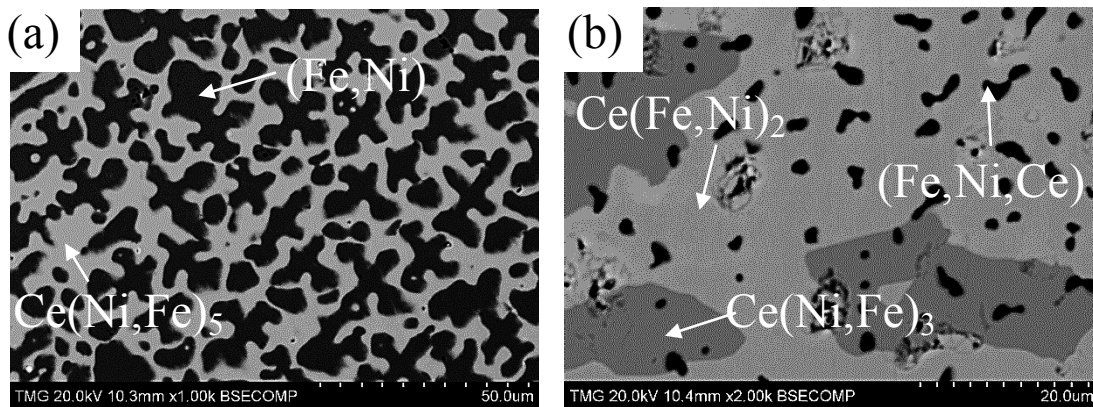


Figure 4.6: BSE micrographs of key alloys (a) 1, (b) 2

Table 4.6: Chemical analysis and the corresponding phases in key alloys 1 to 5 used in the Ce-Fe-Ni system

Key alloy number	Actual global composition (at.%)			Phase composition (at.%)			Corresponding phase
	Ce	Fe	Ni	Ce	Fe	Ni	
1	7	46	47	17	19	64	Ce(Ni, Fe) ₅
				0	62	38	(Fe, Ni)
2	34	35	31	33	30	37	Ce(Ni, Fe) ₂
				2	97	1	α-Fe
				25	39	36	Ce(Ni, Fe) ₃
3	10	23	67	17	7	76	Ce(Ni, Fe) ₅
				1	41	58	(Fe, Ni)
4	12	73	15	33	32	35	Ce(Ni, Fe) ₂
				25	41	34	Ce(Ni, Fe) ₃
				1	98	1	α-Fe
5	7	72	21	22	16	62	Ce ₂ (Ni, Fe) ₇
				1	95	4	α-Fe

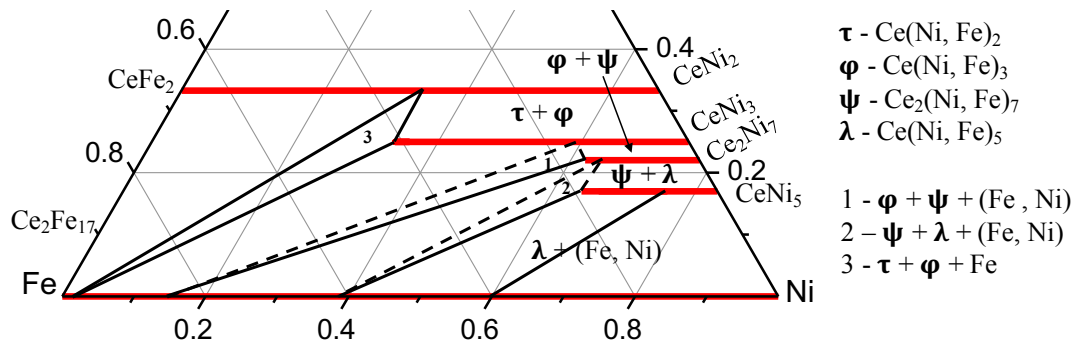


Figure 4.7: Partial isothermal section of the Ce-Fe-Ni system at 700°C

4.1.2.2 Phase analysis of key alloys in the Ce-Fe-Ni-B quaternary system

18 key alloys were prepared to further investigate quaternary solubility extensions of the Ce₂Fe₁₄B, CeNi₄B and (Fe, Ni)₂₃B₆ phases. Table 4.7 shows the compositions and annealing

conditions of these key alloys. Annealing time was increased for the alloys which did not reach equilibrium after 10 days annealing as shown in Table 4.7. Figure 4.8 shows the compositions of the key alloys used in studying the Ce-Fe-Ni-B system.

Table 4.7: Compositions and annealing times of key alloys used in studying the Ce-Fe-Ni-B system at 900°C

Key alloy number	Actual global composition (at.%)				Annealing time (days)
	Ce	Fe	Ni	B	
1	12	81	1	6	10
2	12	65	17	6	10
3	12	76	6	6	31
4	12	74	8	6	10
5	12	73	9	6	10
6	12	68	14	6	10
7	15	9	59	17	11
8	15	21	46	18	31
9	15	27	40	18	31
10	14	35	35	16	10
11	15	43	25	17	10
12	15	50	18	17	10
13	15	53	14	18	10
14	15	55	12	18	10
15	1	11	68	20	11
16	2	10	67	21	32
17	5	7	67	21	42
18	6	2	60	32	22

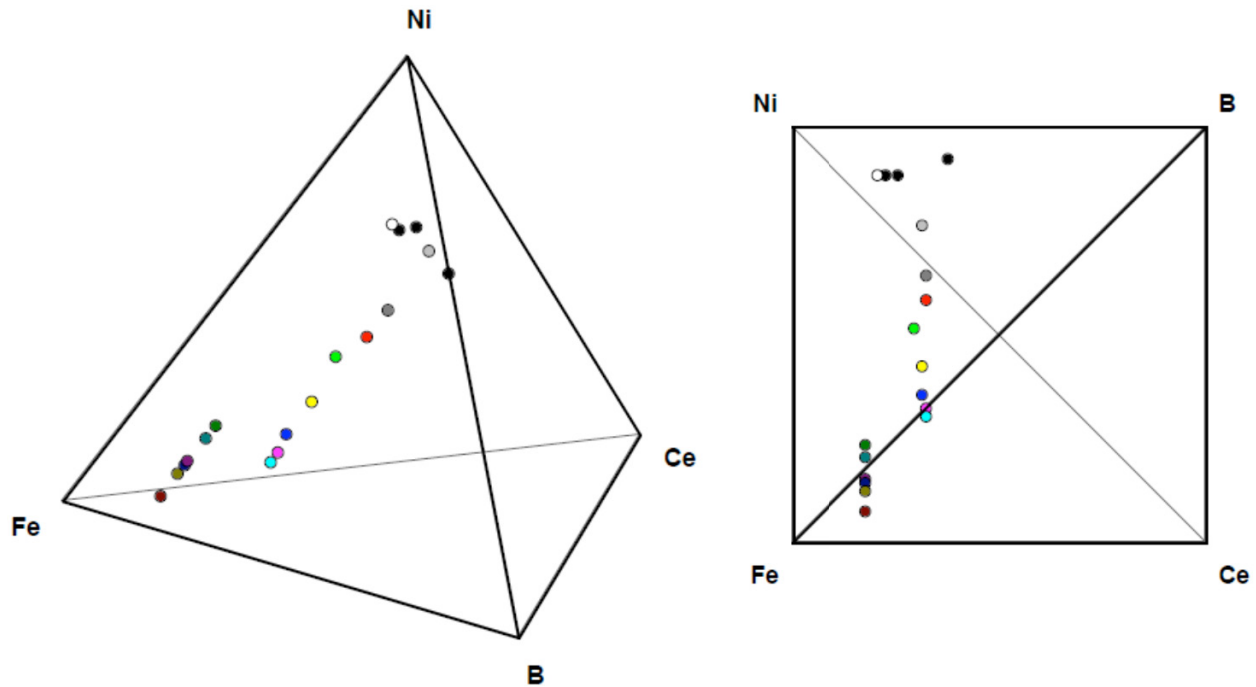


Figure 4.8: The compositions of the key alloys in the Ce-Fe-Ni-B system

4.1.2.2.1 Phase analysis of key alloys 1 to 6

To verify and further investigate the quaternary solid solubility of Ni in $\text{Ce}_2\text{Fe}_{14}\text{B}$, key alloys 1-6 were prepared. After key alloys 1 and 2 were annealed for 10 days at 900°C , a three-phase equilibrium among $\alpha\text{-Fe}$, $\text{Ce}_{1.1}\text{Fe}_4\text{B}_4$ and a quaternary solid solution of Ni in $\text{Ce}_2\text{Fe}_{14}\text{B}$ was observed. Ni contents measured in $\text{Ce}_2\text{Fe}_{14}\text{B}$ are 1 at.% and 4 at.% for key alloys 1 and 2, respectively. Figure 4.9(a) shows a BSE micrograph of key alloy 1. Key alloy 3 was first annealed at 900°C for 10 days. However, four phases among $\alpha\text{-Fe}$, a ternary solid solution of Fe in CeNi_3 , $\text{Ce}(\text{Fe},\text{Ni})_2$ solid solution and a quaternary solid solution of Fe in CeNi_4B are observed. Further annealing of this alloy for additional 21 days at 900°C resulted in a three-phase equilibrium among $\alpha\text{-Fe}$, $\text{Ce}_{1.1}\text{Fe}_4\text{B}_4$ and quaternary solid solution of Ni in $\text{Ce}_2\text{Fe}_{14}\text{B}$. This shows that the annealing of 10 days did not achieve equilibrium. Ni concentration in $\text{Ce}_2\text{Fe}_{14}\text{B}$ was measured as 6 at.%. Figures 4.9(b) and 4.9(c) show BSE micrographs of key alloy 3 after

annealing at 900°C for 10 and 31 days, respectively. Key alloy 4 was annealed for 10 days at 900°C. A four-phase equilibrium among α -Fe, $Ce_{1.1}Fe_4B_4$, $Ce(Fe, Ni)_2$ solid solution and a quaternary solid solution of Ni in $Ce_2Fe_{14}B$ was observed. Fe amount in $Ce(Fe, Ni)_2$ was measured as 28 at.% while Ni amount in $Ce_2Fe_{14}B$ was measured as 8 at.%. Figure 4.9(d) shows a BSE micrograph of key alloy 4. A four-phase equilibrium was observed in key alloy 5 after annealing at 900°C for 10 days. Observed phases are α -Fe, $Ce_{1.1}Fe_4B_4$, $Ce(Fe, Ni)_2$ solid solution and a quaternary solid solution of Ni in $Ce_2Fe_{14}B$. 25 at.% Fe and 9 at.% Ni concentrations were measured in $Ce(Fe, Ni)_2$ and $Ce_2Fe_{14}B$, respectively. After annealing key alloy 6 at 900°C for 10 days, a three-phase equilibrium among α -Fe, $Ce_{1.1}Fe_4B_4$ compound and a quaternary solid solution of Ni in $Ce_2Fe_{14}B$ was observed. Ni content in $Ce_2Fe_{14}B$ phase was measured as 9 at.%. Table 4.8: lists the compositions of the phases obtained by WDS in the above-mentioned key alloys

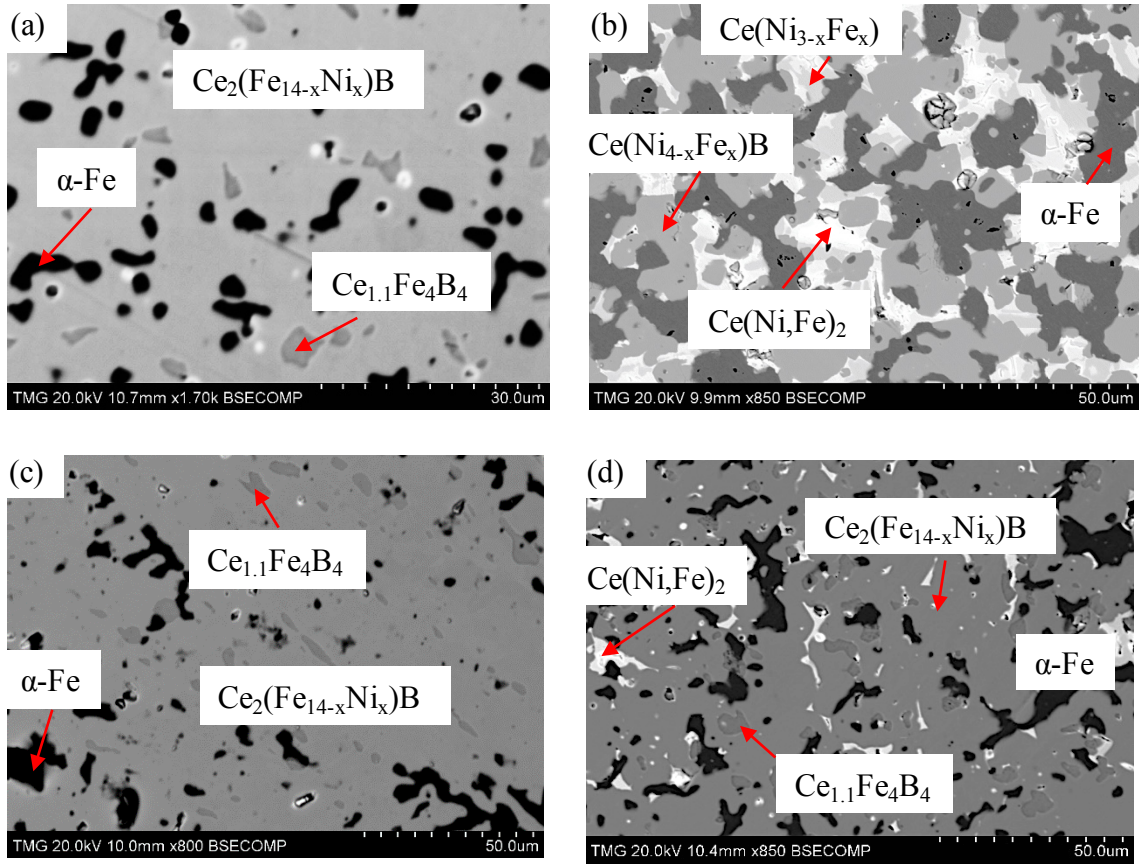


Figure 4.9: BSE micrographs of key alloys (a) 1, (b) 3 after 10 days annealing, (c) 3 after 31 days annealing, (d) 4

Table 4.8: Chemical analysis and the corresponding phases in key alloys 1 to 6

Key alloy number	Actual global composition (at.%)				Phase composition (at.%)				Corresponding phase
	Ce	Fe	Ni	B	Ce	Fe	Ni	B	
1	12	81	1	6	12	81	1	6	Ce ₂ (Fe, Ni) ₁₄ B
					12	44	0	44	Ce _{1.1} Fe ₄ B ₄
					5	94	1	0	α-Fe
2	12	65	17	6	12	78	4	6	Ce ₂ (Fe, Ni) ₁₄ B
					12	44	0	44	Ce _{1.1} Fe ₄ B ₄
					1	98	1	0	α-Fe
3	12	76	6	6	12	76	6	6	Ce ₂ (Fe, Ni) ₁₄ B
					12	44	0	44	Ce _{1.1} Fe ₄ B ₄
					1	91	8	0	α-Fe
4	12	74	8	6	12	74	8	6	Ce ₂ (Fe, Ni) ₁₄ B
					12	44	0	44	Ce _{1.1} Fe ₄ B ₄
					1	96	3	0	α-Fe
					34	28	38	0	Ce(Fe, Ni) ₂
5	12	73	9	6	12	73	9	6	Ce ₂ (Fe, Ni) ₁₄ B
					12	44	0	44	Ce _{1.1} Fe ₄ B ₄
					1	95	4	0	α-Fe
					34	25	41	0	Ce(Fe, Ni) ₂
6	12	68	14	6	12	73	9	6	Ce ₂ (Fe, Ni) ₁₄ B
					12	44	0	44	Ce _{1.1} Fe ₄ B ₄
					1	97	2	0	α-Fe

4.1.2.2.2 Phase analysis of key alloys 7 to 14

Key alloys 7 to 14 were prepared to verify the quaternary solid solubility of Fe in CeNi₄B observed in the diffusion couples. Table 4.7 shows the annealing conditions and actual compositions obtained by ICP of these key alloys. A two-phase equilibrium was observed in key alloy 7 after annealing at 900°C for 11 days. These phases are a quaternary solid solution of Fe in CeNi₄B and a binary solid solution between Fe and Ni. Concentration of Fe in CeNi₄B is measured as 5 at.%. Figure 4.10(a) shows a BSE micrograph of key alloy 7. Key alloys 8 and 9

were annealed at 900°C for 31 days. Two-phase equilibrium between a quaternary solid solution of Fe in CeNi₄B and the Fe₂B compound was observed in both key alloys. Amounts of Fe measured in CeNi₄B of key alloys 8 and 9 are 14 at.% and 24 at.%, respectively. After key alloy 10 was annealed at 900°C for 10 days, a three-phase equilibrium among a quaternary solid solution of Fe in CeNi₄B, the Fe₂B compound and a ternary solid solution of Fe in Ce₂Ni₇ was observed. Quaternary solubility extension in CeNi₄B compound is 28 at.% Fe. Figure 4.10(b) shows a BSE micrograph of key alloy 10. Key alloy 11 was annealed at 900°C for 10 days and a two-phase equilibrium between a quaternary solid solution of Fe in CeNi₄B and Fe₂B was observed. The extension of quaternary solubility of Fe in CeNi₄B was measured as 42 at.%. After annealing key alloy 12 for 10 days at 900°C, a three-phase equilibrium among a quaternary solid solution of Fe in CeNi₄B, a ternary solid solution of Fe in CeNi and α-Fe was observed. Amounts of Fe measured in CeNi₄B and CeNi are 50 at.% and 4 at.%, respectively. Figure 4.10(c) shows a BSE micrograph of key alloy 12. Key alloy 13 was annealed at 900°C for 10 days. A three-phase equilibrium among a quaternary solid solution of Ni in Ce₂Fe₁₄B, a quaternary solid solution of Fe in CeNi₄B and the Ce_{1.1}Fe₄B₄ compound, was observed. 9 at.% of Ni concentration was measured in Ce₂Fe₁₄B and 52 at.% of Fe was measured in CeNi₄B. After key alloy 14 was annealed at 900°C for 10 days, a four-phase equilibrium among a quaternary solid solution of Ni in Ce₂Fe₁₄B, a quaternary solid solution of Fe in CeNi₄B, the Ce(Fe, Ni)₂ solid solution and the Ce_{1.1}Fe₄B₄ compound was observed. Respective quaternary solubility extensions of Ce₂Fe₁₄B and CeNi₄B are found to be 9 at.% Ni and 53 at.% Fe. Figure 4.10(d) shows a BSE micrograph of key alloy 14. Table 4.9 shows the phase compositions determined by WDS of key alloys 7 to 14.

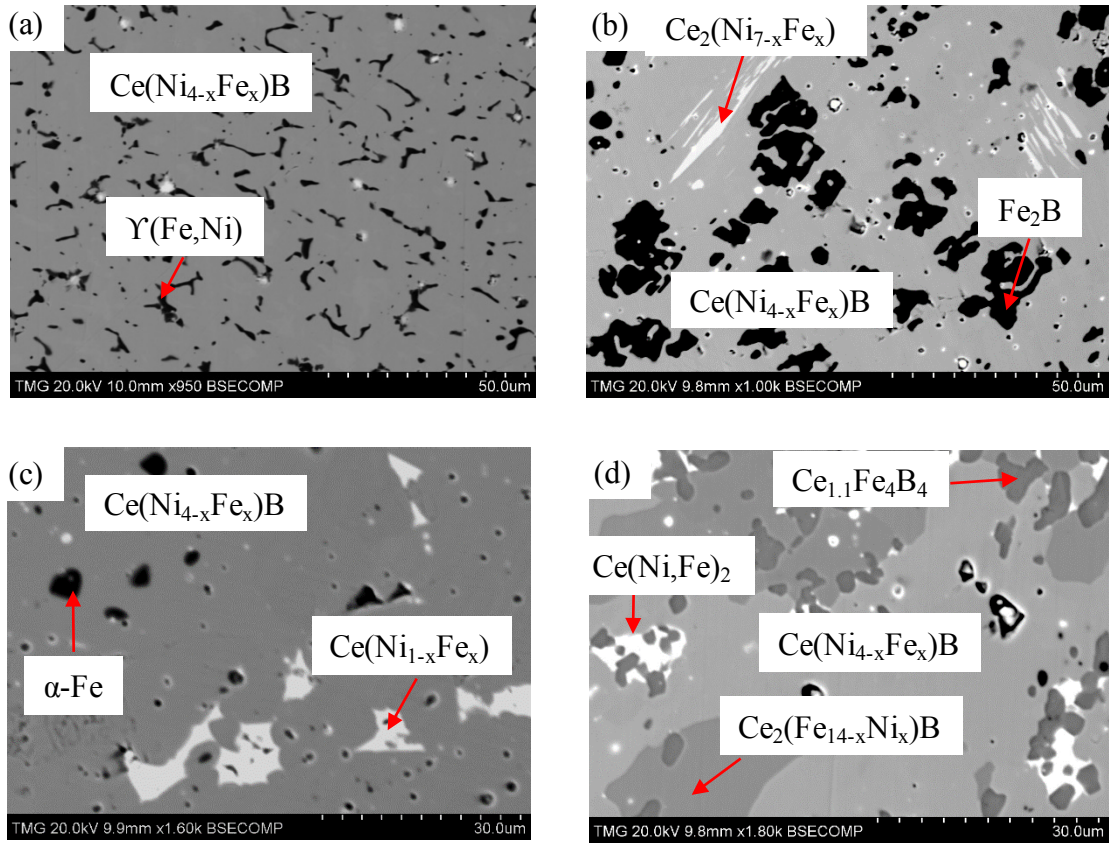


Figure 4.10: BSE micrographs of key alloys (a) 7, (b) 10, (c) 12, (d) 14

Table 4.9: Chemical analysis and the corresponding phases in key alloys 7 to 14

Key alloy number	Actual global composition (at.%)				Phase composition (at.%)				Corresponding phase
	Ce	Fe	Ni	B	Ce	Fe	Ni	B	
7	15	9	59	17	15	5	63	17	Ce(Ni, Fe) ₄ B
					1	55	44	0	(Fe, Ni)
8	15	21	46	18	15	14	54	17	Ce(Ni, Fe) ₄ B
					2	67	5	26	(Fe, Ni, Ce) ₂ B
9	15	27	40	18	15	24	44	17	Ce(Ni, Fe) ₄ B
					1	68	2	29	(Fe, Ni, Ce) ₂ B
10	14	35	35	16	15	28	40	17	Ce(Ni, Fe) ₄ B
					0	67	0	33	Fe ₂ B
					23	20	57	0	Ce ₂ (Ni, Fe) ₇
11	15	43	25	17	15	42	26	17	Ce(Ni, Fe) ₄ B
					1	65	1	33	(Fe, Ni, Ce) ₂ B
12	15	50	18	17	15	50	18	17	Ce(Ni, Fe) ₄ B
					50	4	46	0	Ce(Ni, Fe)
					1	94	5	0	α-Fe
13	15	53	14	18	12	73	9	6	Ce ₂ (Fe, Ni) ₁₄ B
					15	52	16	17	Ce(Ni, Fe) ₄ B
					12	44	0	44	Ce _{1.1} Fe ₄ B ₄
14	15	55	12	18	12	73	9	6	Ce ₂ (Fe, Ni) ₁₄ B
					15	53	15	17	Ce(Ni, Fe) ₄ B
					12	44	0	44	Ce _{1.1} Fe ₄ B ₄
					31	28	41	0	Ce(Fe, Ni) ₂

4.1.2.2.3 Phase analysis of key alloys 15 to 18

Monnier et al. [98] investigated the (Fe, Ni)₂₃B₆ phase and confirmed its occurrence with Fe_{4.5}Ni_{18.5}B₆ composition. Stadelmaier et al. [99] reported Fe₃Ni₂₀B₆ composition and stated that it is a metastable compound that solidifies from the melt. Diffusion zone 9 of the diffusion couple 3 revealed the (Fe, Ni)₂₃B₆ phase, which is stabilized by substituting Fe with 2-5 at.% Ce.

Key alloys 15 to 18 were prepared to further investigate $(\text{Fe, Ni, Ce})_{23}\text{B}_6$ and Table 4.5 shows the actual global compositions and annealing conditions of these key alloys.

Key alloy 15 was prepared and annealed at 900°C for 11 days. A BSE micrograph of Figure 4.11(a) displays four distinct phases. Compositions of the three phases, except dark morphologies of $(\text{Ni, Fe, Ce})_3\text{B}$ phase, are very close and they all belong to the $(\text{Fe, Ni, Ce})_{23}\text{B}_6$ quaternary solid solution. The varying contents of Ce measured in the $(\text{Fe, Ni})_{23}\text{B}_6$ are 1, 2 and 3 at.%. Same occurrence of varying close concentration of Ce in the $(\text{Fe, Ni})_{23}\text{B}_6$ phase was observed in key alloys 16 and 17. A three-phase equilibrium was observed in key alloy 16 after annealing at 900°C for 32 days. From the XRD and SEM/WDS results, two of the phases show a quaternary solid solution of Ce in $(\text{Fe, Ni})_{23}\text{B}_6$ and the third phase is a ternary solid solution of Fe in Ni_3B . Figure 4.11(b) shows a BSE micrograph of key alloy 16. After annealing key alloy 17 for 10 days at 900°C , non-equilibrium five phases were observed. Further 32 days annealing resulted in a three-phase equilibrium in which two phases belong to quaternary solid solution of Ce in $(\text{Fe, Ni})_{23}\text{B}_6$ and the third phase is a quaternary solid solution of Fe in $\text{CeNi}_{12}\text{B}_6$. Figure 4.11(c) shows a BSE micrograph of key alloy 17 after 42 days annealing. Key alloy 18 was prepared and annealed for 22 days at 900°C . A three-phase equilibrium among a quaternary solid solution of Fe in CeNi_4B , a quaternary solid solution of Ce in $(\text{Fe, Ni})_{23}\text{B}_6$ and a quaternary solid solution of Fe in $\text{CeNi}_{12}\text{B}_6$ was observed. 1 at.% Fe was measured in both $\text{CeNi}_{12}\text{B}_6$ and CeNi_4B , while 6 at.% Ce concentration was measured in $(\text{Fe, Ni})_{23}\text{B}_6$. Figure 4.11(d) shows a BSE micrograph of key alloy 18. Table 4.10 shows the compositions of the phases in key alloys 15 to 18.

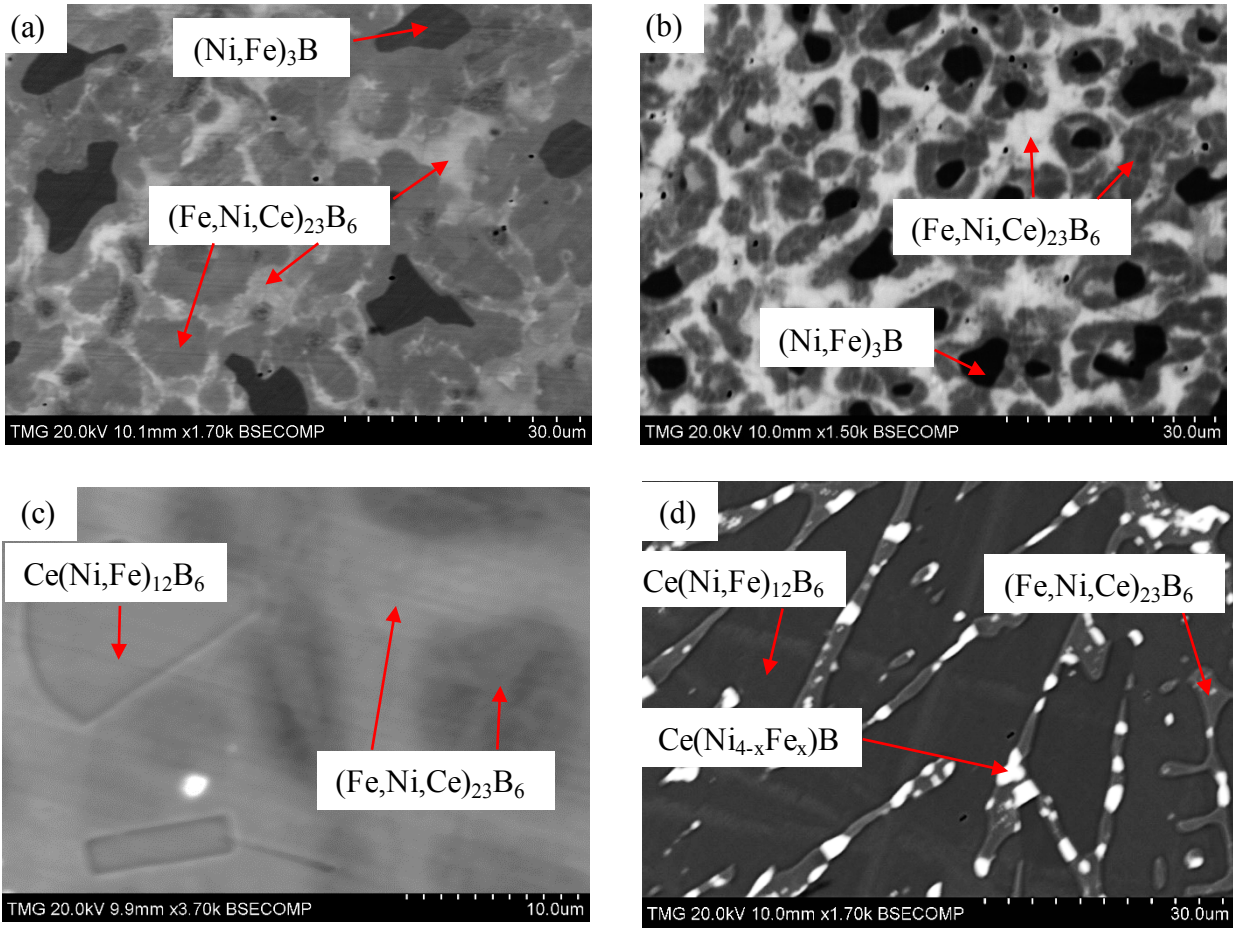


Figure 4.11: BSE micrographs of key alloys (a) 15, (b) 16, (c) 17, (d) 18

Table 4.10: Chemical analysis and the corresponding phases in key alloys 15 to 18

Key alloy number	Actual global composition (at.%)				Phase composition (at. %)				Corresponding phase
	Ce	Fe	Ni	B	Ce	Fe	Ni	B	
15	1	11	68	20	3	9	67	21	(Fe, Ni, Ce) ₂₃ B ₆
					1	12	67	20	(Fe, Ni, Ce) ₂₃ B ₆
					2	11	67	20	(Fe, Ni, Ce) ₂₃ B ₆
					0	7	68	25	(Ni, Fe) ₃ B
16	2	10	67	21	4	8	67	21	(Fe, Ni, Ce) ₂₃ B ₆
					1	12	67	20	(Fe, Ni, Ce) ₂₃ B ₆
					0	8	67	25	(Ni, Fe) ₃ B
17	5	7	67	21	5	7	67	21	(Fe, Ni, Ce) ₂₃ B ₆
					3	10	66	21	(Fe, Ni, Ce) ₂₃ B ₆
					6	2	60	32	Ce(Ni, Fe) ₁₂ B ₆
18	6	2	60	32	6	1	60	33	Ce(Ni, Fe) ₁₂ B ₆
					6	6	67	21	(Fe, Ni, Ce) ₂₃ B ₆
					15	1	67	17	Ce(Ni, Fe) ₄ B

4.1.2.2.4 XRD analyses of the Ce-Fe-Ni-B key alloys

XRD analyses were performed on key alloys 1 to 18. Si was used as an internal calibration standard to correct the zero shift and specimen surface displacement. The analyses were to verify the crystal structures and phase equilibria of the phases observed using SEM/WDS. Ce₂(Fe, Ni)₁₄B solid solution observed in key alloys 1 to 6 crystallizes in tetragonal structure with P4₂/mm space group and Nd₂Fe₁₄B prototype. The peak positions shift to higher angle with decreasing Fe content. The substitution of Fe by Ni, which has a smaller atomic radius, decreases the unit cell parameters of Ce₂Fe₁₄B. This is confirmed by the increase of the 2θ values of the peak positions as the Ni concentration increases. Example of the Ce₂(Fe, Ni)₁₄B solid solution XRD pattern can be found in Figure 4.12(a-b), which corresponds to key alloys 3 and 5. Ce(Fe,

Ni)₂ solid solution, which was observed in key alloys 4 and 5, has MgCu₂ prototype and Fd-3m space group. XRD analysis of the Ce(Ni, Fe)₄B solid solution, which was observed in key alloys 7 to 14, shows that it crystallizes in hexagonal structure with P6/mmm space group and CeCo₄B prototype. Example of XRD pattern of the Ce(Ni, Fe)₄B solid solution can be found in Figure 4.12(c), which corresponds to key alloy 11. The Ce₂(Fe, Ni)₁₄B and Ce(Ni, Fe)₄B solid solutions identified in key alloys by SEM/WDS analysis were confirmed by XRD analysis. SEM/WDS study of (Fe, Ni, Ce)₂₃B₆ phase has shown that it has varying Ce and Fe concentrations as observed in key alloys 15 to 18. To further study (Fe, Ni, Ce)₂₃B₆ phase, XRD analysis was carried out on these key alloys. XRD results show that the varying concentrations of Ce and Fe in (Fe, Ni, Ce)₂₃B₆ phase corresponds to the same crystal structure, which crystallizes in face-centered cubic structure with Fm-3m space group and Cr₂₃C₆ prototype. Example of XRD pattern of the (Fe, Ni, Ce)₂₃B₆ solid solution is shown in Figure 4.12(d), which corresponds to key alloy 16.

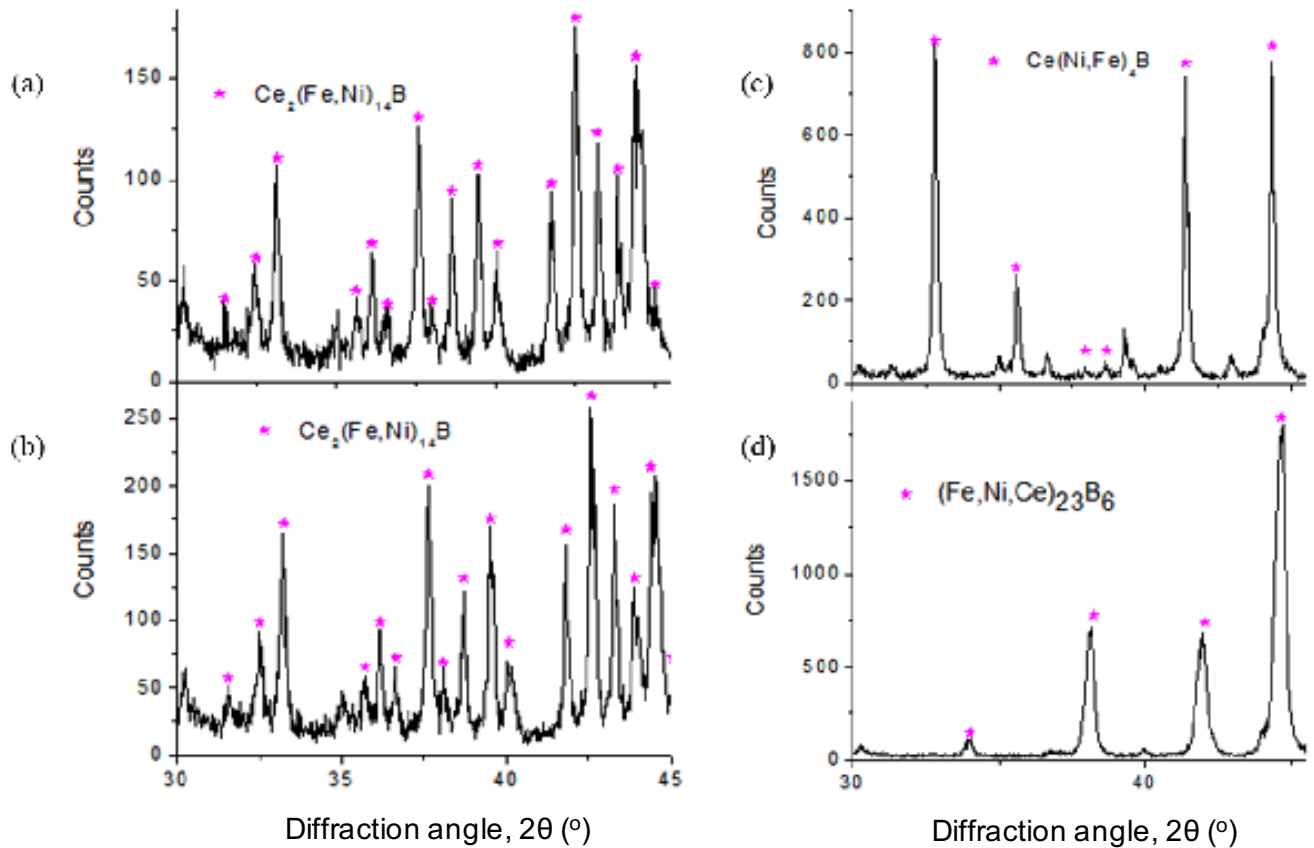


Figure 4.12: XRD pattern of key alloys (a) 3, (b) 5, (c) 11, (d) 16

4.1.3 MFM characterization of phases at the Fe-Ni side of the Ce-Fe-Ni-B system

To identify the magnetic phases at the Fe-Ni side of the Ce-Fe-Ni-B system, MFM was used to screen out non-magnetic phases. Under MFM test, it is known that the magnetic phase produces contrast of magnetic domains while non-magnetic phase has no magnetic domains. The parameters, (scan size for example) used for obtaining MFM micrographs during MFM tests are the same for all the key alloys. From the results of diffusion couples and key alloys prepared for investigating the Fe-Ni side of the Ce-Fe-Ni-B system, three quaternary solid solutions were observed. These are $(\text{Fe, Ni, Ce})_{23}\text{B}_6$, $\text{Ce}(\text{Ni, Fe})_4\text{B}$ and $\text{Ce}_2(\text{Fe, Ni})_{14}\text{B}$. MFM analysis was carried out at different compositions of each solid solution. Only $\text{Ce}_2(\text{Fe}_{14-x}\text{Ni}_x)\text{B}$ ($0 \leq x \leq 1.5$) solid solution shows visible contrast for the magnetic domains. Figure 4.13 shows the

compositions of the key alloys and Table 4.11 lists the compositions and annealing conditions of the selected key alloys used for MFM analysis of the magnetic $\text{Ce}_2(\text{Fe}_{14-x}\text{Ni}_x)\text{B}$ ($0 \leq x \leq 1.5$) solid solution. Figure 4.14 shows examples of MFM micrographs in the $\text{Ce}_2(\text{Fe}_{14-x}\text{Ni}_x)\text{B}$ ($0 \leq x \leq 1.5$) solid solubility range at various Ni concentrations.

Table 4.11: Compositions and annealing conditions of the selected key alloys used for MFM characterization of the $\text{Ce}_2(\text{Fe}_{14-x}\text{Ni}_x)\text{B}$ solid solution annealed at 900°C

Key alloy number	Actual global composition (at.%)				Annealing time (days)
	Ce	Fe	Ni	B	
1	12	81	1	6	10
2	12	65	17	6	10
3	12	76	6	6	31
4	12	74	8	6	10
5	12	73	9	6	10

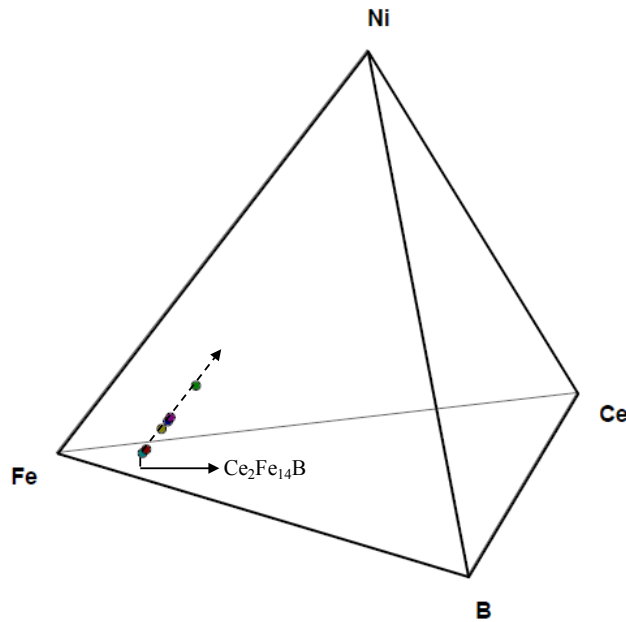


Figure 4.13: Compositions of the selected key alloys used for MFM characterization of the $\text{Ce}_2(\text{Fe}_{14-x}\text{Ni}_x)\text{B}$ solid solution. The arrow represents increasing Ni direction

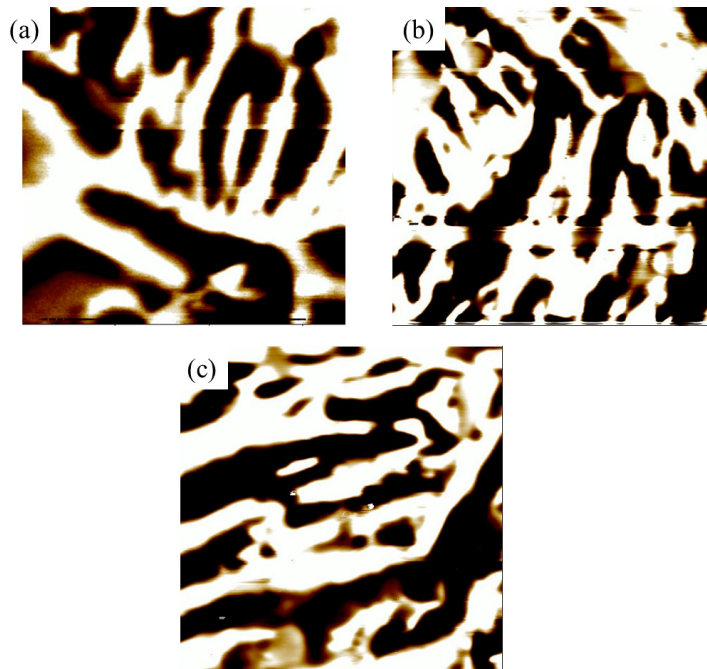


Figure 4.14: MFM magnetic domain micrographs of key alloys (a) 1, (b) 2, (c) 5. Scan size of each micrograph is 30 μm

4.1.4 Intrinsic magnetic properties of the $\text{Ce}_2\text{Fe}_{14}\text{B}$ modified by Ni compound

Four key alloys have been used to study the effect of Ni on the intrinsic magnetic properties of $\text{Ce}_2\text{Fe}_{14}\text{B}$. The percentage volume of the $\text{Ce}_2\text{Fe}_{14}\text{B}$ dissolving different amounts of Ni in each key alloy is greater than 70 %. The saturation magnetizations (M_s) were obtained in external magnetic fields of up to 50 kOe at 298 K. The anisotropy fields (H_A) were determined, using second derivative of magnetization (d^2M/dH^2), by singular point detection (SPD) method. The magnetic measurements of the key alloys 1 to 4, which cover the homogeneity range of $\text{Ce}_2(\text{Fe}_{14-x}\text{Ni}_x)\text{B}$ solid solution, were determined and compared with $\text{Ce}_2\text{Fe}_{14}\text{B}$ reference alloy, number 0 in Table 4.12. Table 4.12 shows compositions and magnetic properties of alloys prepared within the homogeneity range of the $\text{Ce}_2(\text{Fe}_{14-x}\text{Ni}_x)\text{B}$ solid solution. Figures 4.15 to 4.17 show the

respective plots of the composition dependences of saturation magnetizations, anisotropy fields and Curie temperature of the $\text{Ce}_2(\text{Fe}_{14-x}\text{Ni}_x)\text{B}$ solid solution. These results will be discussed in the next section.

Table 4.12: Magnetic properties of the $\text{Ce}_2(\text{Fe}_{14-x}\text{Ni}_x)\text{B}$ solid solution

Key alloy number	Ni addition (at.%)	M_S (emu/g) at 298 K	H_A (kOe) at 298 K	T_C ($^{\circ}\text{C}$)
0	0	130.0	28.1	151
1	1	127.9	27.1	159
2	3	124.3	26.1	174
3	6	114.8	24.1	197
4	9	106.3	24.1	210

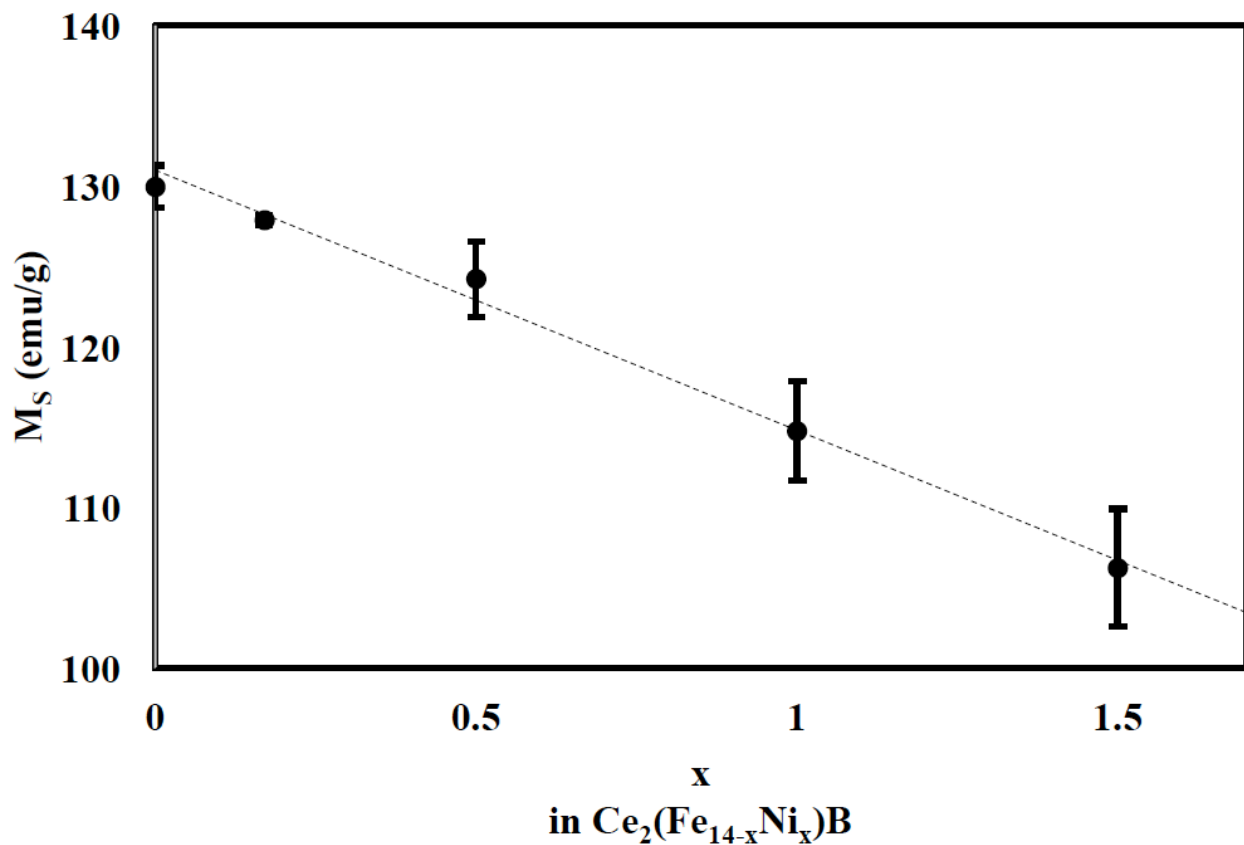


Figure 4.15: The composition dependence of the saturation magnetization (M_S) of the $\text{Ce}_2(\text{Fe, Ni})_{14}\text{B}$ solid solution at 298 K

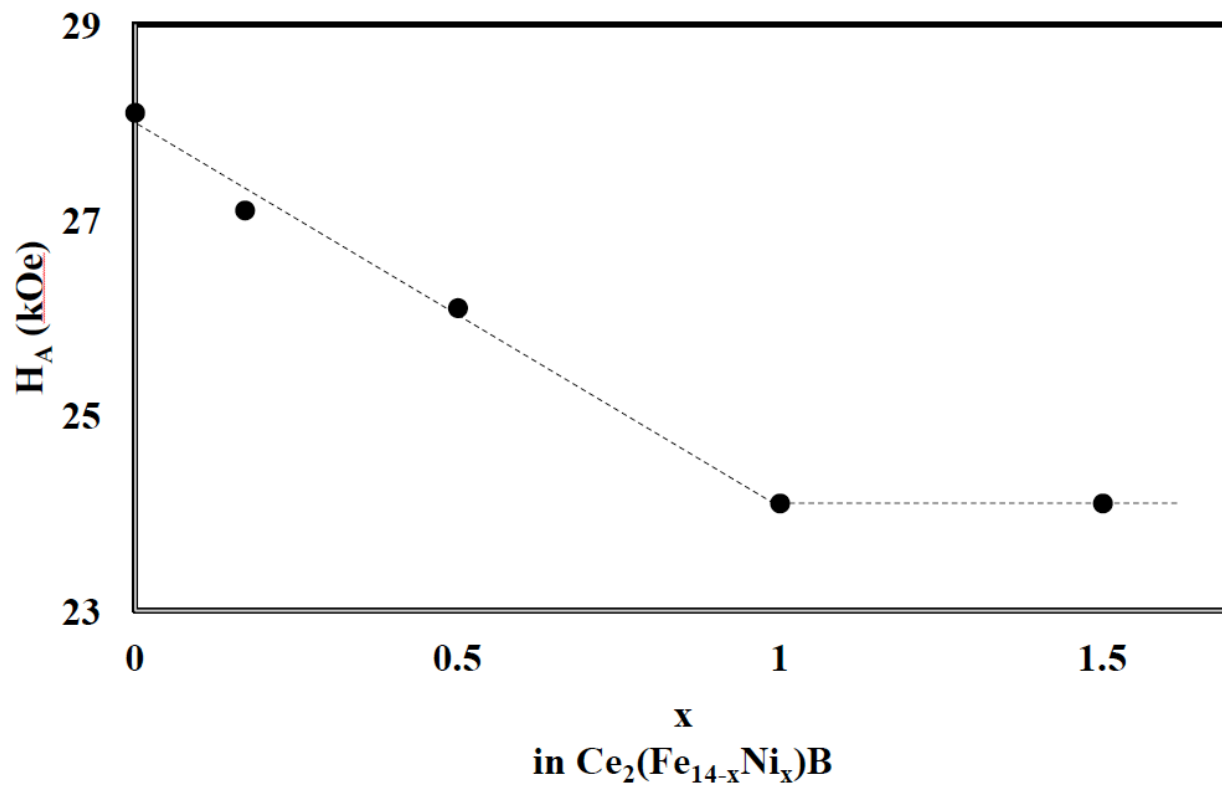


Figure 4.16: The composition dependence of the anisotropy field (H_A) of the $\text{Ce}_2(\text{Fe}, \text{Ni})_{14}\text{B}$ solid solution at 298 K

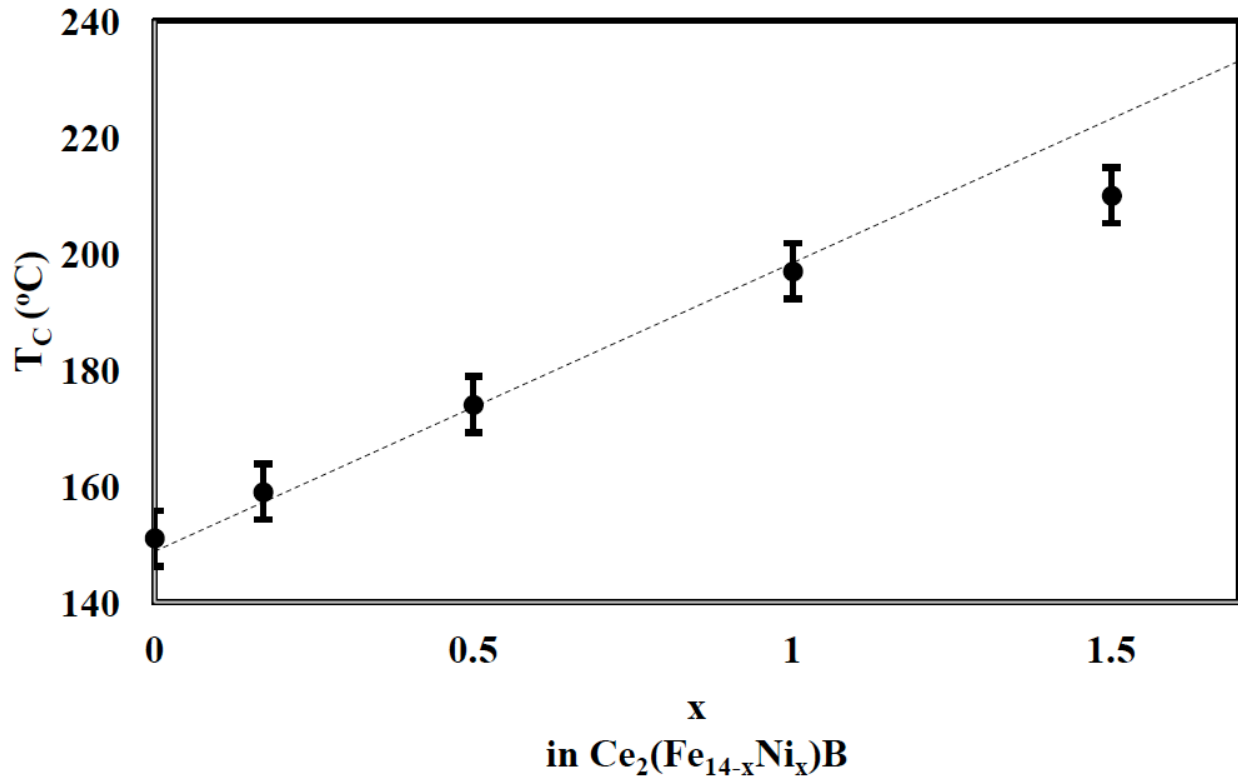


Figure 4.17: The composition dependence of the Curie temperature (T_C) of the $Ce_2(Fe, Ni)_{14}B$ solid solution

4.1.5 Discussion of the results of the Ce-Fe-Ni-B quaternary system

Fe-Ni side of the Ce-Fe-Ni-B quaternary system has been investigated using 3 diffusion couples and 18 key alloys at 900°C. Quaternary extensions of $Ce_2Fe_{14}B$, $CeNi_{14}B$ and $(Fe_{1-x}Ni_x)_{23}B_6$ phases were observed in the diffusion couples. Key alloys were prepared and analyzed to verify and further investigate the compositions and structures of the phases observed in the diffusion couples.

There is limited experimental data on the Ce-Fe-Ni ternary system in the literature. No phase diagram of this system could be found in the literature and it has not been fully investigated yet. Therefore, in this work, the Ce-Fe-Ni system has been partially investigated, focusing on the Fe-Ni side. Investigation was performed in order to further verify the ternary extensions of the Ce-

Ni intermetallics observed in the diffusion couples and key alloys used while studying the Ce-Fe-Ni-B quaternary system. Annealing temperature of 700^oC was selected for key alloys in order to avoid formation of liquid in the Ce-Fe-Ni system. In this work, CeNi₃ and Ce₂Ni₇ compounds have been confirmed to extend into the Ce-Fe-Ni ternary system. Also, the ternary solid solution of Fe in CeNi₅, which was reported to extend to the CeNi₄Fe composition [46, 86], was not observed in this work. Although the exact determination of maximum ternary solid solutions of Fe in CeNi₃, Ce₂Ni₇ and CeNi₅ is not the purpose of this work, it has been confirmed that, ternary solid solution of Fe in CeNi₃, Ce₂Ni₇ and CeNi₅ compounds extend to at least 41 at.% Fe, 16 at.% Fe and 19 at.% Fe, respectively at 700^oC. The results from the three diffusion couples used in studying Ce-Fe-Ni-B quaternary systems at 900^oC have shown that, the ternary solid solutions of Fe in CeNi₃, Ce₂Ni₇ and CeNi₅ compounds extend to at least 43 at.% Fe, 25 at.% Fe and 24 at.% Fe, respectively. These results are self-supportive as Fe/Ni atomic exchange is expected to increase by increasing the temperature from 700^oC to 900^oC.

Ni quaternary solubility in the Ce₂Fe₁₄B compound was observed in the three diffusion couples used in studying Fe-Ni side of the Ce-Fe-Ni-B system at 900^oC. In the diffusion couples, homogeneity range of Ni in the Ce₂Fe₁₄B compound is between 0 and 9 at.% Ni. Key alloys 1 to 6 were prepared to confirm and further investigate the quaternary extension of the Ce₂Fe₁₄B compound observed in the diffusion couples. Results of the key alloys confirm the homogeneity range of the Ce₂Fe₁₄B quaternary solid solution in the Ce-Fe-Ni-B quaternary system to be between 0 and 9 at.% Ni. Since the maximum solubility is 9 at.% Ni, the corresponding formula, which represents the amount of measured Ni in this solid solution, is written as Ce₂(Fe_{14-x}Ni_x)B (0 ≤ x ≤ 1.5). XRD analysis of the Ce₂(Fe_{14-x}Ni_x)B solid solution confirms the Ni substitution

and shows that the compound crystallizes in tetragonal structure with $P4_2/mnm$ space group and $Nd_2Fe_{14}B$ prototype.

Quaternary solid solubility of Fe in the $CeNi_4B$ compound was detected in diffusion couples used in studying Fe-Ni side of the Ce-Fe-Ni-B quaternary system at $900^\circ C$. Solubilities of Fe measured in $CeNi_4B$ from the diffusion couples are 1–7 at.% Fe and 13–53 at.% Fe. The interval between 7 and 13 at.% Fe was not detected in the diffusion couples. Key alloys 7 to 14 were prepared to verify these findings. Key alloys' results confirm the compositions of the $Ce(Ni_{1-x}Fe_x)_4B$ solid solution obtained from the diffusion couples. The gap in the homogeneity range (between 7 and 13 at.% Fe) can be due to the shape of the solid solution single phase region in the quaternary system. However, because the $Ce(Ni_{1-x}Fe_x)_4B$ solid solution has no potential for PM material, the exact determination of its homogeneity range is not the purpose of this work. The corresponding formula is written as $Ce(Ni_{1-x}Fe_x)_4B$ ($0 \leq x \leq 0.10$) and ($0.19 \leq x \leq 0.78$) at $900^\circ C$. XRD study of this solid solution confirms that it crystallizes in hexagonal structure with $P6/mmm$ space group and $CeCo_4B$ prototype.

Quaternary solid solubility of Ce in $(Fe_{1-x}Ni_x)_{23}B_6$ phase was observed in diffusion couple 3. Contents of 2 to 5 at.% Ce was measured in $(Fe_{1-x}Ni_x)_{23}B_6$ from the diffusion couples. Key alloys 15 to 18 were used to verify and further investigate the quaternary solid solubility of Fe in $(Fe_{1-x}Ni_x)_{23}B_6$. Varying concentrations of Ce and Fe were measured in the $(Fe_{1-x-y}Ni_xCe_y)_{23}B_6$ solid solution in key alloys 15 to 18 using the SEM/WDS analysis ranging from 6 to 12 at.% Fe and from 1 to 6 at.% Ce. XRD study shows that the varying concentrations of Ce and Fe measured in the $(Fe_{1-x-y}Ni_xCe_y)_{23}B_6$ corresponds to the same crystal structure, which crystallizes in face-centered cubic structure with $Fm-3m$ space group and $Cr_{23}C_6$ prototype. This shows that $(Fe_{1-x-y}Ni_xCe_y)_{23}B_6$ is a solid solution which has a wide homogeneity range of Ce between 0 and 6

at.%. Therefore, the corresponding formula of this solid solution at 900°C is written as $(\text{Fe}_{1-x-y}\text{Ni}_x\text{Ce}_y)_{23}\text{B}_6$, where $0 \leq y \leq 0.062$ and $x = 0.832$.

Out of $\text{Ce}_2\text{Fe}_{14}\text{B}$, CeNi_4B and $(\text{Fe}_{1-x}\text{Ni}_x)_{23}\text{B}_6$ ternary phases which were observed to extend into the Ce-Fe-Ni-B quaternary system, only $\text{Ce}_2\text{Fe}_{14}\text{B}$ quaternary extension has been identified to exhibit magnetic domains in the MFM micrographs. Besides, the $\text{Ce}_2\text{Fe}_{14}\text{B}$ ternary compound has been reported to have potential for PM [72], and the visible contrast of its domains confirms this report. The observed magnetic domain structure in the $\text{Ce}_2(\text{Fe}_{14-x}\text{Ni}_x)\text{B}$ solid solution is an indication of a permanent magnet. After using MFM to screen out non-magnetic $\text{Ce}(\text{Ni}_{1-x}\text{Fe}_x)_4\text{B}$ and $(\text{Fe}_{1-x-y}\text{Ni}_x\text{Ce}_y)_{23}\text{B}_6$ solid solutions at the Fe-Ni side of the Ce-Fe-Ni-B quaternary system, quantitative experimental investigation to determine intrinsic magnetic properties of the $\text{Ce}_2(\text{Fe}_{14-x}\text{Ni}_x)\text{B}$ solid solution was carried out at different Ni concentrations. Various studies have been carried out on how Ni influences magnetic properties of $\text{RE}_2\text{Fe}_{14}\text{B}$ compound, other than $\text{Ce}_2\text{Fe}_{14}\text{B}$, in the literature [14, 99–103]. To verify the intrinsic magnetic properties of pure $\text{Ce}_2\text{Fe}_{14}\text{B}$ compound and to study the effect of modifying this compound by Ni, saturation magnetization, anisotropy field and Curie temperature of $\text{Ce}_2\text{Fe}_{14}\text{B}$ were determined. The anisotropy field of pure $\text{Ce}_2\text{Fe}_{14}\text{B}$ reported in the literature is 26 kOe [94, 95]. After the correction of the demagnetization field contribution, the obtained value of anisotropy field of $\text{Ce}_2\text{Fe}_{14}\text{B}$ in this work is 28.1 kOe. As illustrated in Figure 4.15, saturation magnetization decreases almost linearly with increasing Ni concentration in the $\text{Ce}_2(\text{Fe}, \text{Ni})_{14}\text{B}$ solid solution. This behaviour is in agreement with the other studied $\text{RE}_2(\text{Fe}, \text{Ni})_{14}\text{B}$ solid solutions reported in [14, 99-100, 102-103]. In this work, it is observed that the saturation magnetizations decrease by about 3 emu/g for each 1 at.% substitution of Fe by Ni. As shown in Figure 4.16, increasing Ni substitution of Fe in $\text{Ce}_2\text{Fe}_{14}\text{B}$ compound decreases anisotropy field up to $x = 1$ (6 at.%).

Anisotropy field becomes constant at $x \geq 1$ (6 at.%). It is observed that the anisotropy field decreases by about 0.67 kOe for each 1 at.% substitution of Fe by Ni. Effects of Ni addition on the Curie temperature of RE₂Fe₁₄B series, except Ce₂Fe₁₄B, have been investigated in the past [14, 99, 103]. They all reported that Ni addition to RE₂Fe₁₄B series results in increasing of the Curie temperature. The same trend is observed for the addition of Ni to Ce₂Fe₁₄B compound in this work. As shown in Figure 4.17, increasing concentration of Ni substituting Fe in Ce₂Fe₁₄B compound increases the Curie temperature linearly. It is determined that the substitution leads to an increase of about 7.7°C per 1 at.% Ni.

From a practical perspective, the highest Curie temperature of 210°C and the associated reductions in the saturation magnetization and anisotropy field observed at $x = 1.5$ (9 at.% Ni) in the Ce₂(Fe_{14-x}Ni_x)B solid solution may still deem this Ni doped compound to be promising for the permanent magnet materials, comparing with 151°C Curie temperature of the un-doped Ce₂Fe₁₄B.

4.2 Ce-Fe-Si-B system

Both diffusion couple and key alloy techniques were used to experimentally investigate the effect of Si interaction with the Ce-Fe-B system. In this section, results of SEM/WDS, XRD and MFM will be first explained and discussion of the results will then follow in a separate subsection 4.2.5.

4.2.1 Solid-solid diffusion couples

Three diffusion couples were used in investigating Fe-Si side of the Ce-Fe-Si-B system. Diffusion couples 1 and 2 will be discussed in details while diffusion couple 3, which shows similar diffusion path to diffusion couple 2, will not be discussed. The compositions of the end-members of these diffusion couples and their annealing conditions are listed in Table 4.13.

Figure 4.18 shows the compositions of the diffusion couples, in two views, in the Ce-Fe-Si-B system.

Table 4.13: Terminal compositions and annealing times of the diffusion couples used to study the Ce-Fe-Si-B system at 900°C

Diffusion couple (DC)	End-member 1 (at.%)	End-member 2	Annealing time (days)
1	Ce ₁₅ Fe ₇₄ B ₁₁ (at.%)	Fe ₇₂ Si ₂₈	36
2	Ce ₁₀ Fe ₈₂ B ₈	Si	31
3	Ce ₁₂ Fe ₇₂ B ₁₆	Si	21

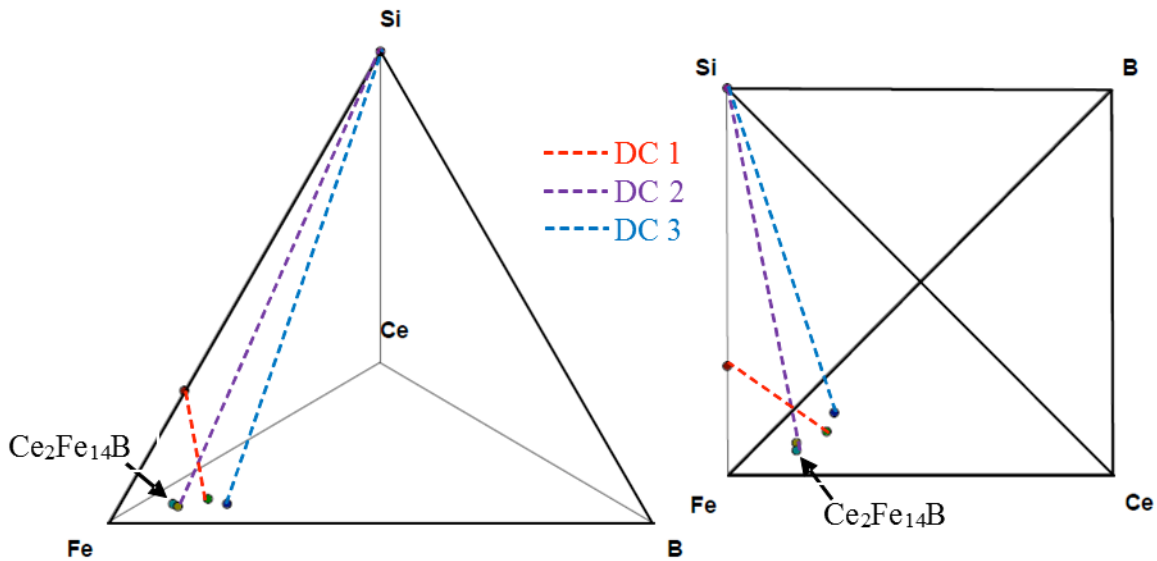


Figure 4.18: Compositions of the diffusion couples in the Ce-Fe-Si-B system

4.2.1.1 Diffusion couple 1: Fe₃Si - Ce₁₅Fe₇₄B₁₁ at.%

End-member 1 contains a three-phase equilibrium among Ce_{1.1}Fe₄B₄, Ce₂Fe₁₄B and CeFe₂, which is in accord with the Ce-Fe-B phase diagram shown in Figure 2.13. Figure 4.19(a) shows a

BSE micrograph of end-member 1. End-member 2 is Fe₃Si single phase. A BSE micrograph of end-member 2 is shown in Figures 4.19(e). After annealing diffusion couple 1 for 36 days at 900°C, five diffusion layers were observed and WDS spot analysis was carried out to determine the composition of phases present in these layers. The results obtained from WDS spot analysis are summarized in Table 4.14. Figure 4.19(c-e) displays the magnified micrographs of layers and phases in diffusion couple 1. The order of the diffusion layers from end-member 1 is indicated as: Ce_{1.1}Fe₄B₄ + CeFe₂ + Ce₂Fe₁₄B (end-member) → Ce_{1.1}Fe₄B₄ + Ce₂(Fe_{14-x}Si_x)B (0 ≤ x ≤ 2.33) → Ce₃(Si_{2-x}Fe_x) (0 ≤ x ≤ 0.1) → CeFeSi → CeFe₂Si₂ → Ce(Fe_{13-x}Si_x) (3.5 ≤ x ≤ 5) → Fe₃Si (end-member).

As shown in the magnified BSE micrograph in Figures 4.19(c-d), diffusion zone 2 is a two-phase equilibrium between Ce_{1.1}Fe₄B₄ and a quaternary solid solution of Si in Ce₂Fe₁₄B. Concentration of Si in the Ce₂Fe₁₄B compound is between 0 and 11 at.%. Diffusion zone 3 is Ce₃Si₂ ternary extension, in which Si is substituted by 2 at.% of Fe. Diffusion zones 4 and 5 belong to CeFeSi and CeFe₂Si₂ compounds, respectively. Diffusion zone 6 is a single phase of the ternary solubility extension of Si in CeFe₁₃ with 33 at.% Si.

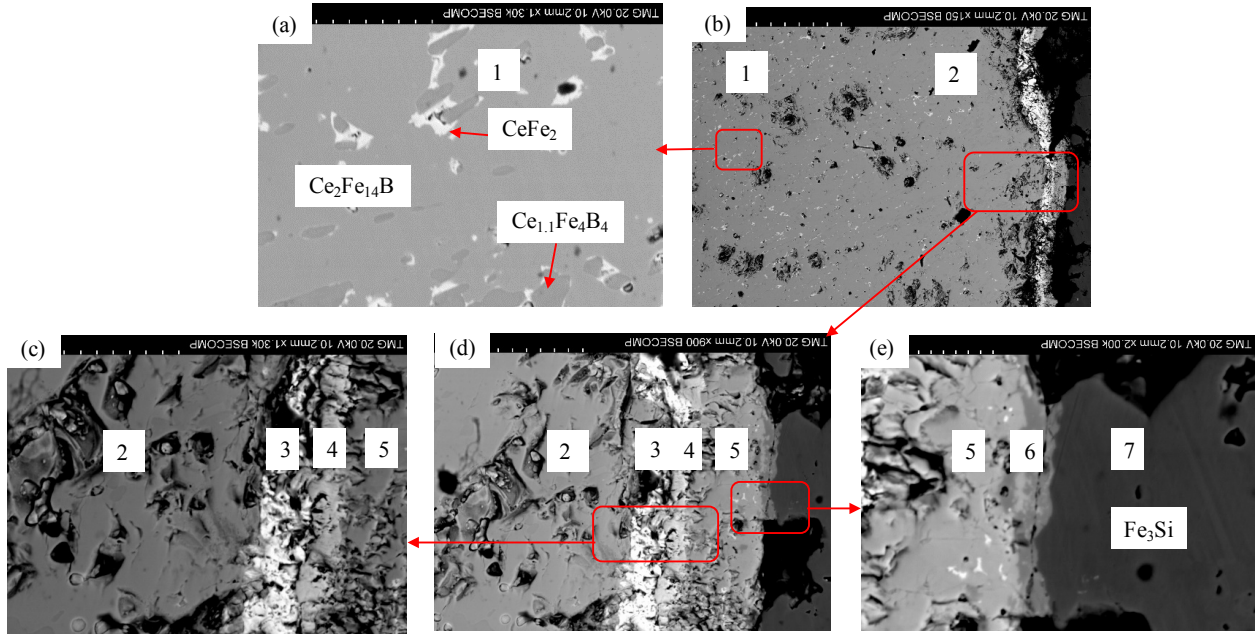


Figure 4.19: BSE micrographs of the solid-solid diffusion couple 1 in the Ce-Fe-Si-B system. The numbers shown on parts (a-e) refer to the diffusion zone numbers

Table 4.14: Phase composition obtained by WDS spot analysis on diffusion couple 1 in the Ce-Fe-Si-B system

Diffusion zone number	Description	Phase composition (at.%)				Corresponding phase
		Ce	Fe	Si	B	
1	Three phase alloy (end-member)	12	82	0	6	Ce ₂ Fe ₁₄ B
		12	44	0	44	Ce _{1.1} Fe ₄ B ₄
		35	65	0	0	CeFe ₂
2	Two-phase zone	12	44	0	44	Ce _{1.1} Fe ₄ B ₄
		12	71-82	0-11	6	Ce ₂ (Fe _{14-x} Si _x)B (0 ≤ x ≤ 2.33)
3	Single-phase zone	61	2	37	0	Ce ₃ (Si _{2-x} Fe _x) (0 ≤ x ≤ 0.1)
4	Single-phase zone	34	32	34	0	CeFeSi
5	Single-phase zone	20	40	40	0	CeFe ₂ Si ₂
6	Single-phase zone	7	60	33	0	Ce(Fe _{13-x} Si _x) (3.5 ≤ x ≤ 5)
7	Single-phase alloy (end-member)	0	72	28	0	Fe ₃ Si

4.2.1.2 Diffusion couple 2: Ce₁₀Fe₈₂B₈ at.% - Si

End-member 1 is an alloy of Ce₁₀Fe₈₂B₈ actual global composition. As shown in Figure 4.20(a), it contains α -Fe, Ce_{1.1}Fe₄B₄ and Ce₂Fe₁₄B which is agreement with the Ce-Fe-B phase diagram shown in Figure 2.13. End-member 2 is pure Si. After annealing diffusion couple 2 at 900°C for 31 days, five diffusion layers were observed as displayed in Figure 4.20(b-d). WDS spot analysis was performed on the observed layers and the results are summarized in Table 4.15. The order of diffusion from the end-member 1 is: α -Fe + Ce_{1.1}Fe₄B₄ + Ce₂Fe₁₄B (end-

member) $\rightarrow \alpha\text{-Fe} + \text{Ce}_{1.1}\text{Fe}_4\text{B}_4 + \text{Ce}_2(\text{Fe}_{14-x}\text{Si}_x)\text{B}$ ($0 \leq x \leq 2.33$) $\rightarrow \text{CeFe}_2\text{Si}_2 \rightarrow \text{CeFe}_2\text{Si}_2 + \text{Ce}(\text{Fe}_{13-x}\text{Si}_x)$ ($3.5 \leq x \leq 5$) $\rightarrow \text{Fe}_3\text{Si} \rightarrow \text{FeSi} \rightarrow \text{Si}$ (end-member)

As shown in Figure 4.18(c), diffusion zone 2, which follows end-member 1, contains $\alpha\text{-Fe}$, $\text{Ce}_{1.1}\text{Fe}_4\text{B}_4$ and a quaternary solid solution of Si in $\text{Ce}_2\text{Fe}_{14}\text{B}$. Quaternary solubility extension of $\text{Ce}_2\text{Fe}_{14}\text{B}$ was measured as 12 at.% Si. Diffusion zone 3 contains single phase of CeFe_2Si_2 . Figure 4.20(c) shows a BSE micrograph of diffusion zones 2 and 3. Diffusion zone 4 is a two-phase equilibrium between a ternary solid solution of Si in CeFe_{13} and CeFe_2Si_2 . The amount of measured Si in this phase is 32 at.%. Diffusion zone 5 is a single phase of Fe_3Si . Before the Si end-member is the last diffusion zone 6 and it is a single-phase of FeSi . Figure 4.20(d) shows a BSE micrograph of diffusion zones 4, 5 and 6.

The results of diffusion couple 3 confirmed those obtained by diffusion couple 2 because they both had similar diffusion path.

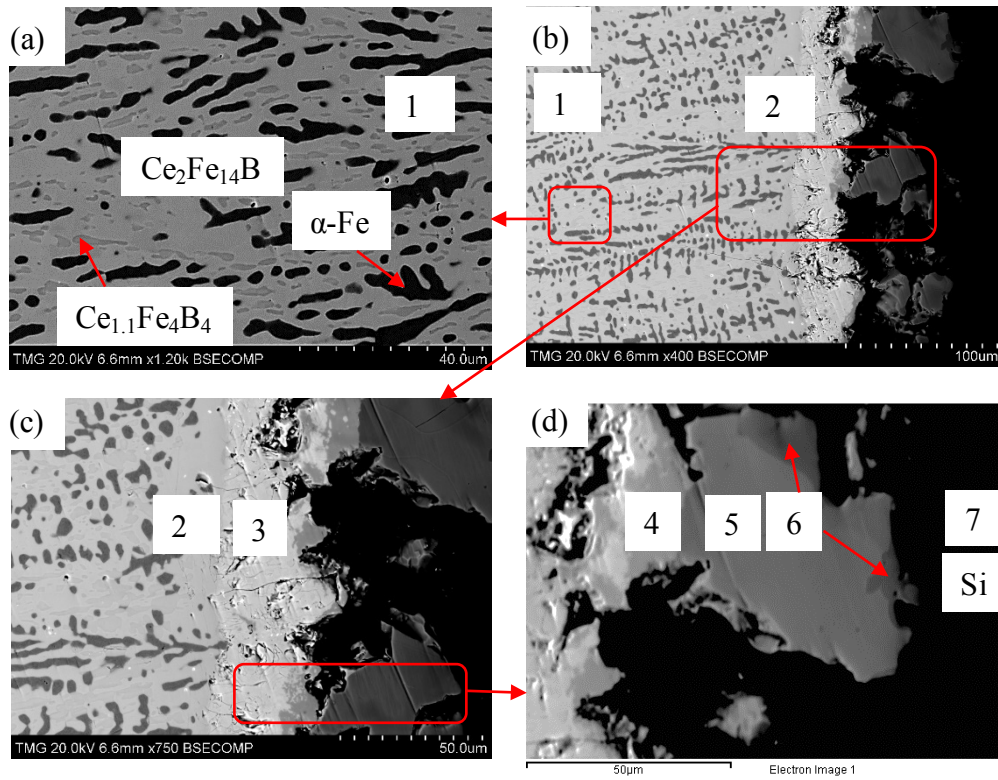


Figure 4.20: BSE micrographs of the solid-solid diffusion couple 2 in the Ce-Fe-Si-B system. The numbers shown on parts (b-d) refer to the diffusion zone numbers

Table 4.15: Phase composition obtained by WDS spot analysis on diffusion couple 2 in the Ce-Fe-Si-B system

Diffusion zone number	Description	Phase composition (at.%)				Corresponding phase
		Ce	Fe	Si	B	
1	Three-phase alloy (end-member)	12	82	0	6	Ce ₂ Fe ₁₄ B
		12	44	0	44	Ce _{1.1} Fe ₄ B ₄
		1	99	0	0	α-Fe
2	Three-phase zone	12	70-82	0-12	6	Ce ₂ (Fe _{14-x} Si _x)B (0 ≤ x ≤ 2.33)
		12	44	0	44	Ce _{1.1} Fe ₄ B ₄
		1-2	95-98	0-4	0	α-Fe
3	One-phase zone	20	40	40	0	CeFe ₂ Si ₂
4	Two-phase zone	7	61	32	0	Ce(Fe _{13-x} Si _x) (3.5 ≤ x ≤ 5)
		20	40	40	0	CeFe ₂ Si ₂
5	One-phase zone	0	72	28	0	Fe ₃ Si
6	One-phase zone	0	48	52	0	FeSi
7	Pure Si (end-member)	0	0	100	0	Si

4.2.2 Experimental results of the key alloys

4.2.2.1 Phase analysis of key alloys 1 to 8

Based on the experimental results obtained from the three diffusion couples, 8 key alloys were prepared to confirm and further investigate the Ce₂(Fe, Si)₁₄B solid solution in the Ce-Fe-Si-B system. Table 4.16 summarizes the compositions and annealing conditions of these 8 key alloys. Figure 4.21 shows the compositions of the key alloys used in studying the Ce-Fe-Si-B system.

Table 4.16: Compositions and annealing time of key alloys used in studying the Ce-Fe-Si-B system at 900°C

Key alloy number	Actual global composition (at.%)				Annealing time (days)
	Ce	Fe	Si	B	
1	12	81	1	6	21
2	13	79	3	5	10
3	13	76	6	5	10
4	13	73	9	5	10
5	13	70	12	5	10
6	12	68	14	6	10
7	13	67	15	5	10
8	14	66	15	5	10

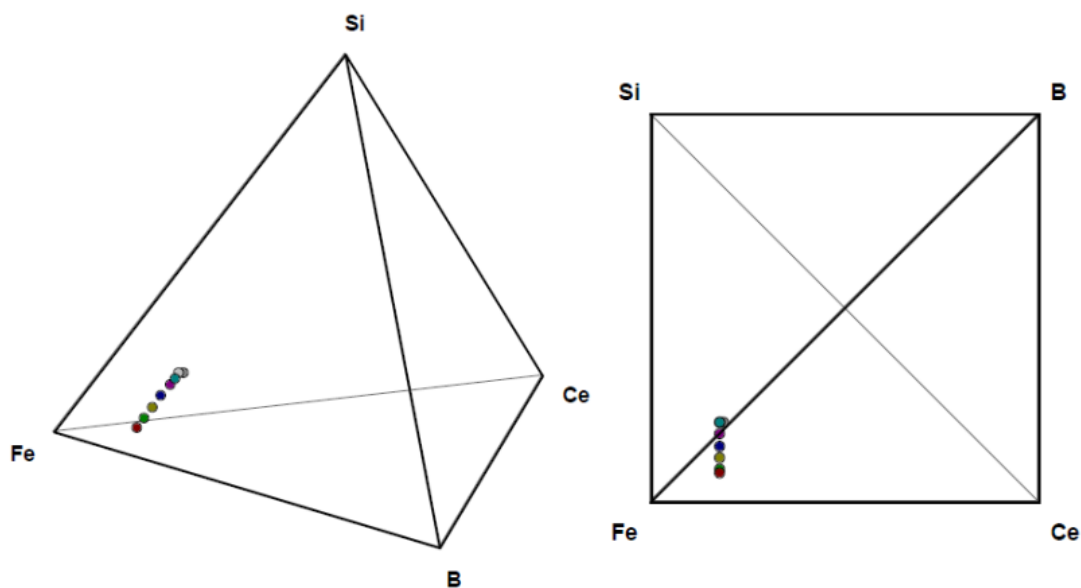


Figure 4.21: The compositions of the key alloys in the Ce-Fe-Si-B system

From the experimental results of the diffusion couples, the $Ce_2Fe_{14}B$ ternary compound was observed to extend into the Ce-Fe-Si-B quaternary system by dissolving Si and the amount of Si substituting Fe was measured between 0 and 12 at.%. To verify this quaternary solid solubility,

key alloys 1 to 8 were prepared and annealed as shown in Table 4.16. Key alloy 1 was annealed for 21 days at 900°C. This alloy was subjected to additional 11 days annealing compared to the other alloys because equilibrium was not reached after first 10 days. A three-phase equilibrium among α -Fe, $Ce_{1.1}Fe_4B_4$ and a quaternary solid solution of Si in $Ce_2Fe_{14}B$ was observed. Quaternary solubility extension of $Ce_2Fe_{14}B$ is 2 at.% Si. Figure 4.22(a) shows a BSE micrograph of key alloy 1. After key alloys 2 to 4 were annealed at 900°C for 10 days, α -Fe and a quaternary solid solution of Si in $Ce_2Fe_{14}B$ were observed. Measured contents of Si in the $Ce_2Fe_{14}B$ compound for key alloys 2 to 4 are 4 at.%, 7 at.% and 10 at.%, respectively. Figure 4.22(b) shows a BSE micrograph of key alloy 3. In key alloy 5, a three-phase equilibrium was observed after annealing at 900°C for 10 days. The present phases are CeFeSi, a ternary solid solution of Si in Ce_2Fe_{17} and a quaternary solid solution of Si in $Ce_2Fe_{14}B$. Concentrations of Si in Ce_2Fe_{17} and $Ce_2Fe_{14}B$ compounds are measured as 15 at.% and 13 at.%, respectively. Figure 4.22(c) shows a BSE micrograph of key alloy 5. Key alloys 6 and 7 were prepared to determine the maximum solubility limit of the $Ce_2(Fe, Si)_{14}B$ solid solution. The same four-phase equilibrium, among $CeFe_2Si_2$, a ternary solid solution of Si in Ce_2Fe_{17} , a quaternary solid solutions of Si in $Ce_2Fe_{14}B$ and $(Fe_{1-x-y}Si_xCe_y)_3B$ phase, was observed in key alloys 6 and 7. Also, the same quaternary solubility extensions of $Ce_2Fe_{14}B$ and $(Fe_{1-x}Si_x)_3B$ phases were measured in alloys 6 and 7 as 13 at.% Si and 7 at.% of Ce, respectively. In key alloy 8, a four-phase equilibrium, among CeFeSi, a ternary solid solution of Si in Ce_2Fe_{17} , a quaternary solid solutions of $Ce_2Fe_{14}B$ and a quaternary solid solutions of $Fe_{23}B_6$, was observed. Quaternary solubility extensions of $Ce_2Fe_{14}B$ is measured as 14 at.% Si. Figure 4.22(d-e) show BSE micrographs of alloys 6 and 8, respectively. Table 4.17 lists the key alloys with their phase-compositions obtained by WDS analysis.

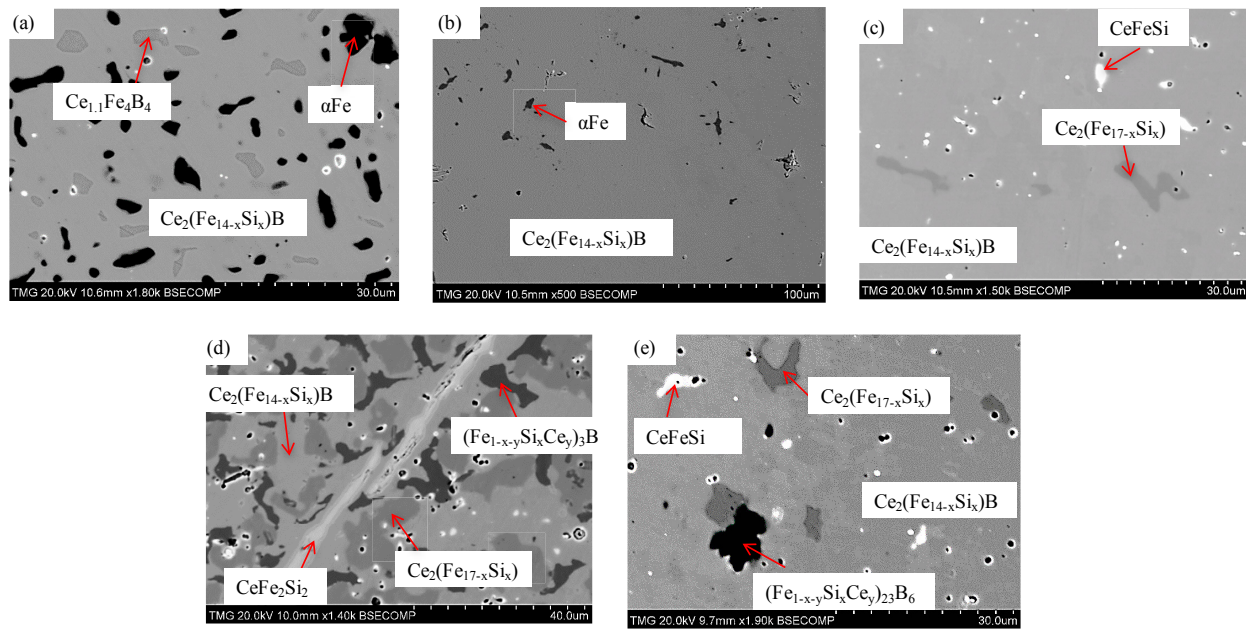


Figure 4.22: BSE micrographs of key alloys (a) 1, (b) 3, (c) 5, (d) 6, (e) 8

Table 4.17: Chemical analysis and the corresponding phases of the key alloys in Ce-Fe-Si-B

Key alloy number	Actual global composition (at.%)				Phase composition (at.%)				Corresponding phase
	Ce	Fe	Si	B	Ce	Fe	Si	B	
1	12	81	1	6	12	80	2	6	$\text{Ce}_2(\text{Fe}_{14-x}\text{Si}_x)\text{B}$ ($0 \leq x \leq 2.33$)
					12	44	0	44	$\text{Ce}_{1.1}\text{Fe}_4\text{B}_4$
					1	99	0	0	$\alpha\text{-Fe}$
2	13	79	3	5	12	78	4	6	$\text{Ce}_2(\text{Fe}_{14-x}\text{Si}_x)\text{B}$ ($0 \leq x \leq 2.33$)
					1	98	1	0	$\alpha\text{-Fe}$
3	13	76	6	5	12	75	7	6	$\text{Ce}_2(\text{Fe}_{14-x}\text{Si}_x)\text{B}$ ($0 \leq x \leq 2.33$)
					1	98	1	0	$\alpha\text{-Fe}$
4	13	73	9	5	12	72	10	6	$\text{Ce}_2(\text{Fe}_{14-x}\text{Si}_x)\text{B}$ ($0 \leq x \leq 2.33$)
					3	94	3	0	$\alpha\text{-Fe}$
5	13	70	12	5	12	69	13	6	$\text{Ce}_2(\text{Fe}_{14-x}\text{Si}_x)\text{B}$ ($0 \leq x \leq 2.33$)
					33	34	33	0	CeFeSi
					11	74	15	0	$\text{Ce}_2(\text{Fe}_{17-x}\text{Si}_x)$ ($0 \leq x \leq 3$)
6	12	68	14	6	12	69	13	6	$\text{Ce}_2(\text{Fe}_{14-x}\text{Si}_x)\text{B}$ ($0 \leq x \leq 2.33$)
					7	60	8	25	$(\text{Fe}_{1-x-y}\text{Si}_x\text{Ce}_y)_3\text{B}$ ($x = 0.107, y = 0.093$)
					20	40	40	0	CeFe_2Si_2
					11	74	15	0	$\text{Ce}_2(\text{Fe}_{17-x}\text{Si}_x)$ ($0 \leq x \leq 3$)
7	13	67	15	5	12	69	13	6	$\text{Ce}_2(\text{Fe}_{14-x}\text{Si}_x)\text{B}$ ($0 \leq x \leq 2.33$)
					7	60	8	25	$(\text{Fe}_{1-x-y}\text{Si}_x\text{Ce}_y)_3\text{B}$ ($x = 0.107, y = 0.093$)
					20	40	40	0	CeFe_2Si_2
					11	74	15	0	$\text{Ce}_2(\text{Fe}_{17-x}\text{Si}_x)$ ($0 \leq x \leq 3$)
8	14	66	15	5	12	68	14	6	$\text{Ce}_2(\text{Fe}_{14-x}\text{Si}_x)\text{B}$ ($0 \leq x \leq 2.33$)
					7	63	8	22	$(\text{Fe}_{1-x-y}\text{Si}_x\text{Ce}_y)_{23}\text{B}_6$ ($x = 0.099, y = 0.087$)
					34	33	33	0	CeFe_2Si_2
					11	74	15	0	$\text{Ce}_2(\text{Fe}_{17-x}\text{Si}_x)$ ($0 \leq x \leq 3$)

4.2.2.2 XRD analyses of Ce-Fe-Si-B key alloys

After identifying the phases and the corresponding compositions in all the key alloys using SEM/WDS, XRD analyses were performed to verify the detected phases. Si was used as an internal calibration standard to correct the zero shift and specimen surface displacement. The $\text{Ce}_2(\text{Fe}_{14-x}\text{Si}_x)\text{B}$ solid solution with 0-14 at.% Si homogeneity range was detected in key alloys 1 to 8. XRD analysis has shown that, $\text{Ce}_2(\text{Fe}_{14-x}\text{Si}_x)\text{B}$ solid solution crystallizes in a tetragonal structure with $\text{P4}_2/\text{mm}$ and $\text{Nd}_2\text{Fe}_{14}\text{B}$ prototype. The peak positions shift to higher angle with decreasing Fe content. The substitution of Fe by Si, which has a smaller atomic radius, decreases the unit cell parameters in $\text{Ce}_2\text{Fe}_{14}\text{B}$. This is confirmed by the increase of the 2θ values of the peak positions as the Si concentration increases. Example of XRD patterns of the $\text{Ce}_2(\text{Fe}_{14-x}\text{Si}_x)\text{B}$ solid solution are shown in Figure 4.23(a-b), corresponding to key alloys 2 and 5. The $\text{Ce}_2(\text{Fe}_{17-x}\text{Si}_x)$ solid solution observed in key alloys 5 to 8 has rhombohedral $\text{Th}_2\text{Zn}_{17}$ structure with R-3m space group. In key alloy 5, CeFeSi crystallizes in tetragonal structure with $\text{P4}/\text{mmm}$ space group and PbClF prototype. The $(\text{Fe}_{1-x-y}\text{Si}_x\text{Ce}_y)_3\text{B}$ and CeFe_2Si_2 phases are observed in key alloys 6 to 7. $(\text{Fe}_{1-x-y}\text{Si}_x\text{Ce}_y)_3\text{B}$ phase has cementite (Fe_3C) structure-type with Pnma space group while CeFe_2Si_2 has CeAl_2Ga_2 structure-type with space group of $\text{I4}/\text{mmm}$. Example of the XRD pattern of $(\text{Fe}_{1-x-y}\text{Si}_x\text{Ce}_y)_3\text{B}$ is shown in Figure 4.23(c), which corresponds to key alloy 7. $(\text{Fe}_{1-x-y}\text{Si}_x\text{Ce}_y)_2\text{B}_6$, which is observed in key alloy 8, crystallizes in face-centered cubic structure with Fm-3m space group and Cr_{23}C_6 prototype. In general, these results are in accord with those obtained by diffusion couples but more discussion will be provided in section 4.2.5.

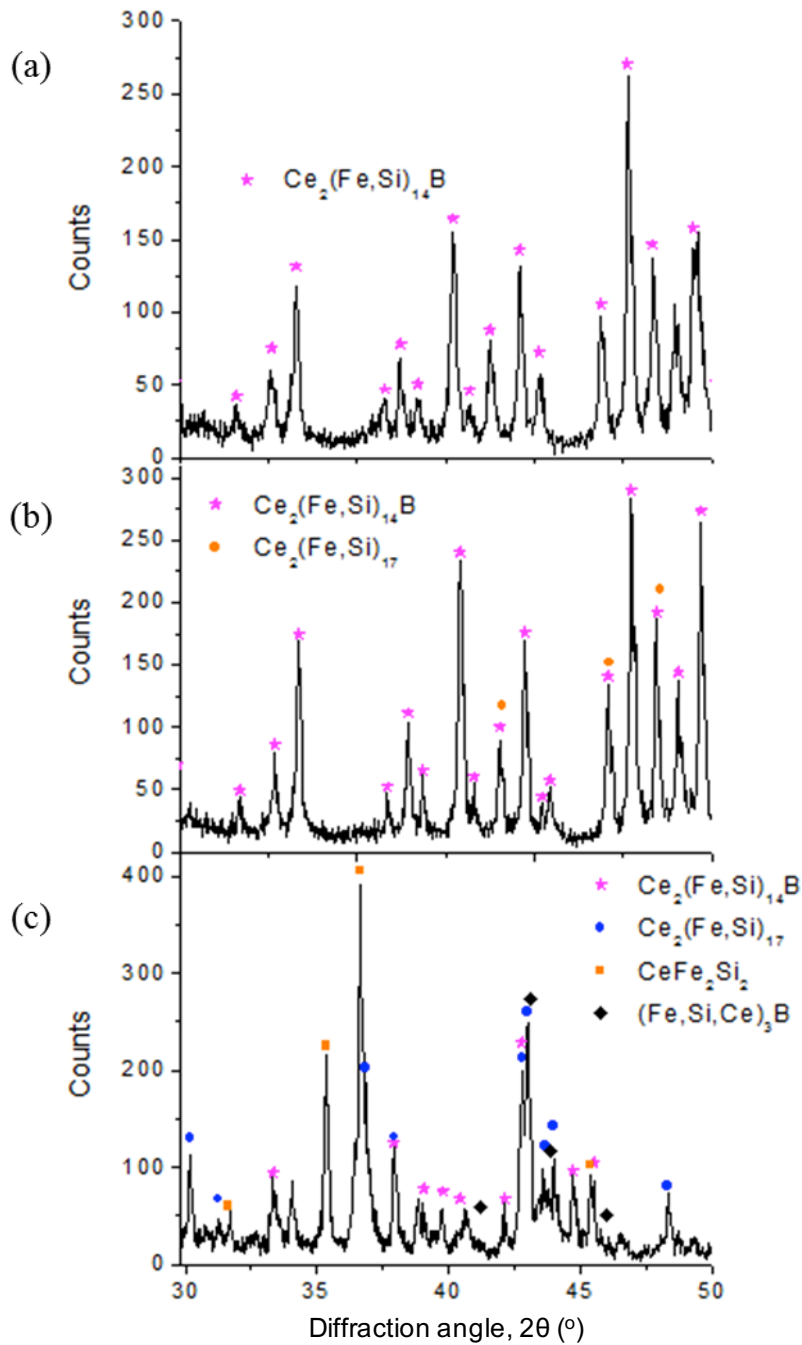


Figure 4.23: XRD pattern of key alloys (a) 2, (b) 5, (c) 7

4.2.3 MFM characterization of phases in the Fe region of the Ce-Fe-Si-B system

To identify the magnetic phases in the Fe region of the Ce-Fe-Si-B system, MFM was used to screen out non-magnetic phases from the observed phases present in this region. Under MFM

test, it is known that a magnetic phase produces contrast of domains while a non-magnetic phase has no magnetic domains. The parameters, (scan size for example) used for obtaining MFM micrographs during MFM tests are the same for all the key alloys. From the results of diffusion couples and key alloys prepared to investigate the Fe region of the Ce-Fe-Si-B system, three quaternary phases were observed. These are $(\text{Fe, Si, Ce})_3\text{B}$, $\text{Ce}_2(\text{Fe, Si})_{14}\text{B}$ and $(\text{Fe, Si, Ce})_{23}\text{B}_6$. MFM analysis was performed on each phase and only $\text{Ce}_2(\text{Fe}_{14-x}\text{Si}_x)\text{B}$ ($0 \leq x \leq 2.33$) solid solution shows visible contrast of magnetic domains. Figure 4.24 shows the compositions of the key alloys and Table 4.18 shows the compositions and annealing conditions of the key alloys used for the MFM analysis of the magnetic $\text{Ce}_2(\text{Fe}_{14-x}\text{Si}_x)\text{B}$ ($0 \leq x \leq 2.33$) solid solution. Figure 4.25 shows examples of MFM micrographs in the $\text{Ce}_2(\text{Fe}_{14-x}\text{Si}_x)\text{B}$ ($0 \leq x \leq 2.33$) solid solution range at different Si contents.

Table 4.18: Compositions of key alloys used in MFM characterization of the $\text{Ce}_2(\text{Fe, Si})_{14}\text{B}$ solid solution annealed at 900°C for at least 10 days

Key alloy number	Actual composition (at.%)			
	Ce	Fe	Si	B
1	12	81	1	6
2	13	79	3	5
3	13	76	6	5
4	13	73	9	5
5	13	70	12	5

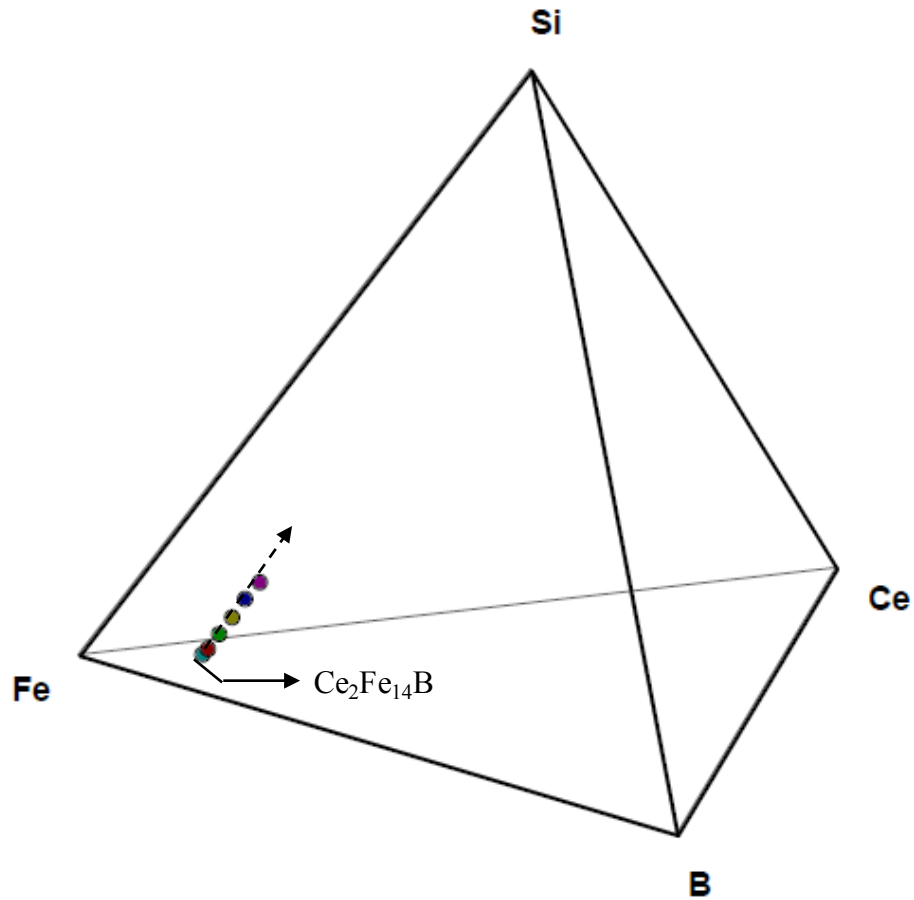


Figure 4.24: Compositions of the selected key alloys used for MFM characterization of the $\text{Ce}_2(\text{Fe}_{14-x}\text{Si}_x)\text{B}$ solid solution. The arrow represents increasing Si direction

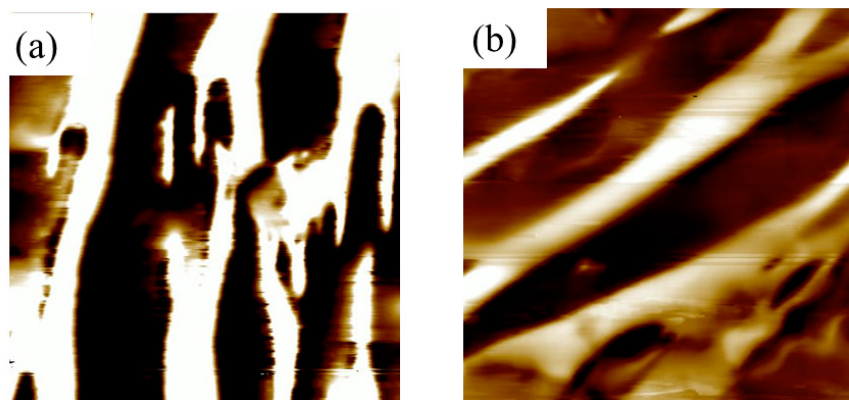


Figure 4.25: MFM magnetic domain micrographs of key alloys (a) 3, (b) 5. Scan size of each micrograph is $30\ \mu\text{m}$

4.2.4 Intrinsic magnetic properties of the $\text{Ce}_2\text{Fe}_{14}\text{B}$ compound modified by Si

Six key alloys have been used to study the effect of Si substitution on the intrinsic magnetic properties of $\text{Ce}_2\text{Fe}_{14}\text{B}$. The percentage volumes of $\text{Ce}_2\text{Fe}_{14}\text{B}$ dissolving different amounts of Si in key alloys are all greater than 60 %, except key alloy 1 which has 56 %. Despite that the content of the $\text{Ce}_2(\text{Fe}_{14-x}\text{Si}_x)\text{B}$ solid solution in the key alloy 6 is more than 70 %, it contains traces of three other phases. The saturation magnetizations (M_S) were obtained in external magnetic fields of up to 50 kOe at 298 K. The anisotropy fields (H_A) were determined, using second derivative of magnetization (d^2M/dH^2), by singular point detection (SPD) method. After measuring magnetic properties of key alloys 1 to 6, comparison was made with the magnetic properties of reference alloy (0) in Table 4.19. This was carried out in order to uncover how the Si affects magnetic properties of $\text{Ce}_2\text{Fe}_{14}\text{B}$ compound. Table 4.19 shows the actual global compositions and intrinsic magnetic properties of alloys prepared within the homogeneity range of $\text{Ce}_2(\text{Fe}_{14-x}\text{Si}_x)\text{B}$ solid solution. Figures 4.26 to 4.28 show the respective plots of the composition dependences of saturation magnetizations, anisotropy fields and Curie temperature in $\text{Ce}_2(\text{Fe}_{14-x}\text{Si}_x)\text{B}$ solid solution. These results will be discussed in the next section.

Table 4.19: Magnetic properties of the $\text{Ce}_2(\text{Fe}_{14-x}\text{Si}_x)\text{B}$ solid solution

Key alloy number	Si addition (at.%)	M_S (emu/g) at 298 K	H_A (kOe) at 298 K	T_C ($^{\circ}\text{C}$)
0	0	130.0	28.1	151
1	1	123.1	26.1	163
2	3	116.1	26.1	183
3	7	110.4	22.1	200
4	10	104.2	13.7	219
5	13	93.0	9.1	243
6	15	88.8	6.8	252

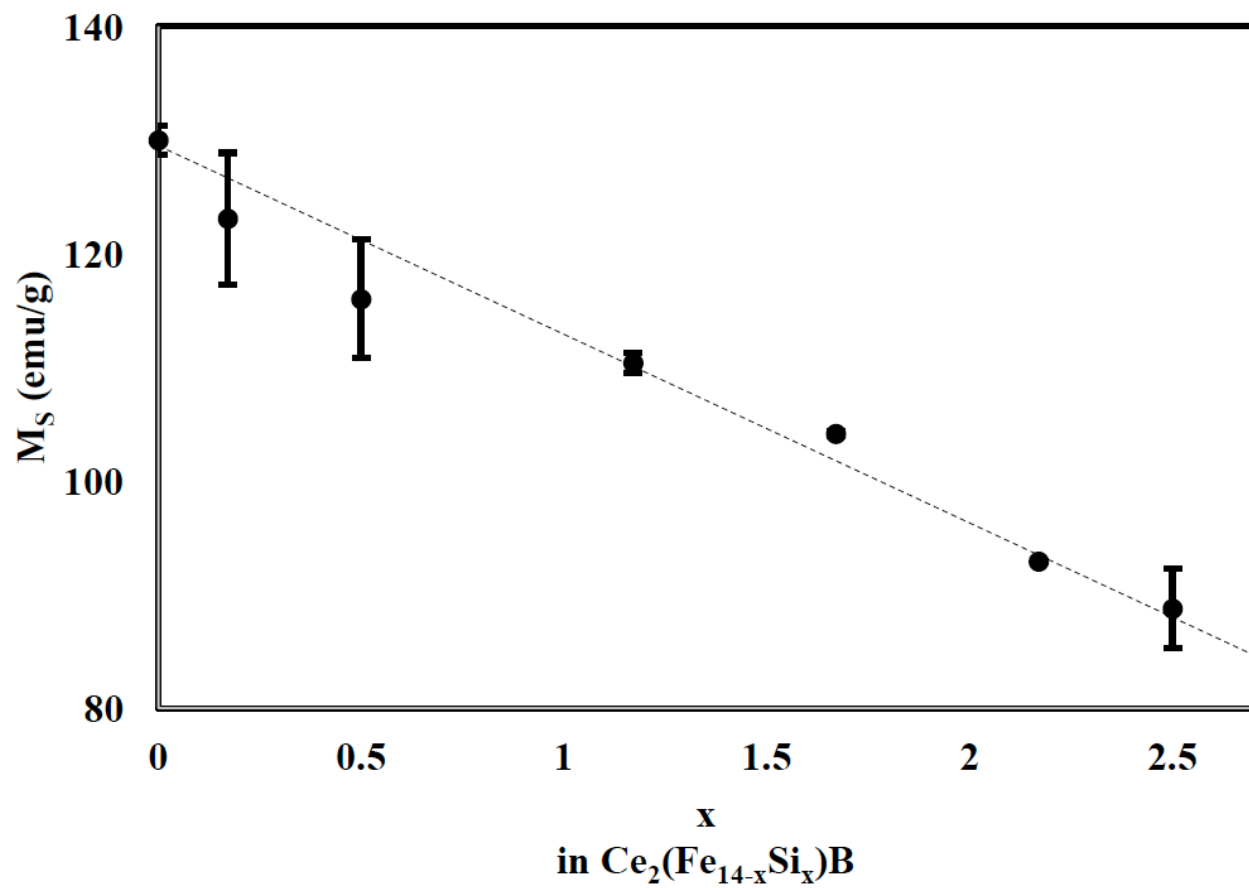


Figure 4.26: The composition dependence of the saturation magnetization (M_S) of the $Ce_2(Fe_{14-x}Si_x)B$ solid solution at 298 K

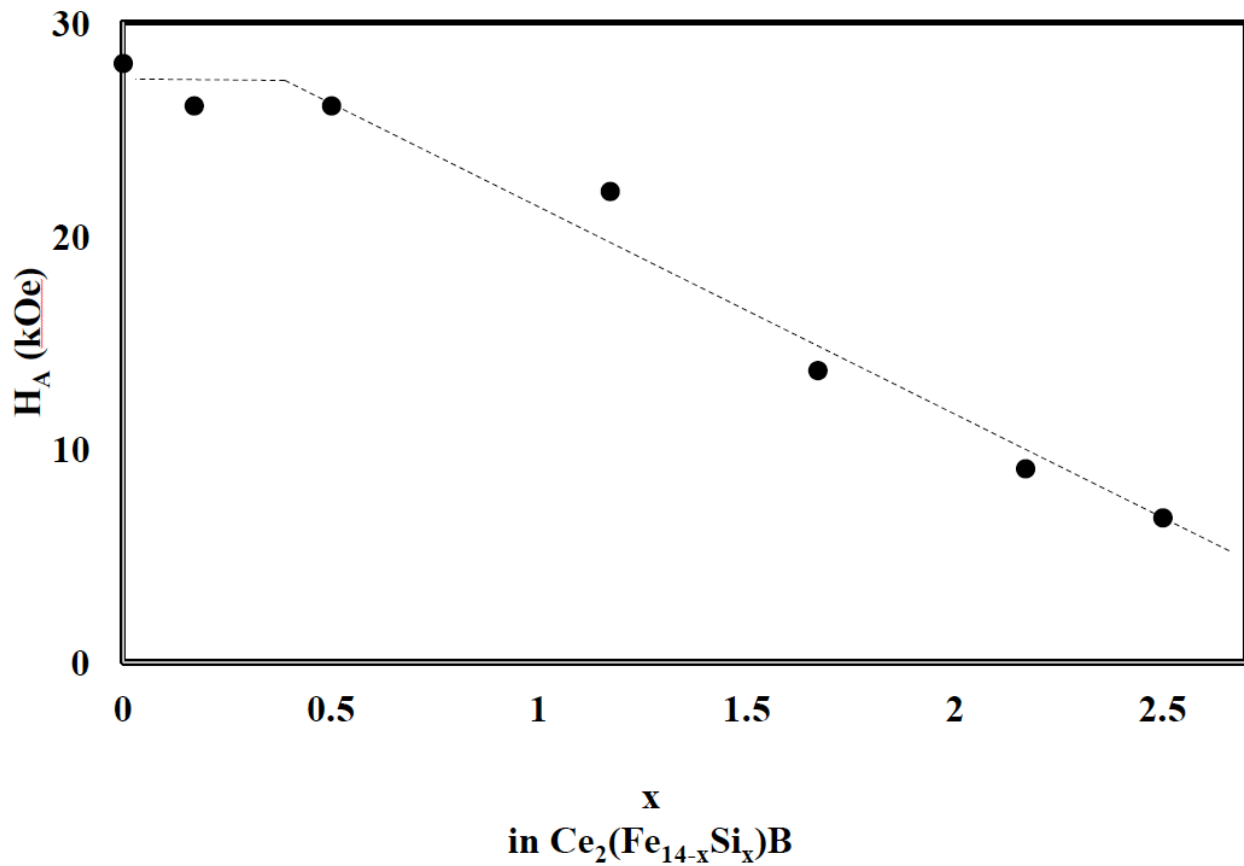


Figure 4.27: The composition dependence of the anisotropy field (H_A) for the $\text{Ce}_2(\text{Fe}_{14-x}\text{Si}_x)\text{B}$ solid solution at 298 K

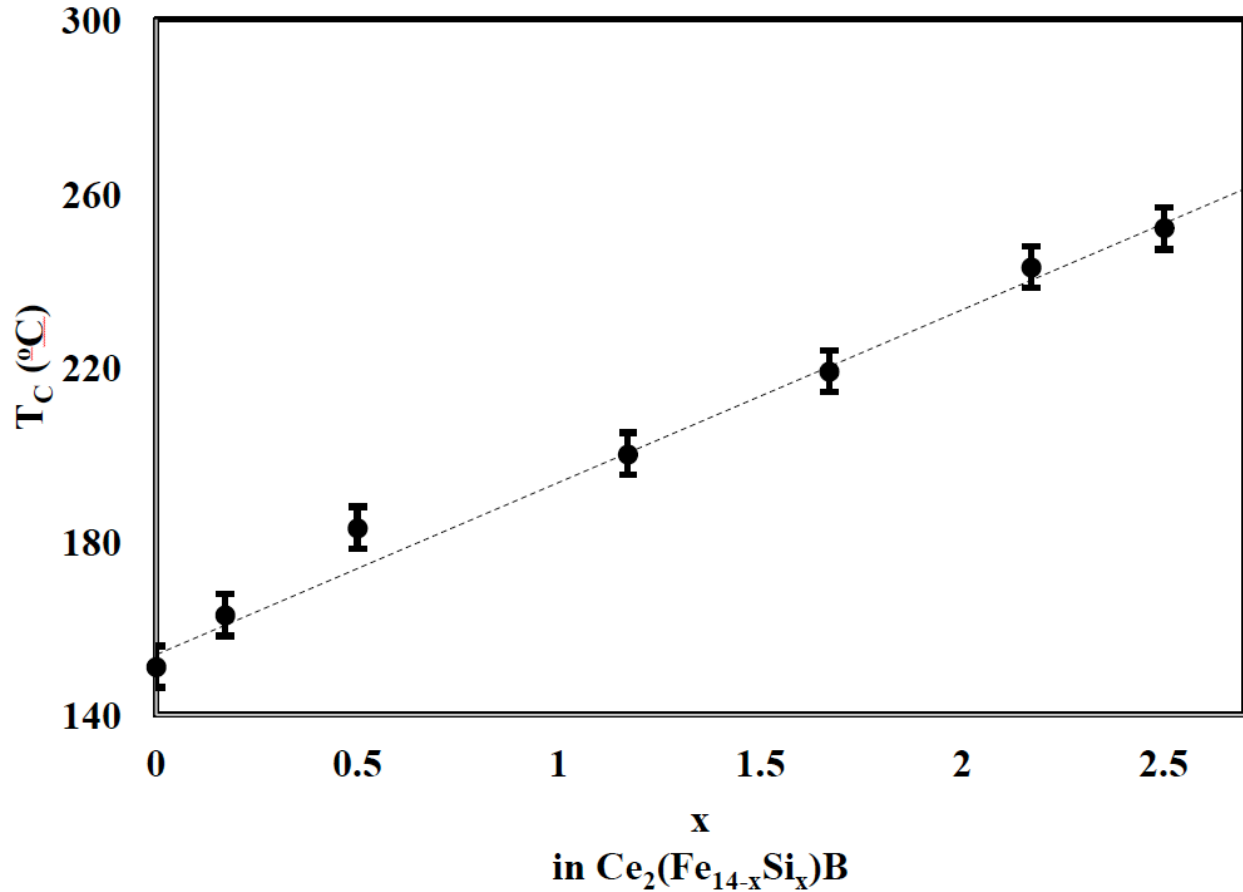


Figure 4.28: The composition dependence of the Curie temperature (T_C) for the $Ce_2(Fe_{14-x}Si_x)B$ solid solution

4.2.5 Discussion of the results of the Ce-Fe-Si-B quaternary system

Fe region of Ce-Fe-Si-B system has been successful investigated with 3 diffusion couples and 8 key alloys annealed at 900°C. Quaternary extension of $Ce_2Fe_{14}B$ compound was observed in diffusion couple and key alloys were prepared to verify and further investigate the quaternary solid solubility of Si in $Ce_2Fe_{14}B$.

In diffusion couples, homogeneity range of Si measured in $Ce_2Fe_{14}B$ compound is between 0 and 12 at.% Si. To verify these results, key alloys 1 to 8 were prepared and annealed at 900°C for 10 days, except key alloy 1 that was annealed for 21 days. Results of key alloys confirm the

occurrence of the $\text{Ce}_2(\text{Fe}_{14-x}\text{Si}_x)\text{B}$ solid solution and the homogeneity range of Si in $\text{Ce}_2\text{Fe}_{14}\text{B}$ compound was measured between 0 and 14 at.% Si. The corresponding formula of Si concentration in this solid solution is $\text{Ce}_2(\text{Fe}_{14-x}\text{Si}_x)\text{B}$ ($0 \leq x \leq 2.33$). XRD analysis confirmed the solid solubility of Si in this solid solution and it also shows that this solid solution crystallizes in tetragonal structure with $\text{P4}_2/\text{mm}$ space group and $\text{Nd}_2\text{Fe}_{14}\text{B}$ prototype.

Fe_3B extends into the Ce-Fe-Si-B quaternary system through Si substitution. The $(\text{Fe}_{1-x-y}\text{Si}_x\text{Ce}_y)_3\text{B}$ ($x = 0.107, y = 0.093$) phase is observed in key alloys 6 to 8. Detailed analysis of this solid solution is not pursued in this study, because it has no potential for PM material. Concentrations of 7 at.% Ce and 8 at.% Si were measured in the $(\text{Fe}_{1-x-y}\text{Si}_x\text{Ce}_y)_3\text{B}$ ($x = 0.107, y = 0.093$) phase. XRD analysis confirms the Si substitution and shows that it has cementite (Fe_3C) structure-type with Pnma space group.

Quaternary solubility of Ce and Si in the Fe_{23}B_6 compound was observed in key alloy 8. Contents of Ce and Si measured in this compound are 7 and 8 at.%, respectively. XRD study shows that the $(\text{Fe}_{1-x-y}\text{Si}_x\text{Ce}_y)_{23}\text{B}_6$ crystallizes in face-centered cubic structure with Fm-3m space group and Cr_{23}C_6 prototype. The corresponding formula of this compound is written as $(\text{Fe}_{1-x-y}\text{Si}_x\text{Ce}_y)_{23}\text{B}_6$, where $x = 0.099$ and $y = 0.087$.

The $\text{Ce}_2(\text{Fe}_{14-x}\text{Si}_x)\text{B}$, $(\text{Fe}_{1-x-y}\text{Si}_x\text{Ce}_y)_3\text{B}$ and $(\text{Fe}_{1-x-y}\text{Si}_x\text{Ce}_y)_{23}\text{B}_6$ phases were analyzed using MFM. Only $\text{Ce}_2(\text{Fe}_{14-x}\text{Si}_x)\text{B}$ solid solution shows visible contrast of magnetic domains at different Si concentrations. Quantitative determination of the intrinsic magnetic properties of the $\text{Ce}_2(\text{Fe}_{14-x}\text{Si}_x)\text{B}$ ($0 \leq x \leq 2.33$) solid solution was carried out after MFM analysis has revealed it to be magnetic. Different studies have been carried out on the effect of Si on magnetic properties of $\text{RE}_2\text{Fe}_{14}\text{B}$ compounds, except $\text{Ce}_2\text{Fe}_{14}\text{B}$, in the literature [15-16, 104-106]. Seven key alloys were selected in order to study the effect of Si substitution on the magnetic properties of

$\text{Ce}_2\text{Fe}_{14}\text{B}$ compound. The selected alloys cover the homogeneity range of the $\text{Ce}_2(\text{Fe}, \text{Si})_{14}\text{B}$ solid solution. The trend of Figure 4.26 shows that saturation magnetization (M_S) decreases as the concentration of Si substituting Fe in $\text{Ce}_2\text{Fe}_{14}\text{B}$ compound increases. The saturation magnetizations decrease by about 2 emu/g for each 1 at.% substitution of Fe by Si. This behaviour is in agreement with the studies on $\text{RE}_2\text{Fe}_{14}\text{B}$ series, other than $\text{Ce}_2\text{Fe}_{14}\text{B}$, reported in the literature [15-16, 104]. As shown in Figure 4.27, in general, anisotropy field decreases as the concentration of Si in $\text{Ce}_2\text{Fe}_{14}\text{B}$ compound increases. However between $x = 0.17$ (1 at.% Si) and $x = 0.5$ (3 at.% Si), increasing the Si concentration maintains anisotropy field value of about 26 kOe. Beyond $x = 0.5$ (3 at.% Si), increasing Si concentration in the $\text{Ce}_2\text{Fe}_{14}\text{B}$ compound decreases anisotropy field rapidly. The trend of the plot of anisotropy field of the $\text{Ce}_2(\text{Fe}_{14-x}\text{Si}_x)\text{B}$ ($0 \leq x \leq 2.33$) solid solution at 298 K studied in this work does not seem to be similar to that of the $\text{Nd}_2(\text{Fe}_{14-x}\text{Si}_x)\text{B}$ solid solution at 295 K reported by Jurczyk et al. [16]. In $\text{Nd}_2(\text{Fe}_{14-x}\text{Si}_x)\text{B}$ solid solutions, the maximum anisotropy field is observed at $x = 0.5$ (3 at.% Si). While no maximum is observed for the $\text{Ce}_2(\text{Fe}_{14-x}\text{Si}_x)\text{B}$ solid solution, the same value of anisotropy field is obtained at $x = 0.17$ and 0.5 (1 at.% Si and 3 at.% Si). The effect of Si on the Curie temperature of $\text{RE}_2\text{Fe}_{14}\text{B}$ compounds, except $\text{Ce}_2\text{Fe}_{14}\text{B}$, has been investigated in the literature [15–16, 106]. It was found that, increasing Si in $\text{RE}_2\text{Fe}_{14}\text{B}$ compounds increases the Curie temperature. As shown in Figure 4.28, increasing Si substitution for Fe in the $\text{Ce}_2\text{Fe}_{14}\text{B}$ compound increases the Curie temperature almost linearly. The Curie temperature increases, in the mean, by about 6.7°C per 1 at.% Si. From the practical perspective, the increase in Curie temperature from 151°C to 252°C by Si substitution may indicate the suitability of this solid solution, with an intermediate Si content (that is, in the range $0 \leq \text{Si} \leq 14$), for some PM applications despite the decrease in M_S and H_A .

4.3 Ce-Fe-Al-B system

Key alloy technique has been used to experimentally investigate the quaternary extension of the $\text{Ce}_2\text{Fe}_{14}\text{B}$ compound in the Ce-Fe-Al-B system. Based on the experience from the results of the $\text{Ce}_2(\text{Fe}, \text{Ni})_{14}\text{B}$ and $\text{Ce}_2(\text{Fe}, \text{Si})_{14}\text{B}$ solid solutions, key alloys containing various levels of Fe/Al substitution in the $\text{Ce}_2(\text{Fe}, \text{Al})_{14}\text{B}$ solid solution were prepared. In this section, results of SEM/WDS, XRD and MFM will be first explained in details and discussions of the results will follow in a separate sub-section.

4.3.1 Phase analysis

9 key alloys were used to investigate the quaternary extension of the $\text{Ce}_2\text{Fe}_{14}\text{B}$ compound in the Ce-Fe-Al-B system. Table 4.20 lists the compositions and annealing conditions of these 9 key alloys. Figure 4.29 shows the compositions of the key alloys used in studying the Ce-Fe-Al-B system.

Table 4.20: Compositions of key alloys used in studying the Ce-Fe-Al-B system annealed at 900°C for 10 days

Key alloy number	Actual composition (at.%)			
	Ce	Fe	Al	B
1	12	81	1	6
2	12	79	3	6
3	12	78	4	6
4	12	76	6	6
5	12	73	9	6
6	12	70	12	6
7	12	64	18	6
8	12	66	16	6
9	12	68	14	6

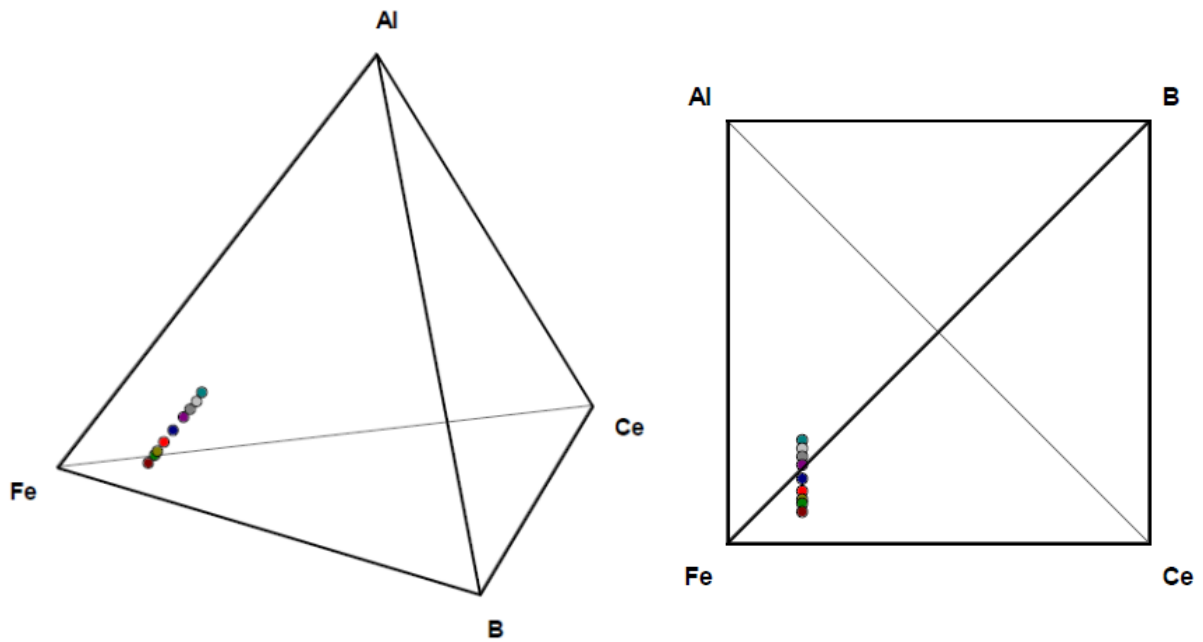


Figure 4.29: : The compositions of the key alloys in the Ce-Fe-Al-B system

The same three-phase equilibrium, among α -Fe, $\text{Ce}_{1.1}\text{Fe}_4\text{B}_4$ and a quaternary solid solution of Al in $\text{Ce}_2\text{Fe}_{14}\text{B}$, was observed in key alloys 1 to 6 after annealing at 900°C for 10 days. Quaternary solubility extensions of $\text{Ce}_2\text{Fe}_{14}\text{B}$ measured in alloys 1 to 6 are 2 at.%, 3 at.%, 5 at.%, 7 at.%, 9 at.% and 12 at.%, respectively. Figure 4.30(a) shows the microstructure observed in alloy 1, which is a typical microstructure observed in these six alloys. Key alloys 7 to 9 contain the same four-phase equilibrium. These phases are α -Fe, $\text{Ce}_{1.1}\text{Fe}_4\text{B}_4$, a ternary solid solution of Al in $\text{Ce}_2\text{Fe}_{17}$ and a quaternary solid solution of Al in $\text{Ce}_2\text{Fe}_{14}\text{B}$. Quaternary solubility extensions of the $\text{Ce}_2\text{Fe}_{14}\text{B}$ compound in alloys 7 to 9 are measured as 14 at.%, 15 at.% and 15 at.%, respectively. Figure 4.30(b) shows the microstructure of key alloy 8 which is a typical microstructure observed in the alloys 7 to 9. Table 4.21 summarizes the chemical analysis and compositions of phases observed in the Al containing Ce-Fe-B key alloys.

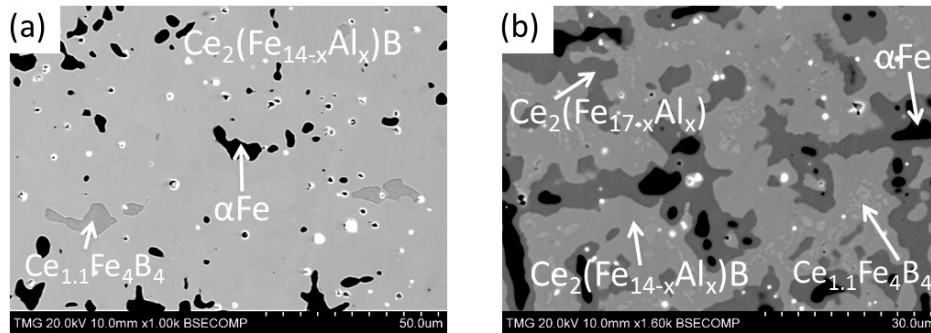


Figure 4.30: BSE micrographs of key alloys (a) 1 (b) 8

Table 4.21: Chemical analysis and the corresponding phases in key alloys 1 to 9

Key alloy number	Actual global composition (at.%)				Phase composition (at.%)				Corresponding phase
	Ce	Fe	Al	B	Ce	Fe	Al	B	
1	12	81	1	6	12	80	2	6	$Ce_2(Fe_{14-x}Al_x)B$ ($0 \leq x \leq 2.5$)
					1	98	1	0	α -Fe
					12	44	0	44	$Ce_{1.1}Fe_4B_4$
2	12	79	3	6	12	79	3	6	$Ce_2(Fe_{14-x}Al_x)B$ ($0 \leq x \leq 2.5$)
					1	96	3	0	α -Fe
					12	44	0	44	$Ce_{1.1}Fe_4B_4$
3	12	78	4	6	12	77	5	6	$Ce_2(Fe_{14-x}Al_x)B$ ($0 \leq x \leq 2.5$)
					1	95	4	0	α -Fe
					12	44	0	44	$Ce_{1.1}Fe_4B_4$
4	12	76	6	6	12	75	7	6	$Ce_2(Fe_{14-x}Al_x)B$ ($0 \leq x \leq 2.5$)
					1	93	6	0	α -Fe
					12	44	0	44	$Ce_{1.1}Fe_4B_4$
5	12	73	9	6	12	73	9	6	$Ce_2(Fe_{14-x}Al_x)B$ ($0 \leq x \leq 2.5$)
					1	91	8	0	α -Fe
					12	44	0	44	$Ce_{1.1}Fe_4B_4$
6	12	70	12	6	12	70	12	6	$Ce_2(Fe_{14-x}Al_x)B$ ($0 \leq x \leq 2.5$)
					1	87	12	0	α -Fe
					12	44	0	44	$Ce_{1.1}Fe_4B_4$
7	12	64	18	6	12	68	14	6	$Ce_2(Fe_{14-x}Al_x)B$ ($0 \leq x \leq 2.5$)
					1	86	13	0	α -Fe
					12	44	0	44	$Ce_{1.1}Fe_4B_4$
					11	68	21	0	$Ce_2(Fe_{17-x}Al_x)$ ($0 \leq x \leq 11.35$)
8	12	66	16	6	12	67	15	6	$Ce_2(Fe_{14-x}Al_x)B$ ($0 \leq x \leq 2.5$)
					2	84	14	0	α -Fe
					12	44	0	44	$Ce_{1.1}Fe_4B_4$
					11	67	22	0	$Ce_2(Fe_{17-x}Al_x)$ ($0 \leq x \leq 11.35$)
9	12	68	14	6	12	67	15	6	$Ce_2(Fe_{14-x}Al_x)B$ ($0 \leq x \leq 2.5$)
					1	84	15	0	α -Fe
					12	44	0	44	$Ce_{1.1}Fe_4B_4$
					11	66	23	0	$Ce_2(Fe_{17-x}Al_x)$ ($0 \leq x \leq 11.35$)

4.3.2 XRD analyses of the Ce-Fe-Al-B key alloys

XRD analyses were performed to identify the phases present in the nine key alloys used in investigating the Ce-Fe-Al-B system. Si was used as an internal calibration standard to correct the zero shift and specimen surface displacement. The $\text{Ce}_2(\text{Fe}_{14-x}\text{Al}_x)\text{B}$ solid solution was observed in key alloys 1 to 9. XRD analysis has shown that the $\text{Ce}_2(\text{Fe}_{14-x}\text{Al}_x)\text{B}$ solid solution crystallizes in a tetragonal structure with $\text{P4}_2/\text{mnm}$ and $\text{Nd}_2\text{Fe}_{14}\text{B}$ prototype. The peak positions shift to lower angle with decreasing Fe content. The substitution of Fe by Al, which has a smaller atomic radius, increases the unit cell parameters in the $\text{Ce}_2\text{Fe}_{14}\text{B}$. This is confirmed by the decrease of the 2θ values of the peak positions as the Al concentration increases. Example of XRD patterns of the $\text{Ce}_2(\text{Fe}_{14-x}\text{Al}_x)\text{B}$ solid solution is shown in Figure 4.31(a-b) which corresponds to key alloys 2 and 5. The $\text{Ce}_{1.1}\text{Fe}_4\text{B}_4$ compound was observed in key alloys 1 to 9. $\text{Ce}_{1.1}\text{Fe}_4\text{B}_4$ crystallizes in tetragonal structure with $\text{P4}_2/\text{n}$ space group and NdCo_4B_4 prototype. The $\text{Ce}_2(\text{Fe}_{17-x}\text{Al}_x)$ solid solution which was observed in key alloys 7 to 9 has $\text{Zn}_{17}\text{Th}_2$ prototype and R-3m space group. . In general, these results are consistent with the SEM/WDS analysis above-discussed but more discussion will be provided in section 4.3.5.

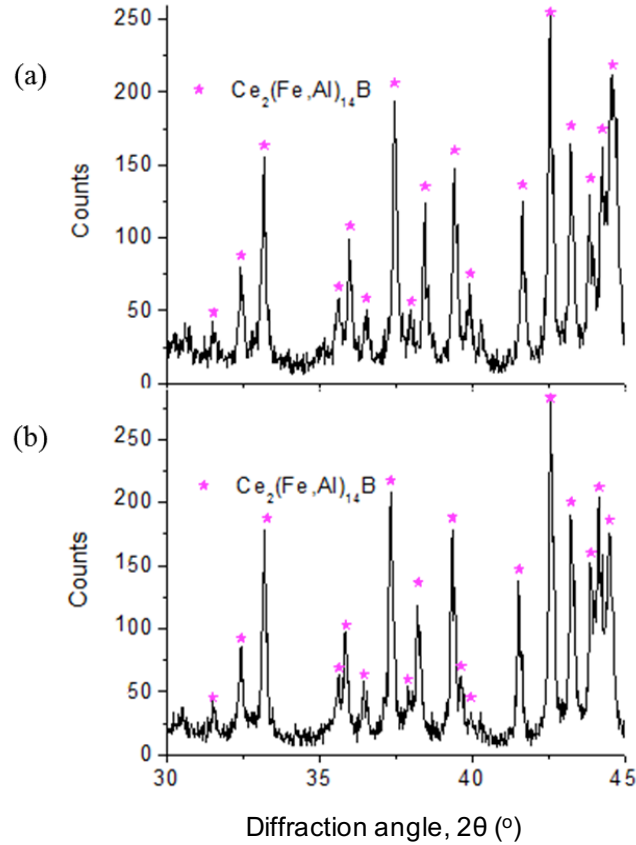


Figure 4.31: XRD pattern of key alloys (a) 2, (b) 5

4.3.3 MFM characterization in the Fe region of the Ce-Fe-Al-B system

8 key alloys were selected to study the $Ce_2(Fe, Al)_{14}B$ solid solution with the aid of MFM. Selection of the compositions of the key alloys was to cover the homogeneity range of Al in the $Ce_2(Fe_{14-x}Al_x)B$ ($0 \leq x \leq 2.50$) solid solution. The parameters, (scan size for example) used for obtaining MFM micrographs during MFM tests are the same for all the key alloys in Table 4.20. Figure 4.32 shows magnetic domain structures of alloys 2, 3 and 5.

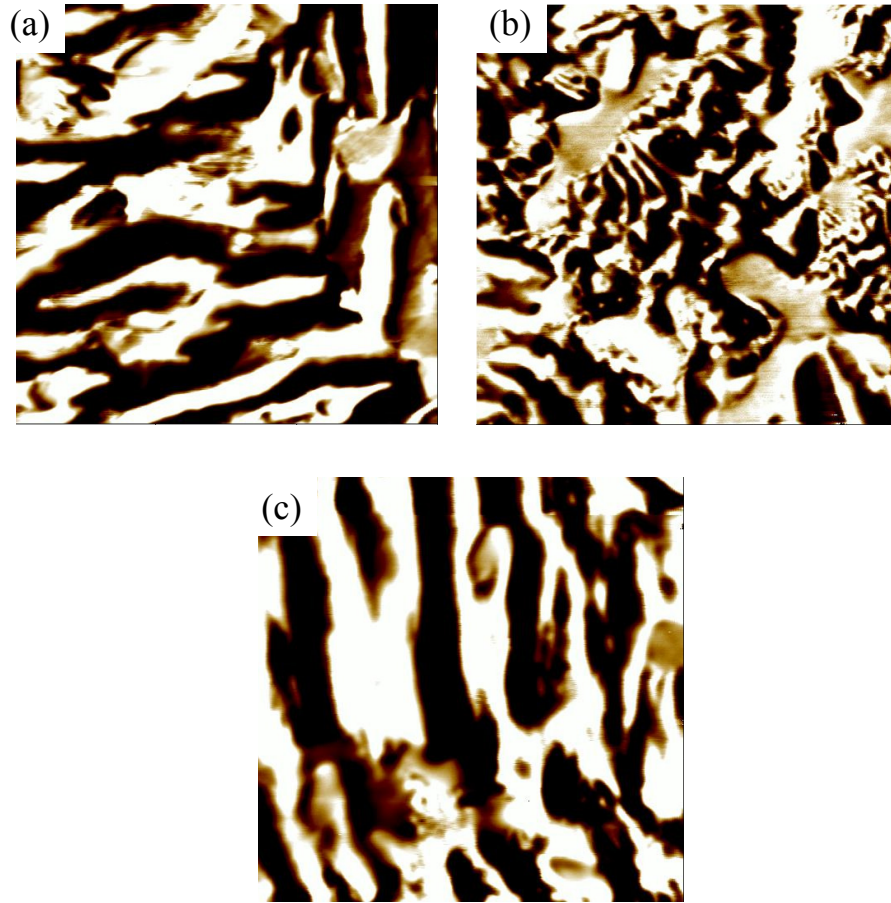


Figure 4.32: MFM domain micrographs of key alloys (a) 2, (b) 3, (c) 5. Scan size of each micrograph is 30 μm

4.3.4 Intrinsic magnetic properties of the $\text{Ce}_2\text{Fe}_{14}\text{B}$ compound doped with Al

Six key alloys have been used to investigate the effect of Al addition on the intrinsic magnetic properties of $\text{Ce}_2\text{Fe}_{14}\text{B}$. The percentage volumes of the quaternary solid solution of Al in $\text{Ce}_2\text{Fe}_{14}\text{B}$ in key alloys are all greater than 70 %, except for key alloy 6 which has 64 %. The saturation magnetizations (M_S) were obtained in external magnetic fields of up to 50 kOe at 298 K. The anisotropy fields (H_A) were determined, using second derivative of magnetization (d^2M/dH^2), by singular point detection (SPD) method. In order to investigate the effect of Al addition on the magnetic properties of the $\text{Ce}_2\text{Fe}_{14}\text{B}$ compound, comparison was performed

between magnetic properties of Ce₂Fe₁₄B reference alloy (0) and the selected key alloys 1 to 6. Table 4.22 shows intrinsic magnetic properties of alloys prepared along the homogeneity range of the Ce₂(Fe_{14-x}Al_x)B (0 ≤ x ≤ 2.50) solid solution. Figures 4.33 to 4.35 show the respective plots of the composition dependences of saturation magnetizations, anisotropy fields and Curie temperature on Al content in Ce₂(Fe_{14-x}Al_x)B solid solution.

Table 4.22: Magnetic properties of Ce₂(Fe_{14-x}Al_x)B solid solution

Key alloy number	Al addition (at.%)	M _S (emu/g) at 298 K	H _A (kOe) at 298 K	T _C (°C)
0	0	130.0	28.1	151
1	2	* -	27.2	146
2	4	123.6	22.1	139
3	6	86.0	16.1	117
4	9	82.3	10.1	90
5	12	56.8	3.1	46
6	17	36.1	**-	72

*The measurement was not acceptable due to large error. **The test for anisotropy field was stopped in key alloy 5 because the value is too low for PM materials.

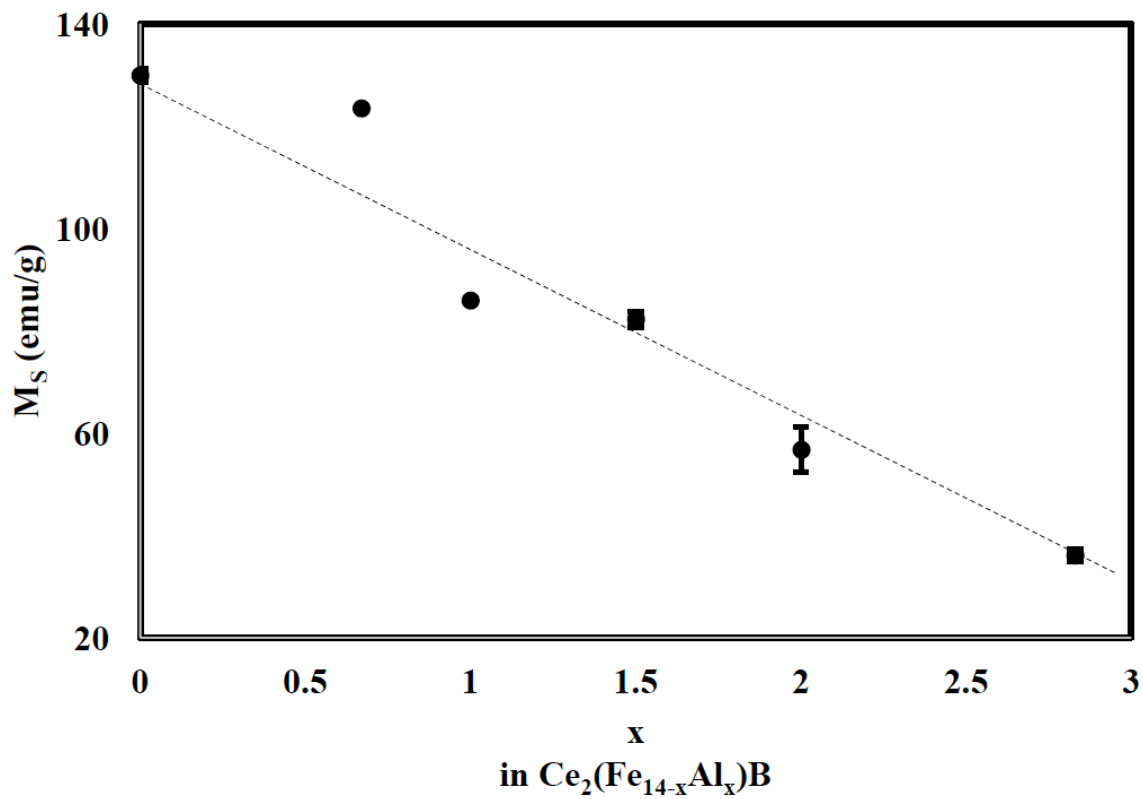


Figure 4.33: The composition dependence of the saturation magnetization (M_S) of the $\text{Ce}_2(\text{Fe}_{14-x}\text{Al}_x)\text{B}$ solid solution at 298 K

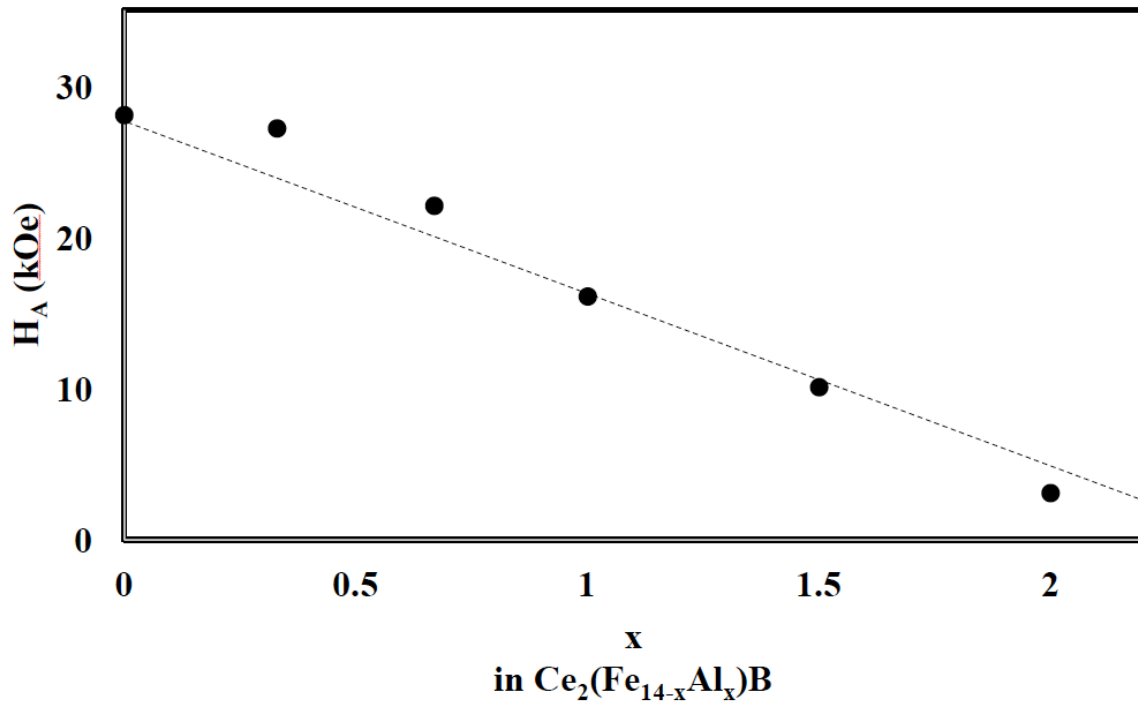


Figure 4.34: The composition dependence of the anisotropy field (H_A) of the $\text{Ce}_2(\text{Fe}, \text{Al})_{14}\text{B}$ solid solution at 298 K

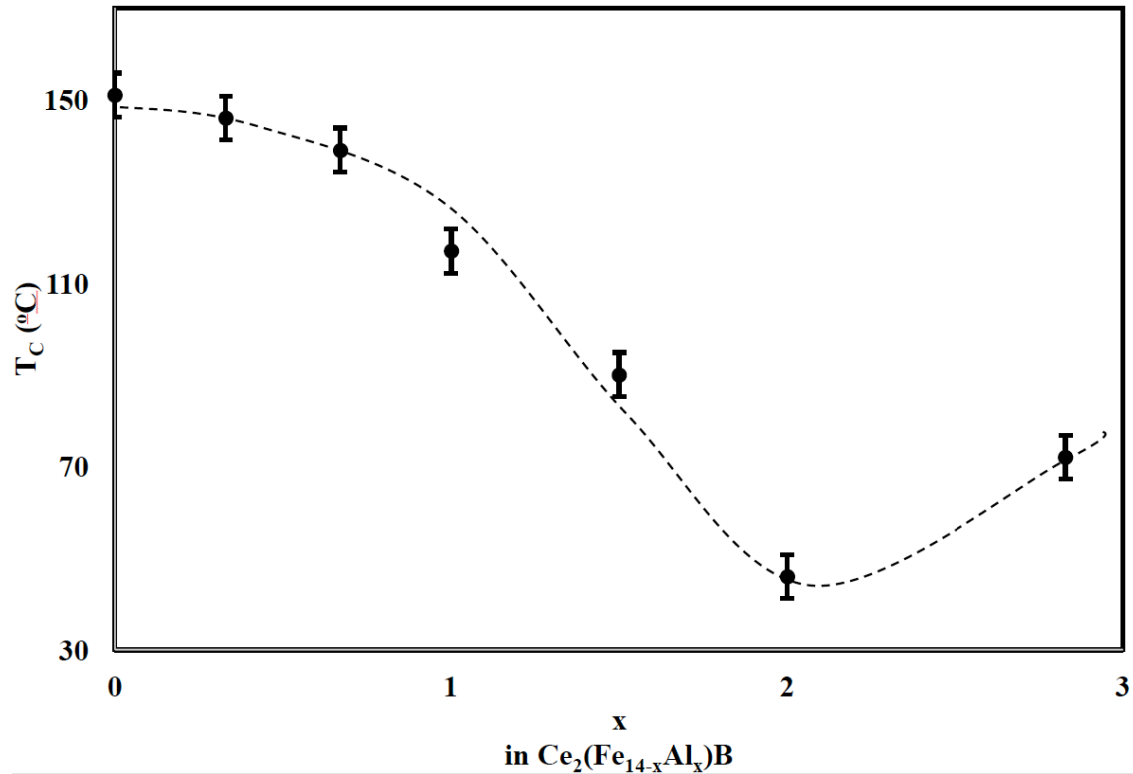


Figure 4.35: The composition dependence of the Curie temperature (T_C) of the $\text{Ce}_2(\text{Fe, Al})_{14}\text{B}$ solid solution

4.3.5 Discussion of the results of the Ce-Fe-Al-B system

9 key alloys have been used to investigate quaternary extension of the $\text{Ce}_2\text{Fe}_{14}\text{B}$ compound in the Ce-Fe-Al-B system at 900°C . Homogeneity range of Al in $\text{Ce}_2(\text{Fe}_{14-x}\text{Al}_x)\text{B}$ solid solution is between 0 and 15 at.% Al. The corresponding formula of this solid solution solid solution is $\text{Ce}_2(\text{Fe}_{14-x}\text{Al}_x)\text{B}$ ($0 \leq x \leq 2.5$). XRD analysis confirmed the solid solubility of Al in this solid solution observed in the key alloys by SEM/WDS. It also shows that this solid solution crystallizes in a tetragonal structure with $P4_2/mnm$ space group and $\text{Nd}_2\text{Fe}_{14}\text{B}$ prototype.

MFM analysis of the $\text{Ce}_2(\text{Fe}_{14-x}\text{Al}_x)\text{B}$ solid solution shows visible contrast of magnetic domains in the MFM micrographs in Figure 4.32. After MFM analysis, further analyses were performed to determine the intrinsic magnetic properties of the $\text{Ce}_2(\text{Fe}_{14-x}\text{Al}_x)\text{B}$ solid solution at various Al

concentrations. Various studies have been carried out to determine the effect of Al on the magnetic properties of $\text{RE}_2\text{Fe}_{14}\text{B}$ compounds, other than $\text{Ce}_2\text{Fe}_{14}\text{B}$, in the literature [13, 17, 105-106]. And to study the effect of Al solubility in the $\text{Ce}_2\text{Fe}_{14}\text{B}$ compound on its magnetic properties, key alloys 1 to 6 were selected. The compositions of the selected alloys cover the homogeneity range of $\text{Ce}_2(\text{Fe}_{14-x}\text{Al}_x)\text{B}$ ($0 \leq x \leq 2.5$) solid solution. In Figure 4.33, it is illustrated that saturation magnetization decreases with increasing Al concentration. This behaviour is in agreement with the studies reported in the literatures for the $\text{RE}_2(\text{Fe, Al})_{14}\text{B}$, other than $\text{Ce}_2\text{Fe}_{14}\text{B}$ [17, 106]. As shown in Figure 4.34, anisotropy field decreases with increasing Al substitution of Fe in $\text{Ce}_2\text{Fe}_{14}\text{B}$. Unlike the result of Jurczyk [20] on the magnetic behaviour of $\text{Nd}_2\text{Fe}_{12-x}\text{Al}_x\text{Co}_2\text{B}$ which shows that a maximum anisotropy field of 85 kOe is observed at $x = 0.10$ and 0.30 (0.6 at.% Al and 1.8 at.% Al), no maximum value of anisotropy field is observed in $\text{Ce}_2(\text{Fe}_{14-x}\text{Al}_x)\text{B}$ solid solution. As shown in Figure 4.35, addition of Al to the $\text{Ce}_2\text{Fe}_{14}\text{B}$ compound reduces Curie temperature. This is in agreement with the previous studies on the effect of Al on the other $\text{RE}_2\text{Fe}_{14}\text{B}$ discussed in the literature [14, 17, 106]. Beyond $x = 2$ (12 at.% Al in the $\text{Ce}_2\text{Fe}_{14}\text{B}$ compound), an unusual increase in Curie temperature is observed. Comparing with the un-doped $\text{Ce}_2\text{Fe}_{14}\text{B}$ reference compound, the addition of Al which reduces the three intrinsic magnetic properties of the above-discussed $\text{Ce}_2(\text{Fe}_{14-x}\text{Al}_x)\text{B}$ solid solution makes its elemental addition alone not to be promising for PM applications. Perhaps, the interaction of Al with other additives such as Ni and/or Si will show different response. This will be attempted in the future.

Chapter 5

Conclusions, contributions and recommendations for future works

5.0 Conclusions

With the aid of the solid-solid diffusion couple and key alloy techniques, experimental investigations in the Fe-rich regions of the Ce-Fe-Ni-B, Ce-Fe-Si-B and Ce-Fe-Al-B quaternary systems have been performed. Phase equilibria in the studied regions were fully determined. No new quaternary compound was detected, but it was identified that compounds such as: CeNi₄B dissolves Fe, Fe₂₃B₆ dissolves Ni and Ce, Fe₃B dissolves Si and Ce, and Ce₂Fe₁₄B dissolves Ni, Si and Al. Homogeneity ranges of quaternary solid solutions of Ce₂Fe₁₄B in the Ce-Fe-{Ni, Si, Al}-B systems were determined as $0 \leq \text{Ni} \leq 9$, $0 \leq \text{Si} \leq 14$ and $0 \leq \text{Al} \leq 15$, in at.%.

High-throughput method has been used to identify magnetic phases in the Fe-rich regions of the Ce-Fe-{Ni, Si, Al}-B systems. This method allows investigating phase equilibria in the Fe-rich regions of the Ce-Fe-{Ni, Si, Al}-B systems, using diffusion couple and key alloy techniques. MFM analyses were used to screen out non-magnetic phases from all the identified phases in these regions. Intrinsic magnetic properties of the magnetic phases were determined, using TGA and PPMS.

MFM tests showed that only Ce₂Fe₁₄B quaternary extension demonstrates potential for PM material among the detected phases in the Fe-rich regions of the Ce-Fe-{Ni, Si, Al}-B quaternary systems. The influences of Ni, Si and Al additives on the intrinsic magnetic properties of Ce₂Fe₁₄B compound were studied. It was discovered that, increasing the concentrations of Ni, Si and Al dissolving in Ce₂Fe₁₄B compound reduce saturation magnetization and anisotropy field. The anisotropy field of Ce₂Fe₁₄B compound, which was reported as 26.4 kOe by Grossinger et

al. [94–95], was determined to be 28.1 kOe in this work. Ni and Si additions to $\text{Ce}_2\text{Fe}_{14}\text{B}$ compound increase Curie temperature, while Al reduces it. Highest value of 210°C Curie temperature for $x = 1.5$ (9 at.% Ni) is observed for the $\text{Ce}_2\text{Fe}_{14}\text{B}$ containing Ni while highest value of 252°C for $x = 2.5$ (15 at.% Si) is found for the $\text{Ce}_2\text{Fe}_{14}\text{B}$ containing Si. The lowest value of 46°C for $x = 2$ (12 at.% Al) is found for the $\text{Ce}_2\text{Fe}_{14}\text{B}$ containing Al. From the practical perspective, the highest Curie temperature of 252°C observed at $x = 2.5$ in $\text{Ce}_2(\text{Fe}, \text{Si})_{14}\text{B}$ solid solution makes it to be promising for the PM materials, comparing with 151°C Curie temperature of the un-doped $\text{Ce}_2\text{Fe}_{14}\text{B}$ reference compound. But in reality, this might not be the case since the saturation magnetization and anisotropy field decrease with increasing Ni and Si contents. Therefore, an intermediate composition with a compromised Curie temperature but with optimum saturation magnetization and anisotropy field might be the most promising Ce-Fe-B containing Ni or Si magnets.

Study of the Fe-Ni side of the Ce-Fe-Ni ternary systems showed that, CeNi_3 and Ce_2Ni_7 compounds extend into the ternary system through dissolving Fe. It is confirmed that the ternary solid solutions of Fe in CeNi_3 , Ce_2Ni_7 and CeNi_5 compounds extend to at least 41 at.% Fe, 16 at.% Fe and 19 at.% Fe, at 700°C and to at least 43 at.% Fe, 25 at.% Fe and 24 at.% Fe at 900°C , respectively.

5.1 Contributions

There are no reports on the phase equilibria and magnetic properties of the phases in the Fe-rich regions of the Ce-Fe-{Ni, Si, Al}-B quaternary systems in the literature, hence all the contributions of this work were performed for the first time. In this work, the magnetic phases in the Fe-rich regions in the Ce-Fe-{Ni, Si, Al}-B systems have been identified using high-

throughput screening method. These phases are the quaternary solid solutions of Ni, Si and Al in $\text{Ce}_2\text{Fe}_{14}\text{B}$. Additional contributions of this work are:

- ✓ Phase equilibria in the Fe-rich of the Ce-Fe-{Ni, Si, Al}-B quaternary systems were established at 900°C based on the results of diffusion couples and key alloys. The solubilities of Ni, Si and Al in $\text{Ce}_2\text{Fe}_{14}\text{B}$ were determined using WDS and XRD analysis.
- ✓ Micrographs showing the magnetic domain structures of the $\text{Ce}_2(\text{Fe}_{14-x}\text{T}_x)\text{B}$ solid solutions, where T denotes Ni, Si and Al, were obtained using MFM
- ✓ The intrinsic magnetic properties of the $\text{Ce}_2(\text{Fe}_{14-x}\text{T}_x)\text{B}$ solid solutions, where T denotes Ni, Si and Al, were determined. Increasing solubilities of Ni and Si in the $\text{Ce}_2\text{Fe}_{14}\text{B}$ were found to reduce saturation magnetization and anisotropy field, but increase Curie temperature. Solubility of Al in the $\text{Ce}_2\text{Fe}_{14}\text{B}$ reduces saturation magnetization, anisotropy field and Curie temperature.
- ✓ The Fe-Ni side of Ce-Fe-Ni ternary system was investigated in this work. There were reports only on the ternary solid solution of Fe in CeNi_5 and unlimited solid solution between CeFe_2 and CeNi_2 in the literature. Extended solid solution of Fe in CeNi_3 and Ce_2Ni_7 were observed at 700°C and 900°C for the first time in this work.

5.2 Recommendations for future work

Phase equilibria in the Fe-rich regions of Ce-Fe-{Ni, Si, Al}-B quaternary systems have been experimentally determined in this work, studying other regions of these quaternary systems is recommended.

Other recommendations are:

- Influences of the simultaneous addition of Ni, Si and/or Al on the $\text{Ce}_2\text{Fe}_{14}\text{B}$ compound are suggested for the future work;

- Studying the extrinsic magnetic properties of $\text{Ce}_2(\text{Fe}_{14-x}\text{T}_x)\text{B}$ solid solutions, where T denotes Ni, Si and Al;
- Studying the effect of fabrication process, that is melt spinning and casting, on these magnetic properties;
- Determining the phase equilibria in the Ce-Fe-Ni ternary system for the whole composition ranges;
- The use of the thermodynamic modelling coupled with the current experimental results is recommended to construct a self-consistent database for the Ce-Fe-{Ni, Si, Al}-B systems.

Reference

- [1] P. C. Dent: Rare earth elements and permanent magnets (invited). *J. Appl. Phys.*, Vol. 111, No. 7, 2012, pp. 07A721.
- [2] M. J. Kramer, R. W. McCallum, I. A. Anderson, and S. Constantinides: Prospects for non-rare earth permanent magnets for traction motors and generators. *JOM*, Vol. 64, No. 7, 2012, pp. 752–763.
- [3] Tech Alert: Automotive Applications for Magnetic Materials. Magnetic Division, Canada. Available online: www.mmgca.com
- [4] S.-F. Cheng: The materials substitution in rare earth permanent magnets. PhD thesis, North Carolina State University at Raleigh, USA, 1984.
- [5] K. J. Strnat: Modern permanent magnets for applications in electro-technology. *Proc. IEEE*, Vol. 78, No. 6, 1990, pp. 923–946.
- [6] K. S. V. L. Narasimhan: Iron-based rare earth magnets. *J. Appl. Phys.*, Vol. 57, No. 1, 1985, pp. 4081–4085.
- [7] M. Sagawa, S. Fujimura, N. Togawa, H. Yamamoto, and Y. Matsuura: New material for permanent magnets on a base of Nd and Fe (invited). *J. Appl. Phys.*, Vol. 55, No. 6, 1984, pp. 2083–2087.
- [8] J. J. Croat, J. F. Herbst, R. W. Lee, and F. E. Pinkerton: High-energy product Nd-Fe-B permanent magnets. *Appl. Phys. Lett.*, Vol. 44, No. 1, 1984, pp. 148–149.
- [9] C. Jonsson: The magnets of the green cars: Motors. Earth, European Rare Network, Recycling Network, 2014. Available online: erean.eu
- [10] General Motors: Chevrolet showcases spark EV electric motor. GM corporate newsroom, 2011. Available online: www.media.gm.com

- [11] D. Goll and H. Kronmüller: High-performance permanent magnets. *Naturwissenschaften*, Vol. 87, 2000, pp. 423–438.
- [12] W. E. Wallace: Rare earth-transition metal permanent magnet materials. *Prog. Solid St. Chem.*, Vol. 16, 1985, pp. 127–162.
- [13] S. Pandian, V. Chandrasekaran, G. Markandeyulu, K. J. L. Iyer, and K. V. S. Rama Rao: Effect of Al, Cu, Ga, Nb additions on the magnetic properties and microstructural features of sintered NdFeB. *J. Appl. Phys.*, Vol. 92, No. 10, 2002, pp. 6082–6086.
- [14] M. Jurczyk: On the magnetic behaviour of $\text{Nd}_2\text{Fe}_{12-x}\text{T}_x\text{Co}_2\text{B}$ compounds ($T = \text{Al}, \text{V}, \text{Cr}$). *IEEE Trans. Magn.*, Vol. 24, No. 2, 1988, pp. 1942–1944.
- [15] E. Burzo, N. Plugaru, V. Pop, L. Stanciu, and W. E. Wallace: Bulk magnetic properties of the $\text{Y}_2\text{T}_x\text{Fe}_{14-x}\text{B}$ compounds, where $T = \text{Al}, \text{Ni}, \text{or Co}$. *Solid State Commun.*, Vol. 58, No. 11, 1986, pp. 803–805.
- [16] M. Jurczyk, A. Kowalczyk, and A. Wrzeciono: Magnetic properties of $\text{Nd}_2\text{Fe}_{14-x}\text{Si}_x\text{B}$ compounds. *Phys. Status Solidi*, Vol. 101, 1987, pp. K65.
- [17] M. Jurczyk and A. Kowalczyk: Effect of silicon additions on the magnetic properties of $\text{Nd}_2\text{Fe}_{12}\text{Co}_2\text{B}$ alloy. *J. Magn. Magn. Mater.*, Vol. 68, 1987, pp. 331–334.
- [18] A. T. Pedziwiatr, W. E. Wallace, E. Burzo, and V. Pop: Magnetic properties of $\text{Y}_2\text{Fe}_{14-x}\text{M}_x\text{B}$ compounds where $M = \text{Si or Cu}$. *Solid State Commun.*, Vol. 61, No. 1, 1987, pp. 61–64.
- [19] E. J. Skoug, M. S. Meyer, F. E. Pinkerton, M. M. Tessema, D. Haddad, and J. F. Herbst: Crystal structure and magnetic properties of $\text{Ce}_2\text{Fe}_{14-x}\text{Co}_x\text{B}$ alloys. *J. Alloys Compd.*, Vol. 574, 2013, pp. 552–555.
- [20] M. Q. Huang, E. B. Boltich, W. E. Wallace, and E. Oswald: Magnetic characteristics of

- $R_2Fe_{14-x}Mn_xB$ systems ($R = Y, Nd, Pr$ and Gd). *J. Less-Common Met.*, Vol. 124, 1986, pp. 55–60.
- [21] S. Constantinides: The magnetic material challenge. ARPA-E Workshop, 2010. Available online: www.arpa-e.energy.gov
- [22] M. Humphries: Rare earth elements: The global supply chain. CRS Report for Congress, 2013.
- [23] C. Zhou, F. E. Pinkerton, and J. F. Herbst: High curie temperature of Ce–Fe–Si compounds with $ThMn_{12}$ structure. *Scr. Mater.*, vol. 95, 2015, pp. 66–69, 2015.
- [24] Rare earth metals: MineralPrices.com. Available online: mineralprices.com
- [25] R. Marazza, P. Riani, and G. Cacciamani: Critical assessment of iron binary systems with light rare earths La, Ce, Pr, and Nd. *Inorganica Chim. Acta*, Vol. 361, No. 14–15, 2008, pp. 3800–3806.
- [26] L. Paolasini, P. Dervenagas, P. Vulliet, J. P. Sanchez, G. H. Lander, A. Hiess, A. Panchula, and P. C. Canfield: Magnetic response function of the itinerant ferromagnet $CeFe_2$. *Phys. Rev. B*, Vol. 58, No. 18, 1998, pp. 12117–12124.
- [27] Y. Janssen, S. Chang, A. Kreyssig, A. Kracher, Y. Mozharivskyj, S. Misra, and P. C. Canfield: Magnetic phase diagram of Ce_2Fe_{17} . *Phys. Rev. B*, Vol. 76, No. 5, 2007, pp. 054420.
- [28] W. Iwasieczko, A. G. Kuchin, L. Folcik, and H. Drulis: Effect of pressure and Mn substitution on magnetic ordering of $Ce_2Fe_{17-x}Mn_x$ ($x = 0, 1$). *J. Alloys Compd.*, Vol. 406, 2005, pp. 155–159.
- [29] H. Okamoto: Ce-Fe (cerium-iron). *J. Phase Equilibria Diffus.*, Vol. 29, No. 1, 2008, pp. 116–117.

- [30] T. Van Rompaey, K. C. Hari Kumar, and P. Wollants: Thermodynamic optimization of the B-Fe system. *J. Alloys Compd.*, Vol. 334, 2002, pp. 173–181.
- [31] O. Kubaschewski: *Iron binary phase diagrams*. Springer, 1982.
- [32] V. Raghavan: B-Fe-Si (boron-iron-silicon). *J. Phase Equilibria Diffus.*, Vol. 28, No. 4, 2007, pp. 380–381.
- [33] E. C. Passamani, J. R. B. Tagarro, C. Larica, and A. A. R. Fernandes: Thermal studies and magnetic properties of mechanical alloyed Fe₂B. *J. Physics-Condensed Matter*, Vol. 14, No. 8, 2002, pp. 1975–1983.
- [34] G. V. Raynor and V. G. Rivlin: *Phase equilibria in iron ternary alloys (A critical assessment of the experimental literature)*. The Institute of Metals, 1988.
- [35] V. Raghavan: Phase diagram updates and evaluations of the Al-Fe-P, B-Fe-U, Bi-Fe-Zn, Cu-Fe-Zn, Fe-Si-Zn and Fe-Ti-V systems. *J. Phase Equilibria Diffus.*, Vol. 34, No. 3, 2013, pp. 230–243.
- [36] V. Raghavan: Al-Fe-Zn (aluminum-iron-zinc). *J. Phase Equilibria Diffus.*, Vol. 32, No. 2, 2011, pp. 143–144.
- [37] V. Raghavan: Al-Fe-Si (aluminum-iron-silicon). *J. Phase Equilibria Diffus.*, Vol. 23, No. 4, 2002, pp. 362–366.
- [38] R.-H. Fan, L. Qi, K.-N. Sun, G.-H. Min, and H.-Y. Gong: The bonding character and magnetic properties of Fe₃Al: Comparison between disordered and ordered alloy. *Phys. Lett. Sect. A*, Vol. 360, No. 2, 2006, pp. 371–375.
- [39] ASM International: *Alloy phase diagrams*. ASM handbook, Vol. 3, 1998.
- [40] Y. Jiraskova, J. Bursik, I. Turek, M. Hapla, A. Titov, and O. Zivotsky: Phase and magnetic studies of the high-energy alloyed Ni-Fe. *J. Alloys Compd.*, Vol. 594, 2014, pp.

133–140.

- [41] J. De Keyzer, G. Cacciamani, N. Dupin, and P. Wollants: Thermodynamic modeling and optimization of the Fe–Ni–Ti system. *Calphad*, Vol. 33, No. 1, 2009, pp. 109–123.
- [42] K. B. Reuter, D. B. Williams, and J. Goldstein: Determination of the Fe-Ni phase diagram below 400°C. *Metall. Trans. A*, Vol. 20A, 1989, pp. 719–725.
- [43] Y. Mishin, M. J. Mehl, and D. A. Papaconstantopoulos: Phase stability in the Fe–Ni system: Investigation by first-principles calculations and atomistic simulations. *Acta Mater.*, Vol. 53, No. 15, 2005, pp. 4029–4041.
- [44] L. J. Swartzendruber, V. P. Itkin, and C. B. Alcock: The Fe-Ni (iron-nickel) system. *J. Phase Equilibria*, Vol. 12, No. 3, 1991, pp. 288–312.
- [45] T. Shima, M. Okamura, S. Mitani, and K. Takanashi: Structure and magnetic properties for L1₀-ordered FeNi films prepared by alternate monatomic layer deposition. *J. Magn. Magn. Mater.*, Vol. 310, No. 2 Suppl. Part 3, 2007, pp. 2213–2214.
- [46] V. Raghavan: Ce-Fe-Si (cerium-iron-silicon). *J. Phase Equilibria Diffus.*, Vol. 29, No. 5, 2008, pp. 436–437.
- [47] V. Raghavan: Phase diagrams of ternary alloys (Monograph series on alloy phase diagram). Part 6A, NRC, 1992.
- [48] H. Vinzelberg, J. Schumann, D. Elefant, E. Arushanov, and O. G. Schmidt: Transport and magnetic properties of Fe₃Si epitaxial films. *J. Appl. Phys.*, Vol. 104, No. 9, 2008, pp. 093707.
- [49] K. Hamaya, K. Ueda, Y. Kishi, Y. Ando, T. Sadoh, and M. Miyao: Epitaxial ferromagnetic Fe₃Si/Si(111) structures with high-quality heterointerfaces. *Appl. Phys. Lett.*, Vol. 93, No. 13, 2008, pp. 132117.

- [50] R. Mantovan, M. Georgieva, M. Fanciulli, A. Goikhman, N. Barantcev, Y. Lebedinskii, and A. Zenkevich: Synthesis and characterization of Fe₃Si/SiO₂ structures for spintronics. *Phys. Status Solidi (A) Appl. Mater. Sci.*, Vol. 205, No. 8, 2008, pp. 1753–1757.
- [51] M. V Bulanova, P. N. Zheltov, K. A. Meleshevich, P. A. Saltykov, and G. Effenberg: Cerium–silicon system. *J. Alloys Compd.*, Vol. 345, 2002, pp. 110–115.
- [52] H. Okamoto: Ce-Si (cerium-silicon). *J. Phase Equilibria Diffus.*, Vol. 32, No. 5, 2011, pp. 470–471.
- [53] S. Noguchi, K. Okuda, H. Nojiri, and M. Motokawa: Magnetic properties of CeSi single crystal. *J. Magn. Magn. Mater.*, Vol. 177–181, 1998, pp. 403–404.
- [54] K. A. Gschneider Jr. and F. W. Calderwood: Al-Ce (aluminum-cerium). *Bin. Alloy Phase Diagrams*, Vol. 1, 1986, pp. 100–101.
- [55] H. Okamoto: Al-Ce (aluminum-cerium). *J. Phase Equilibria Diffus.*, Vol. 32, No. 4, 2011, pp. 392–393.
- [56] P. K. Liao, K. E. Spear, and M. E. Schlesinger: The B-Ce (boron-cerium) system. *J. Phase Equilibria*, Vol. 18, No. 3, 1997, pp. 280–283.
- [57] W. Xiong, Y. Du, X. Lu, J. C. Schuster, and H. Chen: Reassessment of the Ce-Ni binary system supported by key experiments and ab initio calculations. *Intermetallics*, Vol. 15, No. 11, 2007, pp. 1401–1408.
- [58] H. Okamoto: Ce-Ni (cerium-nickel). *J. Phase Equilibria Diffus.*, Vol. 30, No. 4, 2009, pp. 407.
- [59] K. H. J. Buschow: Magnetic properties of CeCo₃, Ce₂Co₇ and CeNi₃ and their ternary hydrides. *J. Less-Common Met.*, Vol. 72, 1980, pp. 257–263.
- [60] J. V. Chang: Magnetic properties of CeNi₃ and Ce₂Ni₇. *Trends in condensed matter*

- physics research, Nova Science Publishers, New York, 2006.
- [61] K. I. Portnoi, V. M. Romashov, V. M. Chubarov, M. K. Levinskaya, and S. E. Salibekov: Phase diagram of the system nickel-boron. *Poroshkovaya Metall.*, Vol. 50, No. 2, 1967, pp. 15–21.
- [62] J. D. Schobe and H. H. Stadelmaier: Das zweistoffsystem nickel-bor. *Zeitschrift fur Met.*, Vol. 56, No. 12, 1965, pp. 856–859.
- [63] P. K. Liao and K. E. Spear: B-Ni (boron-nickel). Phase diagrams of binary nickel alloys: Monograph series on alloy phase diagrams, ASM International, USA, 1988.
- [64] R. W. Olesinski and G. J. Abbaschian: The B-Si (boron-silicon) system. *Bull. alloy phase diagrams*, Vol. 5, No. 5, 1984, pp. 478–484.
- [65] A. I. Zaitsev and A. A. Kodentsov: Thermodynamic properties and phase equilibria in the Si-B system. *J. Phase Equilibria*, Vol. 22, No. 2, 2001, pp. 126–135.
- [66] H. Okamoto: B-Si (boron-silicon). *J. Phase Equilibria Diffus.*, Vol. 26, No. 4, 2005, pp. 396.
- [67] H. Duschaneck and P. Rogl: The Al-B (aluminium-boron) system. *J. Phase Equilibria*, Vol. 15, No. 5, 1994, pp. 543–553.
- [68] N. S. Bilonishko and Y. B. Kuz'ma: The system Ce-Fe-B. *Inorg. Mater.*, Vol. 8, No. 1, 1972, pp. 163–164.
- [69] O. M. Dub, N. F. Chaban, and Y. B. Kuz'ma: New borides of $\text{Pr}_{5-x}\text{Co}_{2+x}\text{B}_6$ -type structure containing iron and cobalt. *J. Less-Common Met.*, Vol. 117, 1986, pp. 297–302.
- [70] O. M. Dub and Y. B. Kuz'ma: Ternary borides with the $\text{Nd}_2\text{Fe}_{14}\text{B}$ structure. *Sov. Powder Metall. Met. Ceram.*, Vol. 25, No. 7, 1986, pp. 572–575.
- [71] A. Bezinge, H. F. Braun, J. Muller, and K. Yvon: Tetragonal rare earth (R) Iron borides,

- $R_{1+E}Fe_4B_4$ ($E=0.1$), with incommensurate rare earth and iron substructures. *Solid State Commun.*, Vol. 55, No. 2, 1985, pp. 131–135.
- [72] J. F. Herbst, M. S. Meyer, and F. E. Pinkerton: Magnetic hardening of $Ce_2Fe_{14}B$. *J. Appl. Phys.*, Vol. 111, No. 7, 2012, pp. 07A718.
- [73] Q. Y. Zhou, Z. Liu, S. Guo, A. R. Yan, and D. Lee: Magnetic properties and microstructure of melt-spun Ce–Fe–B magnets. *IEEE Trans. Magn.*, Vol. 51, No. 11, 2015, pp. 2104304.
- [74] K. L. Meissner: Some examples of the practical use of the clear-cross method. *Met. und erz*, Vol. 22, 1925, pp. 243–247.
- [75] O. S. Zarechnyuk, M. G. Myskin, and V. R. Ryabor: *Izv. AN SSSR. Izv. Akad. Nauk SSSR, Met.*, Vol. 2, 1969, pp. 164–166.
- [76] D. F. Franceschini and S. F. da Cunha: Magnetic properties of $Ce(Fe_{1-x}Al_x)_2$ for $x \leq 0.20$. *J. Magn. Magn. Mater.*, Vol. 51, 1985, pp. 280–290.
- [77] V. S. Zolotarevsky, N. A. Belov, and M. V. Glazoff: *Casting aluminum alloys*. Vol. 1, Elsevier, 2007.
- [78] S. R. Mishra, G. J. Long, O. A. Pringle, D. P. Middleton, Z. Hu, W. B. Yelon, F. Grandjean, and K. H. J. Buschow: A magnetic, neutron diffraction, and mossbauer spectral study of the $Ce_2Fe_{17-x}Al_x$ solid solutions. *J. Appl. Phys.*, Vol. 79, No. 6, 1996, pp. 3145–3155.
- [79] B. Grieb: *Ternary Alloys: A comprehensive compendium of evaluated constitutional data and phase diagram*. Vol. 4, 1991, pp. 59–63.
- [80] O. I. Bodak, E. I. Gladyshevskii, A. V. Kardash, and E. E. Cherkashin: The system cerium-iron-silicon. *Inorg. Mater.*, Vol. 6, No. 6, 1970, pp. 935–938.

- [81] D. Berthebaud, O. Tougait, M. Potel, and H. Noel: Isothermal section at 900°C of the Ce–Fe–Si ternary system. *J. Alloys Compd.*, Vol. 442, 2007, pp. 104–107.
- [82] Y. Zhao, J. Liang, W. Tang, Y. Guo, and G. Rao: Structure and magnetic properties of CeFe_{13-x}Si_x compounds. *J. Appl. Phys.*, Vol. 78, No. 4, 1995, pp. 2866–2867.
- [83] D. P. Middleton and K. H. J. Buschow: Magnetic properties of Ce₂Fe_{17-x}Si_x compounds,” *J. Alloys Compd.*, Vol. 206, 1994, pp. L1–L2.
- [84] D. P. Middleton, S. R. Mishra, G. J. Long, O. A. Pringle, Z. Hu, W. B. Yelon, F. Grandjean, and K. H. J. Buschow: A magnetic, neutron-diffraction , and mossbauer spectral study of the Ce₂Fe_{17-x}Si_x solid solutions. *J. Appl. Phys.*, Vol. 78, No. 9, 1995, pp. 5568–5576.
- [85] R. C. Mansey, G. V. Raynor, and I. R. Harris: Rare-earth intermediate phases VI: Pseudo-binary systems between cubic laves phases formed by rare-earth metals with iron, cobalt, nickel, aluminium and rhodium. *J. Less-Common Met.*, Vol. 14, 1968, pp. 337–347.
- [86] I. R. Harris and G. Longworth: X-ray and mossbauer studies of the pseudo-binary system Ce(Fe_{1-x}Ni_x)₂. *J. Less-Common Met.*, Vol. 45, 1976, pp. 63–77.
- [87] H. Oesterreicher, F. T. Parker, and M. Misroch: Giant intrinsic magnetic hardness in RFe_{5-x}Ni_x (R=rare earth, x=4 to 5). *Appl. Phys.*, Vol. 16, 1978, pp. 185–189.
- [88] A. A. Kodentsov, G. F. Bastin, and F. J. J. Van Loo: Methods for phase diagram determination. J.C. Zhao (Ed), Elsevier, 2007.
- [89] J. C. Zhao, M. R. Jackson, and L. A. Peluso: Determination of the Nb-Cr-Si phase diagram using diffusion multiples. *Acta Mater.*, Vol. 51, No. 20, 2003, pp. 6395–6405.
- [90] H. Putz and K. Brandenburg: Pearson crystal data: Crystal Structure Database for Inorganic Compounds. CD-ROM Software Version 1.3.

- [91] Veeco Metrology Group: Scanning Probe Microscopy Training Notebook. Digital Instruments, Version 3.0, 2000.
- [92] X. Zhu: Magnetic Force Microscopy Studies of Submicron and Nanoscale Magnet Arrays. McGill University, Montreal, Canada, 2002.
- [93] Q. M. Lu, M. Yue, H. G. Zhang, M. L. Wang, F. Yu, Q. Z. Huang, D. H. Ryan, and Z. Altounian: Intrinsic magnetic properties of single-phase $Mn_{1+x}Ga$ ($0 < x < 1$) alloys. *Sci. Rep.*, Vol. 5, 2015, pp. 17086.
- [94] H. Kirchmayr: Supermagnets, hard magnetic materials. NATO ASI Series, Series C: Mathematical and Physical Science, G. J. Long and F. Grandjean (Eds.), Vol. 331, Chapter 18, 1991.
- [95] R. Grössinger, X. K. Sun, R. Eibler, K. H. J. Buschow, and H. R. Kirchmayr: The temperature dependence of the anisotropy field in $R_2Fe_{14}B$ compounds ($R = Y, La, Ce, Pr, Nd, Gd, Ho, Lu$). *Le J. Phys. Colloq.*, Vol. 46, No. C6, 1985, pp. C6–221–C6–224.
- [96] R. Grossinger, X. K. Sun, R. Eibler, K. H. J. Buschow, and H. R. Kirchmayr: Temperature dependence of anisotropy fields and initial susceptibilities in $R_2Fe_{14}B$ compounds. *J. Magn. Magn. Mater.*, Vol. 58, No. 1–2, 1986, pp. 55–60.
- [97] R. Skomski, G. C. Hadjipanayis, and D. J. Sellmyer: Effective demagnetizing factors of complicated particle mixtures. *IEEE Trans. Magn.*, Vol. 43, No. 6, 2007, pp. 2956–2958.
- [98] G. Monnier, R. Riviere, and M. Ayel: Sur l'existence d'un nouveau composé $(Fe,Ni)_{23}B_6$, borure complexe du type structural $Cr_{23}C_6$. *C.R. Acad. Sc. Paris*, Vol. T. 264 Se, 1967, pp. 1756–1757.
- [99] H. H. Stadelmaier and C. B. Pollock: Die metastable tau-phase im system eisen-nickelbor. *Zeitschrift für Met.*, Vol. 60, 1969, pp. 960–961.

- [100] A. Kowalczyk, P. Stefanski, A. Wrzeciono, and A. Szlaferek: Structure and magnetic properties of $R_2Fe_{14-x}Ni_xB$ compounds ($R = Nd$ and Gd). *Phys. status solidi*, Vol. 114, 1989, pp. 355–358.
- [101] F. Bolzoni, F. Leccabue, O. Moze, L. Pareti, and M. Solzi: Magnetocrystalline anisotropy of Ni and Mn substituted $Nd_2Fe_{14}B$ compounds. *J. Magn. Magn. Mater.*, Vol. 67, 1987, pp. 373–377.
- [102] Y. Fukuda, A. Fujita, and M. Shimotomai: Magnetic properties of monocrystalline $Nd_2(Fe,Co,Ni)_{14}B$. *J. Alloys Compd.*, Vol. 193, 1993, pp. 256–258.
- [103] H. C. Ku and L. S. Yen: Magnetic properties of the new permanent magnet compounds $Nd_2(Fe_{0.9}M_{0.1})_{14}B$ ($M = Sc, Ti, V, Cr, Mn, Co, Ni$). *J. Less-Common Met.*, Vol. 127, 1987, pp. 43–48.
- [104] E. Burzo, L. Stanciu, and W. E. Wallace: On the magnetic behaviour of $Y_2Fe_{14-x}Ni_xB$ and $Y_2Fe_{14-x}Co_xB$. *J. Less-Common Met.*, Vol. 111, 1985, pp. 83–86.
- [105] E. Burzo: Iron rich-rare-earth compounds: Basic and permanent magnetic properties. *Rom. Reports Phys.*, Vol. 60, No. 3, 2008, pp. 701–711.
- [106] X. C. Kou, X. K. Sun, Y. C. Chuang, T. S. Zhao, R. Grossinger, and H. R. Kirchmayr: Exchange interaction and magnetic anisotropy in $Nd_2(Fe_{13}M)B$ compounds ($M=Ga, Si, Al$). *J. Magn. Magn. Mater.*, Vol. 82, 1989, pp. 327–334.